Distributed Massive MIMO in Millimetre Wave Communication

Shammi Farhana Islam

Doctor of Philosophy

University of York
Electronic Engineering

April 2022

Abstract

This thesis considers a distributed massive MIMO (D-MaMIMO) system for millimetre wave (mmWave) communication for an outdoor coverage area, as the wavelength of mmWave makes it easier and the free space path loss necessitates the use of relatively large distributed antenna arrays. We assume that the line-of-sight (LoS) links are available between the access points (APs) and user equipment (UEs). We have examined different AP arrangements to serve a given square area using the beamforming (BF) for a single user case. Furthermore, the zero-forcing (ZF) pre-coding is applied at a central processing unit (CPU) on the downlink to separate multiple users. We focus on these multi-user scenarios with varying numbers of APs to demonstrate the extent to which closely spaced users can be separated by ZF processing. We examine the determinant of the effective composite channel matrix to demonstrate the conditions under which the ZF problem may become ill-conditioned. We then show that nearly perfect separation is attainable, even when the UEs are only a few metres apart. Subsequently, an eigenvalue decomposition (EVD) based ZF is proposed to improve the performance of multi-antenna UEs. It has been observed that 3DBF has limited scope in circumstances when users are distributed horizontally, near to the same height as the APs and it is advantageous to employ non-square AP antenna arrays to maximize azimuth separation, especially for multi-user environments. The throughput per UE indicates how many users could be served effectively using the aforementioned schemes and AP arrangements for these multi-user cases. We further explore the significant issue of multipath propagation characteristics for mmWave communication and propose the novel distinction between the effective and the environmental K-factor for Ricean channels. A closed-form approximation for the effective K-factor is derived and corroborated by comparison with numerical results.

Table of Contents

List of Figures

List of Tables

I would like to dedicate this thesis to my loving Father ...

Acknowledgements

The real spirit of achieving a goal is through the way of excellence and austere discipline. I am grateful to the divine God to bless me with the ability to persistently focus on this work. Yet I would have never succeeded in completing my task without the cooperation, encouragement and help provided to me by various personalities.

First and foremost, I would like to express my deepest respect and gratitude to my supervisors Prof. Alister G. Burr and Prof. David Grace for their continuous guidance, valuable discussion and constructive suggestions in various phases of the thesis work. Their feedback and editorial comments were invaluable for the writing of this thesis report. They were extremely sympathetic and kind toward me while I was going through the toughest phase of my life due to my father's demise. I consider myself very fortunate for the opportunity to work with them.

I would also like to thank Dr. Stuart Porter, my thesis advisor, for his insightful discussions and suggestions over the course of this study.

I am greatly indebted to the European Commission for providing me the financial support through "Horizon 2020 Marie Curie Actions".

A special thanks to all my colleagues and friends at the Department of Electronics for providing the nice and friendly environment, a very warm thanks goes to Sumaila, Kafi, Tariq and Steve. A special thank you to my dear friend Roly, for her love and care. I would also like to render my sincere gratitude to my mentors back home for their constant encouragement.

Last but certainly not the least, I am deeply grateful to my family for their inspiration and ever encouraging moral support, which enabled me to pursue my PhD. They sheltered me from all the hardship they faced throughout the tough time so that I can focus on my study and finish the PhD.

Declaration

I declare that this thesis is a presentation of original work and I am the sole author. This work has not previously been presented for an award at this, or any other, University. All sources are acknowledged as References.

List of Symbols

$(\cdot)^*$	Complex Conjugate
$(\cdot)^T$	Transpose
$(\cdot)^H$	Hermitian Transpose
$(\cdot)^{-1}$	Inverse
$\mathbf{X}$	Matrix
$\log 2\,(x)$	Logarithm of x to base 2
$\log\,(x)$	Logarithm of x to base 10
$\det\,(\mathbf{X})$	Determinant of $\mathbf{X}$
$\lvert x\rvert$	Absolute value (modulus) of the a complex scalar x
$\mathbf{I}_N$	N dimension identity matrix
i	Imaginary unit $i = \sqrt{1}$
$diag(a)$	A diagonal matrix with the entries of $\mathbf{a}$ on its diagonal
$\mathrm{sinc}(x)$	Sinc function with input x

List of Abbreviations

2D	Two-dimensional
2DBF	Two-dimensional Beamforming
3D	Three-dimensional
3DBF	Three-dimensional Beamforming
3GPP	3rd Generation Partnership Project
4G	Fourth Generation Mobile Networks
5G	Fifth Generation Mobile Networks
6G	Sixth Generation Mobile Networks
5G NR	5G New Radio
AAS	Antenna Array System
AI	Artificial Intelligence
ADC	Analog-to-Digital Converters
AOA	Angle-of-Arrival
AP	Access Point
BF	Beamforming
BS	Base Station
CAA	Collocated Antenna Array
CDF	Cumulative Distribution Function

CF	Cell Free
CPU	Central Processing Unit
C-RAN	Cloud/Centralised Radio Access Network
CSI	Channel State Information
DAA	Distributed Antenna Array
DAS	Distributed Antenna System
DL/UL	Downlink/Uplink
DMIMO	Distributed Multiple Input Multiple Output
EE	Energy Efficiency
eMBB	enhanced Mobile Broadband
EVD	Eigenvalue Decomposition
FD-MIMO	Full-dimension MIMO
FSPL	Free-Space Path Loss
HD	High Definition
ICIC	Inter-Cell Interference Cancellation
IoT	Internet of Things
IUI	Inter User Interference
LSAS	Large-scale Antenna Systems
LoS	Line-of-Sight
LTE	Long-Term Evolution
MaMIMO	Masssive Multiple Inputs Multiple Outputs
MIMO	Multiple-Input-Multiple-Output
MMSE	Minimum-Mean-Squared-Error

mMTC	massive Machine-Type Communications
MR	Maximum Ratio
mmWave	Millimetre Wave
MU	Multiple User
NLoS	Non-Line-of-Sight
NR	New Radio
PD	Partially Distributed
RAN	Radio Access Network
RAT	Radio Access Technologies
RF	Radio Frequency
SE	Spectral Efficiency
SINR	Signal-to-Interference-plus-Noise Ratio
SNR	Signal-to-Noise Ratio
SVD	Singular Value Decomposition
UDN	Ultra-Dense Network
UE	User Equipment
ULA	Uniform Linear Array
UPA	Uniform Planar Array
URLLC	Ultra-Reliable and Low Latency Communications
ZF	Zero-Forcing
ZFBF	Zero-Forcing Beamforming

Chapter 1

Introduction

1.1 Overview and Motivation

In future wireless communication, 5G and beyond is expected to enhance the network with higher aggregated data rate, low latency by reducing the costs and energy consumption. Undoubtedly, 5G has earned higher publicity than any other previous generations not only among the research and technical bodies but at every level of society. 5G has extended conventional mobile communication to establish connections between humans, machines and devices through internet of things (IoT), augmented reality, artificial intelligence (AI), industrial automation. Moreover, amidst a crisis like the global pandemic (Covid-19) where unprecedented restrictions on public mobility have been imposed, the use of virtual platforms have become more prominent than ever. In order to keep systems running, communication and services have shifted to digital platforms. The pressing challenges due to this kind of situation, can only be addressed by building an efficient network with greater capacity to be able to connect as many devices even in small areas simultaneously. This surely requires the services and applications promised by 5G technology. The remote services required in this crisis such as remote surgery, on-line classes, remote office, driver-less vehicles, unmanned delivery, smart healthcare, and autonomous industries can be supported by the 5G architecture [1][2]. According to [3], International Mobile Telecommunications-2020 (IMT-2020) standards defined by the ITU-R (radio section of the International Telecommunications Union) documented the 5G usage scenarios:

- **Enhanced Mobile Broadband (eMBB)** aims to boost the existing mobile network with higher speed, greater capacity and wider coverage to support the future consumer services and applications designed using the broadband mobile connectivity such as

3D video transmission, UHD (Ultra-High Definition) screens, augmented reality, etc. [1][4].

- **Ultra-Reliable and Low Latency Communications (URLLC)** is designed to support the mission/time critical applications which are sensitive to reliability, availability and latency. It creates new possibilities for Industry 4.0 facilitated by industrial automation, remote health surgeries, automatic vehicles etc. [1][4].
- **Massive Machine-Type Communications (mMTC)** targets the ultra dense network with large number of connected devices that are economic, have low-power consumption and transmit low volume of data which are not sensitive to delay. Examples of such scenarios are smart grid, smart home, smart cities etc. [1][4].

Initially, 5G was expected to be rolled out worldwide by 2020 but currently it is still on the implementation stage in some parts of the world [5]. In [4], the authors envisage that because of the video based communication, the use of billions of applications and smart devices, the global IMT traffic will be increased in the range of 10-100 times from 2020 to 2030. As a result, the researchers in academia and industry have started to ponder beyond 5G and moving towards 6G to meet the future demands for information and communications technology (ICT) in 2030. Besides the services that 6G has to offer such as holographic type communication (HTC), extended reality (ER), tactile internet, multi-sense experience, pervasive intelligence, intelligent transport and logistics, enhanced on-board communications and so on, cater for the evolution of current network towards a more powerful and more efficient system in terms of cost, energy, spectrum, and operational efficiency. Consequently, the aforementioned usage scenarios in 5G require revision to support the 6G services [1].

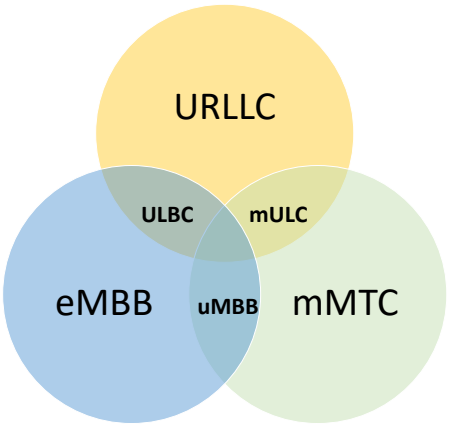

Fig. 1.1 Usage scenarios in 5G and 6G [1]

Therefore, three new usage scenarios have been proposed: ubiquitous MBB or uMBB (ensures global ubiquitous connectivity across the whole earth surface), ultra-reliable low-latency broadband communication or ULBC (supports URLLC and also provides very high throughput for 6G applications such as HTC) and massive ultra-reliable low-latency communication or mULC (combination of mMTC and URLLC scenrios). To satisfy the technical requirements of these use cases, shown in Fig. 1.1, has been the main motivation for the innovations in the future wireless communication [1].

Therefore, some of the key requirements of these usage scenarios are high data rate, larger bandwidth, dense connectivity, low latency, wide coverage, high energy and spectral efficiency. IMT2020 considers millimetre wave (mmWave) communication a prospective candidate to provide the data rate that is considered one of the 5G key performance indicators (KPIs) by IMT2020. Furthermore, the enabling technologies such as massive multiple-input and multiple-output (MaMIMO), beamforming (BF) exploiting large scale antenna arrays have provided promising possibilities in implementing the mmWave communication. Compared to lower frequencies used in 4G-LTE, mmWave suffers from increased pathloss with propagation distance and blockage from environmental components due to shorter wavelengths. As a result, line-of-sight (LoS) propagation plays dominant part in mmWave channel as the signals scatter, reflect and diffract with a large angular spread due to the blockage from human body, buildings, foliage etc. The non-LoS received signals emerge from first and second order reflected paths through the surfaces of the objects in outdoor environments. To support a large number of smart devices in crowded areas, ultra-dense networks must be deployed due to the mmWave propagation characteristics and to assure uninterrupted connections for mobile users [6]. However, [7] shows distributed MaMIMO (D-MaMIMO) has sufficiently enhanced the network performance compared to small-cell and collocated antenna approach by providing more dedicated antenna arrays as base stations (BS) for the users. The D-MaMIMO based mmWave communication is preferable to provide the BS diversity to overcome the pathloss and attenuation in mmWave propagation that can be caused by the large distances between BSs and user equipments (UEs). In addition, increasing the number of elements per antenna array provides increased directional gain, and 3D beamforming can support directing the beams both in horizontal and vertical directions. Hence, multi-beam steerable antenna arrays are even capable of serving the mobile transceiver when the LoS path does not exist [6]. D-MaMIMO systems using multi-beam directional arrays and suitable pre-coding can improve the spectral efficiency and reduce the multi-user interference.

Implementing the D-MaMIMO mmWave system is challenging as it requires proper estimation of the channel and a channel model that captures the unique mmWave features. In addition, to cancel the inter-user interference a proper pre-coding scheme needs to be designed. Motivated by the challenges and the proposed enabling technologies this thesis, therefore, considers the advantages of D-MaMIMO mmWave communication over centralised or collocated MaMIMO for an outdoor environment and investigates the ZF pre-coding approach in detail evaluating under what conditions this pre-coding can effectively eliminate the user interference. We also show the importance of coordinated multi-antenna arrays and, the impact of the K-factor in multipath scattering.

1.2 Research Objectives

This thesis focuses on the design of distributed massive MIMO in mmWave communication and, to overcome challenges of implementing an ultra-dense radio access network using D-MaMIMO in the mmWave band. The objectives are summarised as follows:

- Focusing on using distributed antenna arrays rather than having a single antenna at each access point (AP); partially distributing the total elements into small number of arrays to utilize micro-diversity.
- The antenna arrays are configured to perform 3D beamforming (BF), therefore, providing the directionality requires in mmWave communication. So that this model can be easily adapted in the scenarios where the vertical separation between the AP and user equipment (UE) is large.
- Reducing the complexity of the zero-forcing (ZF) scheme to eliminate the inter-user interference.
- Analysing the performance of the ZF algorithm, considering the effect of two adjacent users.
- Scaling up the number of users that can be served by a particular arrangement of APs in terms of the number antenna elements in each AP, and the horizontal and vertical orientation of the antenna elements.
- Investigating the performance degradation from the non-coordinated multiple APs.
- Study the multi-antenna user scenario, whether it is beneficial for the multiple user (MU) D-MaMIMO to have users with additional antennas.

- Emphasising on the impact of antenna array gain and scatterer distribution on the K-factor of a Ricean channel.

1.3 Contributions and Structure of the Thesis

This thesis addresses the challenges in implementing D-MaMIMO for the mmWave channel for both LoS and NLoS environments. It proposes novel schemes to improve the performance by cancelling the inter-user interference and provides insightful results for multi-user (MU) D-MaMIMO scenarios. The scope of this thesis comprises finding the best distribution of the antenna arrays for a particular coverage area, analysing and designing ZF algorithms, combining eigenvalue decomposition with ZF for multi-antenna user, introducing the concept of environmental and effective K-factor for Ricean fading and numerical simulation results. This thesis is organised into seven chapters and the main contributions of the remaining chapters are summarised as follows:

- Chapter 2: **Literature Review**
  The chapter is dedicated to the fundamental concepts and literature review related to this thesis. Firstly, it introduces the state-of-art, requirements and challenges for 5G. Next the propagation characteristics, proposed channel model and attenuation factors for mmWave frequencies. Moreover, the MU D-MaMIMO or CF-MaMIMO architecture for mmWave communication and their shortcomings are documented. In addition, the type of antenna arrays used in this thesis work are described. Finally, the basic principles of antenna array beamforming, ZF-precoding and eigenmode decomposition are reviewed.

- Chapter 3: **Distributed 3D Beamforming for a Single User**
  In Chapter 3, the distribution of antenna arrays are compared to a centralised array is studied for a single user. The entire coverage area is divided into small grids to exhibit the SNR performances for different combinations and configurations of APs using cooperative 3D beamforming. The received signals are combined coherently at the UE from each AP. Parts of this chapter's findings were included in a conference paper given at the International Conference on Emerging Technologies of Information and Communications (ETIC).

- Chapter 4: **Multi-user D-MaMIMO System using Zero-forcing Pre-coding**
  Chapter 4 deals with multi-user scenarios, and cancelling the inter-user interference. 3D

BF can provide the directionality and direct the beams toward the intended user. 3DBF is insufficient to reduce interference among the UEs where there is little difference in height between the APs and UEs. Except for the instances where the users are extremely close to one of the APs, the elevation angles for almost every other user vary insignificantly. Hence, a novel reduced complexity partially centralized zero-forcing (PC-ZF) scheme is proposed to successfully eliminate the inter-user interference where the CSI is available to the CPU. An analysis is presented to evaluate the performance of the ZF algorithm for two adjacent users and their correlation is also shown. Moreover, it is also observed that if phase error occurs at the transmitter end due to unstable mmWave oscillators, it affects the performance of the system differently for different AP arrangements. This technique is also applied in more dense user scenarios and that gives us the approximation of the number of UEs that can be served by a set of AP arrangement for a given coverage area. Based on the concepts and findings of this chapter, a conference paper was presented at the IEEE Statistical Signal Processing Workshop in 2021 and a chapter in the book titled "Cell-Free MIMO Systems for UDNs".

- Chapter 5: **Multi-user D-MaMIMO System with Multi-antenna APs and UEs**
  In Chapter 5, multi-antenna UEs are utilised to provide diversity and improve the throughput. A new approach has been implemented where eigenmode decomposition is combined with zero-forcing to send single stream of data to an user rather than multi-stream using only ZF. The observations of this chapter are provided in a more generalized approach from the concepts described in the paper presented in 54th Asilomar Conference on Signals, Systems, and Computers conference in 2020 as the the results involve more than just the strongest eigenvector.

- Chapter 6: **Impact of K-factor in mmWave Transmission**
  Chapter 6 focuses on the impact of K-factor for multipath channel using a simple one ring scattering multipath model. The effect of directional antenna gain on K-factor is highlighted. We proposed two novel concepts distinguishing the resultant K-factor from using single antenna and directional antenna array in the transmitting end. We defined them as Environmental and the Effective K-factor respectively. A closed form expression is derived to support the proposition. This chapter's concept and findings were presented at the 17th International Symposium on Wireless Communication Systems (ISWCS) in 2021.

- Chapter 7: **Conclusion and Future Work**
  Finally, Chapter 7 presents the conclusions of the novel contributions in this thesis and provides some further potential research directions for future work.

1.4 Publication List

Conference Papers

1. Shammi Farhana Islam, Alister G. Burr, David Grace, "Impact of Directional Array Response on K - factor in Millimetre Wave Transmission," 2021 17th International Symposium on Wireless Communication Systems (ISWCS), 2021, pp. 1-5.

2. Shammi Farhana Islam, Alister Burr, David Grace, "Capacity of Distributed Millimetre-wave Antenna Arrays," 2021 IEEE Statistical Signal Processing Workshop (SSP), 2021, pp. 256-260.

3. Alister Burr, Shammi Islam, Junbo Zhao, Manijeh Bashar, "Cell-free Massive MIMO with multi-antenna access points and user terminals," 2020 54th Asilomar Conference on Signals, Systems, and Computers, 2020, pp. 821-825.

4. Shammi Farhana Islam, Alister Burr, David Grace, "Coherent and non-coherent combining in distributed millimetre wave beamforming", International Conference on Emerging Technologies of Information and Communications (ETIC), March 8-10 2019, Samdrup Jongkhar, Bhutan.

Book Chapter

1. Roya Gholami, Shammi Farhana Islam, Sumaila Mahama, Dirk Slock, Laura Cottatellucci, Alister Burr and David Grace, "Cell-Free MIMO Systems for UDNs", Enabling 6G Mobile Networks, Springer, Cham, 6 November 2021.

Journal Papers

1. Shammi Farhana Islam, Alister G. Burr, David Grace, "Multi-user distributed massive MIMO for mmWave communication," to be submitted to IEEE Access, (2022).

Chapter 2

Literature Review

2.1 Introduction

The chapter introduces the fundamental concepts of 5G wireless communication and discusses the relevant literature focusing on the topics of this thesis. It highlights the evolution of 5G and the impediments it faces to its implementation. Furthermore, it discusses the state-of-the-art, requirements and potential solutions for 5G deployment. As mentioned in Chapter 1, the focus of this thesis is to investigate distributed massive MIMO for mmWave communication. Therefore, this chapter aims to introduce the basic principles of the techniques used in this thesis. First, the introduction and challenges in 5G are discussed in Sec. 2.2. The fundamentals of millimetre waves and their challenges are described in Section 2.3. Next, an overview of distributed massive MIMO as one of the potential solutions for mmWave communication is discussed in Section 2.4. In Section 2.5, the basics of antenna arrays and the beamforming techniques employed in this thesis are presented. Furthermore, the basic concepts of zero-forcing (ZF) pre-coding are given in Section 2.6. The process of singular value decomposition (SVD) is presented in Section 2.7 and finally, the chapter is summarized in Section 2.8.

2.2 Fundamentals of 5G

Wireless communication systems have been evolving since early 1970s and have gone through four generations (1G, 2G, 3G, 4G) of technological development to provide connectivity to billions of people providing a global platform as we are experiencing today. These developments have paved their ways through numerous innovations and upgrades between

generations. As a result, the network performance has been enhanced significantly at an affordable cost. The fourth generation (4G) of wireless communication systems has enabled mobile broadband internet access for laptops, smartphones, and other mobile devices, resulting in the emergence of popular services like mobile web access, IP telephony, gaming, HD video transmission, 3D television, and cloud computing. Moreover, the commercial deployment of 4G, which includes the first-release Long Term Evolution (LTE) standard, has expanded the scope of mobile communication beyond voice calls and text messaging. As a result, to meet the demand of the increasingly heavy traffic and mitigate the limitations of 4G to support future applications, the 5G wireless communication system has already begun to replace the existing 4G LTE system and provided a network empowered with new deployment models and new services [8][9]. The deployment of 5G will extend the mobile communication system into new possibilities, and it is expected for 5G to have a significant impact on the evolution in different areas such as industry 4.0, automotive and mobility, transportation, healthcare system, agriculture, energy industry, education, media and entertainment, ecosystem. Moreover, new value chains for business models are being developed [4]. In short, we can say that the 5G features and their applications will lay the foundation for next industrial and technological revolution which necessitates real-time and ultra-high quality delivery. Furthermore, future applications such as augmented reality, artificial intelligence (AI)-based systems, and the internet of things (IoT) will require substantially higher bandwidth to provide high data rates for uninterrupted transmission [10].

The key requirements of the 5G wireless system are given below:

- **Data Rate:** The main driver for 5G technology is that it has to support a significant amount of data traffic. In order to provide that the aggregate data rate should be increased by around 1000 compared to 4G.

- **Latency:** In 4G-LTE the latency is approximately 15 milliseconds and sufficient for most of the current applications. As 5G is expected to deal with real-time data for the applications mentioned above, the latency is anticipated to be roundtrip latency of about 1 millisecond.

- **Energy and Cost:** The cost and energy consumption should be less in 5G than 4G. Since the per-link data rates will be increasing by around $100\times$ which in turns should compensate in low cost per bit by at least $100 \times 4G$. The main concern for 5G cost consideration is the increasing number of base station (BS) and bandwidth in the backhaul [11].

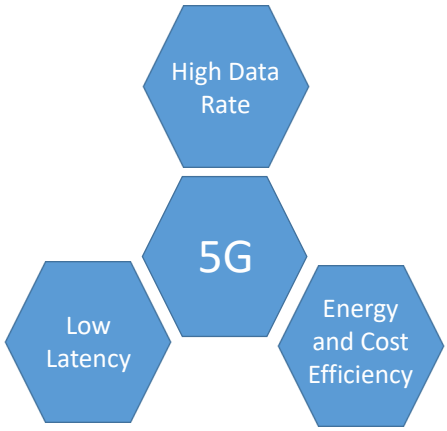

Fig. 2.1 The requirements of 5G

2.2.1 Challenges in 5G

Initially, 5G was expected to be available by 2020, however obtaining the aforementioned attributes has proven to be challenging. Candidate IMT-2020 systems are undergoing an extreme review process to guarantee they meet the international telecommunication union's (ITU) standards for IMT-2020 systems, which are designed to meet the performance requirements of forthcoming 5G applications and typically support three usage scenarios: enhanced Mobile BroadBand (eMBB), Ultra Reliable and Low Latency Communication (URLLC) and massive Machine Type Communication (mMTC) (mentioned in Chapter 1) [12].

It is a huge challenge to provide the proposed data rate in a 5G network. Moreover, the number of mobile data subscribers will also increase globally. The prediction graph made by Ericsson (Fig. 2.2) shows that the estimated mobile data demand by 2024 and revealed that by end of 2024 45% of the total world's population will be privileged with 5G coverage [13].

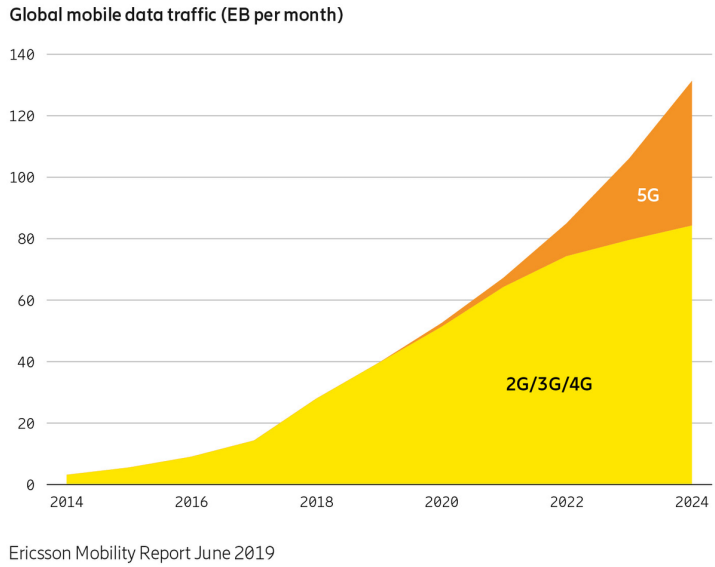

Fig. 2.2 Estimated worldwide mobile data demand [13]

There are two ways to overcome this: first, use wider frequency bands, such as millimetre wave (mmWave) bands, and second, BSs should be deployed in such a way that they form ultra-dense networks to increase capacity per unit area, resulting in a small cell [14]. Operating in mmWave, on the other hand, poses challenges due to its distinct propagation characteristics. Networks in 5G new radio (NR) and beyond are expected to be completely heterogeneous. Furthermore, the radio access network (RAN) will be extremely complex in design, incorporating a wide range of base stations, macrocells, microcells, femtocells, access points (APs), and relays. Additionally, along with device to device (D2D), machine to machine (M2M) communications, the 5G NR and beyond networks will be extensively densified. Consequently, energy consumption is predicted to increase dramatically and it is critical to recognise that 5G and beyond cellular networks may impact largely on the environment with an increase in the CO_2 emissions. It is observed that rise in world average temperatures can be attributed to CO_2 emissions into the atmosphere. This concerns the researchers to built energy-efficient networks termed as “sustainable green communications” [15]. Other challenges are associated with the average spectral efficiency, mobility, good coverage, and diverse quality of service (QoS) requirements [9].

2.2.2 Proposed Technologies for 5G Architecture

To overcome the challenges in 5G wireless system several cutting-edge technologies are proposed by the researchers. Some of these are mentioned below, forming the objectives of this thesis.

- **Millimetre Wave:** To provide higher data rates, 5G aim to utilize the vast amounts of unused spectrum in the millimetre (mmWave) ranging 30–300 GHz, with wavelengths of 1–10 mm [11].
- **Distributed or Cell-free Massive MIMO:** One of the cutting-edge technologies, distributed or cell-free massive multi input multi output (MaMIMO) is one of the ultimate solutions to ensure multi-user transmission in mmWave communication [16].
- **Beamforming:** Beamforming (BF) technology directs a beam to a particular direction and, concentrates the energy towards that direction which helps to overcome the high attenuation in mmWave communication. BF using mmWave band is one of the key technology in enabling 5G communications [17].

2.3 Millimetre Wave

One of the main challenges in 5G wireless communication is to achieve the desired data rate to ensure uninterrupted and high speed data transmission for user's services such as mobile cloud, ultra-high-definition (UHD) 3D video, virtual and augmented realities, internet-of-things (IoT), satellite communications, unmanned aerial vehicle (UAV) [18]. Consequently, the existing frequency allocation is unable to meet the expected high data rate and, hence a larger bandwidth is required. The existing bandwidth is limited in the available assigned frequency spectrum for 4G LTE that is below the mmWave band. So, obviously the mobile operators are eager to explore mmWave mobile frequency spectrum due to its ability to support a wider bandwidth. The specifications for the 5G frequency range are published in the 3GPP Release 15 and beyond [19]. The frequency bands that fall between 30 GHz to 300 GHz is known as the millimetre wave (mmWave) band. This is because the wavelength of electro-magnetic wave in this range is in the millimetre (1-10 mm) range (hence the name). This millimetre band are categorised varying the different frequency range, such as Q-band (30-40GHz), U-band (40-60GHz), V-band (50-75GHz), E-band (60-90GHz), W-band (75-100GHz), F-band (90-140GHz), D-band (110-170GHz) and G-band (110-300GHz) [20].

2.3.1 Characteristics and Propagation of mmWave Band

Although mmWave frequencies provide large bandwidths, the deployment of mmWave requires a good understanding of the propagation characteristics of mmWave communication. The propagation characteristics of mmWave communication are mentioned below:

- **Path Loss:** The free-space loss (FSL), as the name suggests, is the loss in the transmitted signals strength in free space and it is dependent on the carrier frequency f_c and the separation distance d between the transmitter and receiver. If the received power at the receiver is P_r and the transmit power from transmitter is P_t and the transmitter and receiver are placed at a distance d then the equation is given by:

$$\frac{P_r}{P_t} = \frac{\text{Area of receiver antenna}}{\text{Area of sphere}} = \frac{A_d}{4\pi d^2} \tag{2.1}$$

  Here A_d is the aperture area or effective area of an antenna, normal to the line of sight direction. For an antenna with gain G, the aperture area is given by:

$$A_d = G\frac{\lambda^2}{4\pi} \tag{2.2}$$

  For directional antennas, the equation becomes,

$$\frac{P_r}{P_t} = G_t G_r \left(\frac{\lambda}{4\pi d}\right)^2 \tag{2.3}$$

  this is known as Friis' law of free space propagation loss [21]. Now G_t is the transmit antenna gain and G_r is the receiving antenna gain. For fixed antenna gain path loss increases with carrier frequency, and this is the main problem in moving up to mmWave frequencies.

  If the transmit antenna has aperture (effective) area of A^t_{eff} and a receiver at distance d with effective aperture area A^r_{eff}, the received power P_r is given by:

$$\frac{P_r}{P_t} = G_t \frac{A^r_{eff}}{4\pi d^2} \tag{2.4}$$

  where $G_t = \frac{4\pi A^t_{eff}}{\lambda^2}$

$$\frac{P_r}{P_t} = \frac{A^t_{eff} A^r_{eff}}{\lambda^2}\frac{1}{d^2} \tag{2.5}$$

From the above equation 2.5 it is seen that, that if the aperture area is fixed , then the propagation loss decreases with increasing carrier frequency [22]. The antennas also become more directional as frequency increases, which makes it more important that the beams can be steered, and that is why we need to use antenna arrays and beamforming.

- **Atmospheric Attenuation:** mmWaves are vulnerable to the atmospheric attenuation caused by gas molecules in the earth's atmosphere, which limits the propagation, called gaseous attenuation. The radio waves are absorbed by the air molecules that cause the attenuation like oxygen (O_2) and water vapour (H_2O). This gaseous absorption depends on many factors, such as the temperature, pressure, altitude and the carrier frequency [22]. Atmospheric attenuation is dominated by oxygen absorption, which is highest at 60 GHz with a value of over 15 dB/km [23].

- **Rain Attenuation:** the rain droplets also attenuate mmWaves. The wavelengths of mmWave signals ranges between 1 mm and 10 mm and the size of a raindrop is normally found within a few millimeters. Due to this compatible size these signals face scattering due to rain droplets. The intensity of attenuation depends on the nature of rain: whether it is heavy or light rain. For example light and heavy rain-rates can induce an attenuation of 2.5 dB/km and 20 dB/km, respectively [11][22][24].

- **Foliage Attenuation:** While deploying mmWave in rural and forest areas, foliage attenuation is an important consideration. mmWave propagating from transmitter to receiver through vegetation can cause some degree of attenuation and affect the Quality of Service (QoS). Like the rain attenuation the intensity of foliage attenuation depends on quantity of trees as multiple trees attenuates more than a single tree, and a forest exceeds the amount by multiple trees [18][22].

- **Blockage:** The mmWaves have a lower tendency to diffract than microwaves, making them much more susceptible to blockages.. According to [20][25], depending on the transmitter-receiver distance, for line-of-sight (LoS) transmission the rate of path loss decay is 20 dB/decade, whereas, in the non LoS (NLoS) environment this rate increases to 40 dB/decade along with 15-20 dB additional loss.

- **Other Factors:** The mmWave frequencies also suffer attenuation due to various type of obstacles such as room furniture, doors, walls, human bodies etc. [26][27][28]. For an example, according to [22][26] in an indoor environment, a 1.9 cm thick whiteboard attenuates a 60 GHz signal by 9.6 dB. In addition, mmWave frequencies also get

affected by Doppler spread. The Doppler spread yields frequency dispersion because of moving nodes and, it depends on the frequency and the speed of mobility. Therefore, the Doppler spread is higher in mmWaves than in lower frequencies. The Doppler spread f_D can be mathematically expressed as:

$$f_D = (v/c)\, f_c \cos(\theta - \theta_v)$$

where, f_c is the carrier frequency, v is the velocity of the receiver, θ is the direction of arrival and θ_v is the direction of the velocity vector [29].

On the other hand the presence of human body between the transmitter and the receiver can attenuate the received signal of 25-30 dB for a single person [22].

2.3.2 Challenges in mmWave Communication

Due to wide unlicensed, semi-licensed, and licensed bandwidth available in the mmWave frequency band, it has drawn significant interest in academia, industry and standardization bodies to enhance the network capacity substantially. However, as previously discussed, the distinctive propagation characteristics of mmWave frequencies and shadowing necessitate additional modelling efforts [22]. Hence, there are a number of additional challenges to overcome in order to fully utilise the benefits of mmWave communication.

- **Integrated Circuits and System Design:** mmWave transmission will face several technical challenges due to the high carrier frequency and wider bandwidth. These high transmit power and large bandwidth induce non-linear distortion in power amplifiers (PA). In addition, radio frequency (RF) integrated circuits encounter phase noise and IQ imbalance which can cause performance degradation [25][30].

- **Densified Base Stations:** The proposed architectures for mmWave transmission such as small cells or cell-free systems will increase the number of base station (BS). Hence, the spectrum can be reused over the entire coverage area and the probability of a user served by a nearby BS will increase. In spite of these benefits, this BS densification can face some challenges such as establishing users and BSs connections across multiple radio access technologies (RATs), providing mobility for heterogeneous network [11]. Moreover, in this kind of network, the interference between different BSs requires to be dealt with [25].

- **User Mobility Support:** Providing support for user mobility is challenging, especially in mmWave communication as a moving user experience constant changes in the channel state. The variation in the distance among the users and transmitter causes fluctuation in the channel state. Another concern for user mobility is handoffs for mmWave communication as the transmitter and receiver beams must be synchronised for effective communication [11][25].

- **Energy Efficiency and Cost Aspects:** The base station densification will definitely increase the installation, maintenance and backhaul costs. To mitigate this challenge, the designers have to come up with novel energy efficient and cost-effective multi-antenna transceiver architectures to make use of this large mmWave spectrum efficiently. Furthermore, the installation and maintenance costs of wireless backhaul requires to be affordable [11][31].

2.3.3 Channel Model for mmWave Communication

The path loss according to the Friis transmission formula, shadowing effects, and different attenuation losses at the mmWave channel, estimating the accurate channel model is one of the important aspects of 5G innovation. For accurate channel estimation, multipath components also need to be considered. According to [22] channel models are classified into two groups: physical channel models and analytical models. The physical channel models depend on the electromagnetic characteristics of signals propagating from transmitter to receiver whereas analytical channel models rely on mathematical analysis of the channel. The physical channel models are more used in MIMO channel modelling and they are classified into two classes: deterministic and stochastic physical models. The author of [32] have focused on the importance of accurate mmWave channel model based on six areas: spatial consistency, blocking, clustering, ground reflections, frequency dependency and effective channels for link level simulation. In addition, different stochastic and measurement based channel models are used in several papers on mmWave propagation for LoS and NLoS environment in [33][34][35][36][37][38]. Many projects have developed mmWave channel models such as 5GCM, METIS, 3GPP, mmMAGIC [22]. According to [22][38], some of the popular channel models are 3GPP and WINNER II, COST 2100, MiWEBA, METIS, SIRCIM/SMRCIM and Kronecker.

The channel models mentioned here are generally unable to take account of all features of mmWave propagation in a single model, as they have to deal with limiting factors such as 3D modelling, lack of measurements, lack of scenarios, large scale antennas, directional antennas

and huge bandwidth. Moreover, in a multipath scattering scenario, closely spaced users will experience the same signal through the reflectors, hence, the angle-of-arrival (AoA) and direction of arrival (DoA) at the APs remain same for all the users. This spatial characteristic also should be considered in modelling the mmWave channel. For example the MiWEBA project create a single equivalent channel model for entire mmWave band and the parameters vary based on LoS or NLoS scenario. For the METIS project, three different channel models are proposed, as a single one is not applicable for all mmWave ranges [22].

2.4 Distributed Massive MIMO for mmWave Communication

2.4.1 Concept of Massive MIMO

Massive multi-input-multi-output (MaMIMO) is one of the important key technologies in implementing 5G for future wireless communication. In modern wireless communications, MaMIMO techniques have gained considerable attention because of the high spectral efficiencies, energy efficiencies and extended coverage to overcome the traffic problem. The concept of MaMIMO is to use an array containing a large number of antenna elements at the BS which can serve several users at the same time and over the same frequency resource [39][40]. In 2010, Thomas L. Marzetta first introduced this concept of large antenna arrays in his paper which was basically on multi-user MIMO with large antenna arrays. He concluded his paper saying that if the number of antenna elements at the base station is very large compared with the numbers of users being served, simple linear pre-coding becomes possible on the forward link, and linear combining on the reverse link. After this many studies have been performed on MaMIMO. In some, this concept is also named large scale antenna systems (LSAS), very large multi-user MIMO and large-scale MIMO [41][42]. In MaMIMO, the cell size reduction can be avoided by adding more antennas to the current cell sites thus increasing the network capacity. In addition the transmit powers in uplink and downlink are reduced in large scale antenna systems as the powers are combining coherently and the antenna aperture is increased [43]. With the transmission of data streams from multiple antennas and utilization of diversity gains offered by channel propagation effects, the data rate can be increased. The MaMIMO can be implemented using large antenna arrays, with perhaps hundreds to thousands of elements and these large antenna systems concentrate the energy over a small area/short time that enhances the antenna throughput and the efficiency of radiated energy. The concept of MaMIMO is depicted in Fig. 2.3. The MaMIMO has

been shown to have better performance compared to conventional MIMO in the physical layer for 5G future wireless communication as it offers many benefits such as increased data rate, enhanced reliability, improved energy efficiency and reduced interference [44]. The quasi-orthogonal nature of the channels between each BS and the active users using the identical frequency and time makes the transmitter/receiver simpler. For some assigned numbers of users, using large antenna arrays at the BSs the orthogonality is improved, and simple linear transceivers even with single-user beamforming show performance close to an optimal level [11].

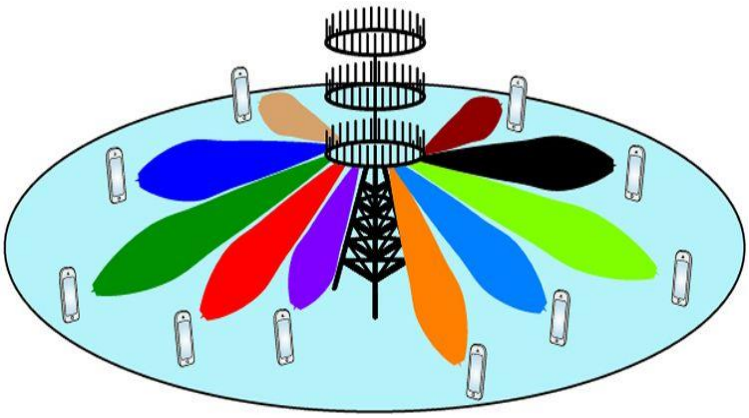

Fig. 2.3 Massive MIMO concept (directly reproduced from [45])

The implementation of MaMIMO faces huge challenges with the increasing number of antennas, thus, the complexity of the system rises. Some of the challenges are given below:

- **Pilot Contamination and Overhead Reduction:** Pilot contamination effects the channel estimation quality and becomes a concerning issue as the number of BS antennas increases. However, the pilot transmission needs to be designed sensibly to avoid excessive overhead. Several considerations have been made, such as sharing the pilot symbols across the antenna, dividing the pilots into groups [11].
- **Architectural Challenges:** The MaMIMO architecture draws special attention in terms of required different BS structures. As a result, some features such as scalability, antenna correlations and mutual couplings, and cost, should be taken under consideration [11].
- **Full-Dimension MIMO and 3D Beamforming:** Linear horizontal antenna arrays exploit the beam in the azimuth direction which limits the service towards high-rise

structures, because of the form factors. In order to counter this issue, 2D arrays can be used to allow beam steering in the vertical direction. This full-dimension MIMO (FD-MIMO) can incorporate extra antennas with same form factor and in turns the signal power is enhanced due to the elevation beams (i.e. 3D beamforming) and reduces the interference [11].

- **Channel Models:** Implementation of MaMIMO calls for proper channel estimation. Channel aging or channel estimation errors can cause performance degradation, especially due to user mobility. The dynamic channel estimation has to be done frequently after the coherence interval [46].

- **Coexistence with mmWave:** As mentioned in Section 2.3 that due to the smaller antenna at mmWave frequencies, in mmWave communication it is often preferable to adopt many antennas i.e. MaMIMO and beamforming. However, at mmWave frequencies, the use of massive MIMO would have to strike the right balance between power gain/interference reduction and parallelization [11].

- **High Cost and Power Consumption:** Using large antennas at the BSs can be expensive and power consuming because of the installation costs and other mixed signal components, such like high-resolution Analog-to-Digital Converters (ADCs). Hence, the design consideration should be done carefully and cost effectively [46].

So, we can see from the above discussion that massive MIMO is one of the enabling key technology in the deployment of mmWave for the 5G era. As the size of the single antenna operating at high frequency will be extremely small and the aperture (usually half of the desired wavelength of carrier frequency) will also be small. Therefore, to increase the signal strength at the receiver end, the number of antennas requires to be increased at the transmitting end.

2.4.2 Cell-free or Distributed Massive MIMO

Although MaMIMO encounters a few challenges, undoubtedly, this technology proposes significant reduction in transmission energy and induced interference. MaMIMO can be implemented either as centralised or in a distributed system [47].

- **Centralised Massive MIMO:** In centralised massive MIMO, the large scale antennas are concentrated into one singe array at the BS. It facilitates the system with low data-sharing overhead and fronthaul requirements [41].

- **Distributed Massive MIMO:** In distributed massive MIMO (D-MaMIMO) the total antennas are split into different arrays throughout the coverage area. Therefore, this provides high diversity gain against shadow fading to ensure uniform quality of service [44].

D-MaMIMO can be incorporated in both multi-cell or cell-free scenarios [48] and cell-free massive MIMO (CF-MaMIMO) seems promising for the distributed approach [7]. The concept of cell-free massive MIMO (CF-MaMIMO) can be defined as a system where large number of antennas are distributed throughout a wide coverage area, simultaneously serving a comparatively small number of user equipments (UEs) over the same time-frequency resource via the fronthaul network and a central processing unit (CPU). This is one of the promising technologies that ensures quality of service to the UEs [47]. This thesis focuses on the D-MaMIMO approach for the cell-free environment.

In CF-MaMIMO/D-MaMIMO, a large number of access points (APs) are distributed over a service area jointly transmitting simultaneously towards all the UEs using the local channel state information (CSI). The APs receive the downlink (DL) data and power control coefficients from the CPU, and also send back the data coming from all the UEs in the uplink (UL) to the CPU through fronthaul links. In addition, only the channel statistics are known to the CPU to perform joint detection [47]. This technique eliminates cell boundaries while providing services to users in a specific area. In addition, this CF approach reduces the path loss between the APs and the UEs and ensures good quality of service (QoS) in spite of its low-complexity signal processing. In fact, mmWave CF MaMIMO system can support the coverage in crowded spaces such as gymnasium, concert hall, etc. [49].

2.4.2.1 The Advantages of CF or D-MaMIMO

Some of the advantages of CF or D-MaMIMO are summarised below:

- **High Energy Efficiency:** According to [47], the energy efficiency (EE) of the network MIMO is restricted because of the power consumption of fronthaul links. However, in D-MaMIMO, selecting the nearest APs to serve the UEs and optimum power control scheme, it is possible to improve the EE more than tenfold compared to centralised MIMO [50][51][52].

- **Flexible and Cost-Efficient:** Unlike centralised MaMIMO, D-MaMIMO exploits arrays with a smaller number of antennas, which makes it feasible for even an indoor environment. Moreover, for a heavily loaded CF-MIMO network, multiple CPUs can

support the clusters of APs. It is also seen that the implementation and operation cost of CF architecture is lower than network MIMO [47][53].

- **Uniform Quality of Service:** In contrast with the small cell system where the UEs are served by a single nearest antenna, the D-MaMIMO architecture offers transmission from multiple nearby APs to help ensure a more uniform quality of service [47].
- **Reduced Handover:** For the dynamic user support the distributed approach can minimize the unnecessary handovers with the increased number of APs [54].

2.4.2.2 Benefits of CF or Distributed Approach over Centralised System

From the discussion it is clear that, CF or D-MaMIMO concept is gaining higher attention due to its additional benefits over centralised MaMIMO [55]. There are some studies that focused on the comparison between D-MaMIMO and centralised or collocated MaMIMO to establish which of the two is better in terms of performance. It is seen that centralised antenna arrays have the leverage of low backhaul overhead to distributed antenna arrays (DAA). However, the DAAs may be able to achieve diversity in LoS channels and thus providing greater coverage at the expense of higher backhaul overheads [56][57]. According to [58][57], a centralised antenna array system improves the user separation but the performance suffers due to poor scattered environment. On the other hand, the DAAs exhibit better user separation capability compared with a collocated antenna array (CAA) in LoS environment for all types of fading scenarios. [57] shows the performance comparison between CAA and DAA regarding throughput, channel hardening, array gain and channel orthogonality for some dense network scenarios for the NLoS case and the study shows that the performance improves with increasing number of antennas in a distributed manner. Large collocated antennas at a single BS can face channel correlation issue for centralised MaMIMO [59]. [60] proposes an uplink achievable sum-rate comparison for distributed and centralised MaMIMO by determining the spatial correlation matrices. The results shows that for a given coverage area distributing the antennas provides better performance. In [61], the authors addressed an important question of whether non synchronized distributed arrays (DA) can outperform centralised arrays and showed that for a factory indoor environment, DAs can overcome the channel outages due to fading or blocking and provide a better link-reliability. Moreover, [62] also showed remarkable power and capacity enhancement for distributed arrays over centralised arrays. In [63], the authors have made the comparison based on the area spectrum efficiency (ASE) and area energy efficiency (AEE). The results revealed that increasing the number of antennas improves both ASE and AEE but increasing the distribution factor of the

massive number of antennas improves only the ASE on every occasion. They also suggested to keep the number of antennas in each distributed cell small. The spectral efficiency (SE) could also be increased even when inter-cell interference is present in distributed antenna system (DAS) [64][65]. [66] has considered scattering environment for distributed multi-user (MU) MaMIMO and CAA system using hybrid beamforming architecture and as expected distributed MU-MaMIMO outperforms CAA system. Li et al. investigate a downlink MU mmWave MaMIMO system for both centralised and distributed MIMO where both large and small scale fading are present. The performed hybrid pre-coding algorithm and it is seen that the D-MIMO system outperforms the C-MIMO system [67].

2.4.2.3 Some Related Works on CF or D-MaMIMO

A large body of research has focused on the measurement and analysis of the channel to support the advantages of using distributed large antenna array systems. In [68] Interdonato et al., have used coherent transmission for the multiple-users in D-MaMIMO system to eliminate the interference between cells exploiting macro-diversity. They also addressed the challenges due to excessive back/front-haul overhead. CF-MaMIMO is investigated in [69] for multiple users to enhance the spectral efficiency through conjugate beamforming, perfect channel estimation, non-orthogonal pilot sequences and power control coefficients and showed improved throughput per UE. The research paper [70] proposed a novel inter-cluster combining method (ICCM) to achieve precise calibration for practical implementation of D-MaMIMO systems. Hence, this reduces the complexity of backhauling. [71] has investigated the scalability of D-MaMIMO and the synchronization of the access points for practical deployment. In order to incorporate intelligent coordinated directional D-MaMIMO, several aspects should to be taken into consideration such as synchronization and tracking of independent oscillators, low-latency, form factor and economic constraints to make the distributed transmission and reception coherent. The authors in [72] proposed an algorithm based on deep learning for a CF MaMIMO to observe a mapping between the large scale fading components and the power elements obtained from the small scale fading coefficients and the results shows that the possible uplink sum rate of the cell-free massive MIMO system was greatly increased by the suggested LSF-DL-based power control approach. In [73] the authors investigated the uplink max-min SINR issue for CF MaMIMO systems, and proposed an ideal method to increase the minimum uplink user rate.

2.4.3 mmWave CF or D-MaMIMO Communication

It is evident from the research studies that to deal with the intensified data requirement in the 5G wireless communication due to an ultra-dense network, exploiting the substantial amount of available mmWave frequency range is inevitable. Subsequently, a great amount of work is dealing with mmWave communication applied to a CF-MaMIMO architecture. mmWave communication and CF-MaMIMO go hand-in-hand as they have the ability to support short range links for both indoor and outdoor environment [47]. The shorter wavelength and path-loss in the mmWave band calls for macro diversity from a large number of APs and reduced AP-UE distance without any cell constraints. Moreover, the narrow beams and higher gains establish a significantly strong communication link between APs and UEs [22][74] and the path diversity suppresses the blocking problem of mmWave [16]. However, one of the impediments of mmWave D-MaMIMO is the design of the system with low hardware and algorithm complexity. Some of the persistent concerns in designing mmWave D-MaMIMO are the channel impulse response (CIR), the increasing RF chain and front/back haul load, and the complexity in hardware and channel estimation, [47][74]. The performance of mmWave CF-MIMO can be affected by the fronthaul capacity. The increase in quantization noise under low capacities of fronthaul degrades the overall performance [74]. Furthermore, for providing dynamic user support, mmWave CF-MaMIMO faces difficulty with lack of LoS links [74]. [6] suggests that large scale antenna array (LSAA)-aided mmWave systems considering propagation measurement, can sufficiently minimise the likelihood of outages and provide a reasonable compromise between network complexity and coverage enhancement in 5G mmWave mobile communications. Furthermore, it is important to consider the hardware design carefully in MaMIMO BSs while providing high spectral efficiency (SE) as the level of hardware impairments (HWIs) shows the intensity of signal distortion caused by the hardware imperfections and analogue-to-digital converters (ADCs) greatly affect the signal distortion and power consumption. In [75], the authors looked at how to allocate HWI and ADC bits per BS antenna to achieve maximum SE. The results indicate that this optimization technique is particularly advantageous for CF-MaMIMO systems.

2.4.3.1 Channel Model

Based on the network architecture of D-MaMIMO, which brings APs closer to users, several researchers have modelled the channel as a Ricean fading channel [76][77][78][79] because of the availability of LoS paths between UEs and APs up to 300 metres [74]. According to [80], for indoor mmWave multipath propagation channel, the information regarding the

positions and the electromagnetic characteristics of all scatterers are important to estimate the multipath components. When such data is unavailable, statistical parameters and models can be employed to define the channel's general features. In addition, strong correlation may occur due to mmWave large tightly-packed transmitter receiver arrangements. Also [47] considers the small-scale fading channel in mmWave CF-MaMIMO. A modified clustered channel model is used in [35][81] incorporating the mmWave propagation. [82][83] [84] shows the cases where the APs are equipped with multiple antennas but UE end are single antennas. On the other hand, [85][86][87][88] utilize both APs and UEs with multiple antennas. Different antenna array pattern are used such as linear arrays ([85][86]) and uniform planar arrays ([82][83] [84][87][88]).

2.4.3.2 Channel Estimation

One of the major considerations for mmWave CF-MaMIMO system is to determine the accurate CSI over this wide bandwidth. Therefore, the simplest solution for acquiring channel state information (CSI) in MaMIMO is to assume perfect CSI is available at the UEs for both the downlink (DL) reception or uplink (UL) transmission which also imposes a restriction on the system design. The number of antennas at the BS must be much bigger than the total number of UE antennas [88][89][90]. Therefore, the authors in [91] study an approach that can omit this MaMIMO design restriction by optimizing a generalized eigenvalue problem. It selects BF vectors based on the signal-to-leakage ratio (SLR). Besides, as mentioned before highly correlated AP-UE channels may occur due to the large number of antennas compacted in a small area. Therefore, different pilot schemes are proposed such as non-orthogonal pilot sequences in [85][86] and sub-optimal pilot allocation [82] to eliminate the pilot contamination. Moreover, in [87] deep-learning based channel estimator is used.

2.4.3.3 Ul and DL Transmission

Several pre-coding schemes are applied to achieve the desired DL/UL data rates. In [85], the authors use zero-forcing (ZF) pre-coding on the DL and ZF detection for the UL. But due to the increasing RF chain complexity hybrid pre-coding and detection schemes are proposed to reduce this. Moreover, selecting a set of APs for active UEs can sufficiently boost the achievable energy efficiency. It can be done by dynamically activating/deactivating the AP selection based on statistical distribution of users [74]. In [92], the authors proposed a new joint maximum-ratio and zero-forcing (JMRZF) pre-coding scheme. They applied an AP subset selection scheme based on large-scale fading coefficients to perform centralized ZF

and the remaining APs apply simple maximum-ratio transmission (MRT). This approach can approximately obtain the spectral efficiency that is achievable by using centralised ZF with a substantial reduction in the front-haul overhead.

2.5 Arrays and Beamforming

2.5.1 Antenna Arrays

2.5.1.1 Array Basics

For high speed communication, large directional gain is required and in particular, for 5G wireless networks which promise high data rate for uninterrupted transmission using mmWave band frequency. Assembling multiple antenna elements into a single electrical and geometrical unit is referred to as an antenna array. Generally, an array consists of similar radiating elements to avoid complexity. The minimum number of elements required to form an array is 2 and it can go up to several thousands depending on the desired gain. An antenna array facilitates a system with following benefits:

- Ensure higher gain and directionality than a single element antenna
- Eliminate interference at the receiver end
- Steer the main beam to a particular direction
- Estimate the AOA of the incoming signals
- Maximize the signal to interference plus noise ratio (SINR)

An array combines the signal from each of the elements to provide improved performance. In order to produce a highly directional array, constructive interference of the fields from the elements of the array is required in the intended direction. The following controlling factors can shape the pattern of the array:

- different geometrical arrangement of arrays such as linear, circular, rectangular, spherical, etc.
- the distance between two adjacent elements
- the excitation amplitude and phase of individual elements

- the respective pattern of the individual elements

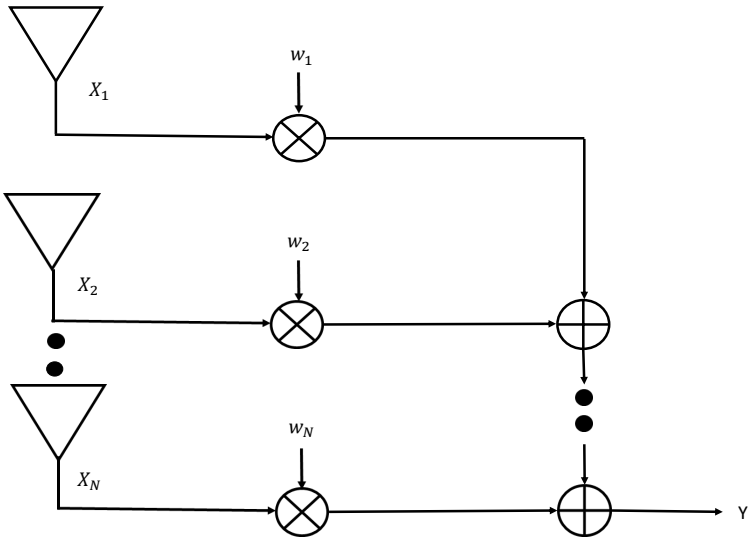

Fig. 2.4 Weighting and summing of signals by an antenna array consists of N elements [93]

Let us consider an array with N antenna elements those outputs are $X_1, X_2, \ldots X_N$. These outputs are then multiplied by a particular set of N weights $w_1, w_2, \ldots w_N$. The basic diagram for an antenna array with N elements is shown in Fig. 2.4. Then the output of an antenna array can be given as

$$Y = \sum_{n=1}^{N} w_n X_n \tag{2.6}$$

This is the basic principle for antenna array signal combining from individual elements [94][93].

Array Factor

Let us consider a two element antenna array, shown in Fig. 2.5, where the elements are at a distance d_l. From observation point P, the distance to the elements are r_1 and r_2 respectively. The angle of arrival is considered as θ. When the signals from two elements interfere constructively then it is said to be "in phase" and for destructive interference it is "out of phase". In Fig. 2.5a, the signals from two elements are meeting at a point P. The path difference has to be determined in order to measure whether the signal are "in phase" or "out of phase". If we move the point to the far field then the paths r_1 and r_2 will become parallel as shown in Fig. 2.5b.

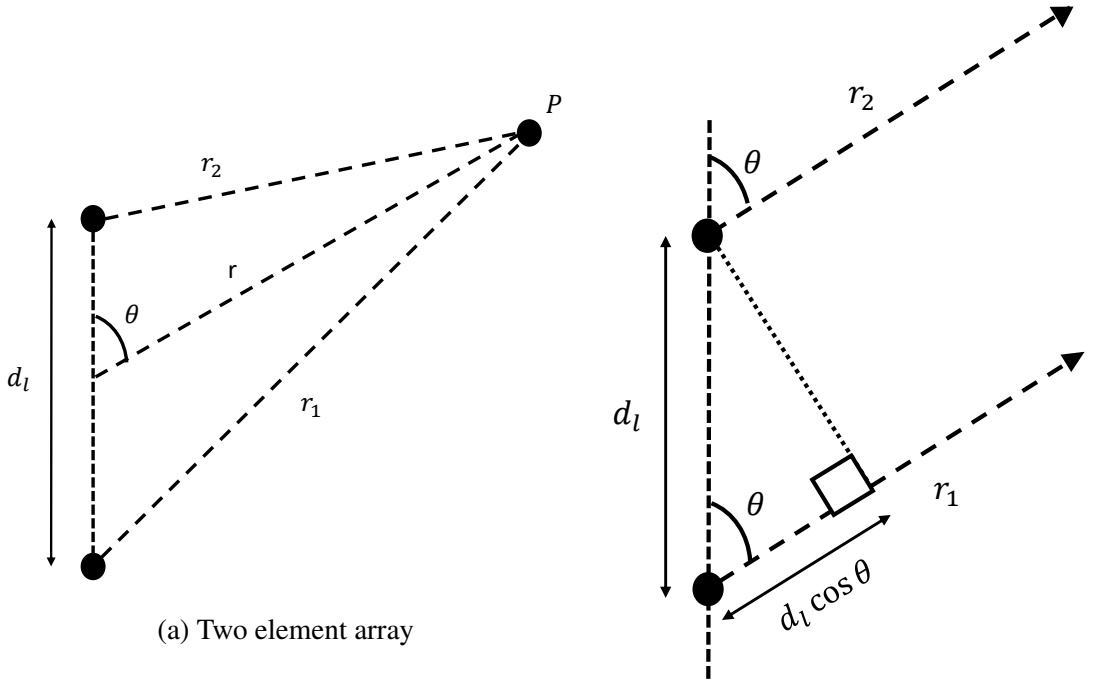

(a) Two element array

(b) Far field observation

Fig. 2.5 Geometry of a two-element array [94]

Now, the path difference between r_1 and r_2 is given by $d_l \cos\theta$. By multiplying this path difference with the wave number k we can calculate the phase difference, γ_d. Therefore,

$$\gamma_d = k d_l \cos\theta \tag{2.7}$$

If δ is assumed to be the difference in phase excitation between the elements, then overall phase difference becomes,

$$\gamma_d = k d_l \cos\theta + \delta \tag{2.8}$$

The total field radiated is equal to the sum of the electric fields of these two elements is given by

$$E(\mathbf{r}) = E_1(\mathbf{r}) e^{j\gamma_d/2} + E_2(\mathbf{r}) e^{-j\gamma_d/2} \tag{2.9}$$

where $E_1(\mathbf{r})$ is the electric field of the first element and $E_2(\mathbf{r})$ is the electric field of the second element.

For two identical antenna elements, this equation can be rewritten as

$$\begin{aligned} E(\mathbf{r}) &= E_1(\mathbf{r})\left(e^{j\gamma_d/2} + e^{-j\gamma_d/2}\right) \\ &= 2E_1(\mathbf{r})\left(\frac{e^{j\gamma_d/2} + e^{-j\gamma_d/2}}{2}\right) \\ &= 2E_1(\mathbf{r})\cos\left(\frac{\gamma_d}{2}\right) \end{aligned} \tag{2.10}$$

Substituting (2.8) into the above equation gives:

$$E(\mathbf{r}) = 2E_1(\mathbf{r})\cos\left(\frac{kd_l\cos\theta + \delta}{2}\right) \tag{2.11}$$

Therefore, it is seen from above equation that the electric field of a single antenna ($E_1(\mathbf{r})$) is multiplied by a new factor called "array factor" to obtain the total field of the array. Hence,

$$(AF)_n = \cos\left(\frac{kd_l\cos\theta + \delta}{2}\right) \tag{2.12}$$

is the normalized form of array factor [94][95].

2.5.1.2 Antenna Array Types

Antenna arrays can be divided into several types depending on the arrangements of the element, radiation pattern and spacing between them. The choice antenna array depends on the desired application. Linear array, planar array, circular array are few among them. We will discuss linear and planar antennas in this section.

Linear Array

When all the elements in an array are arranged in a long straight line, it forms a linear array. Linear arrays can be uniform or non-uniform. If all the elements in an array have uniform spacing between them, is called uniform array. Fig. 2.6 represent the geometry of an uniform linear array with N elements. It is an extension of Fig.2.5.

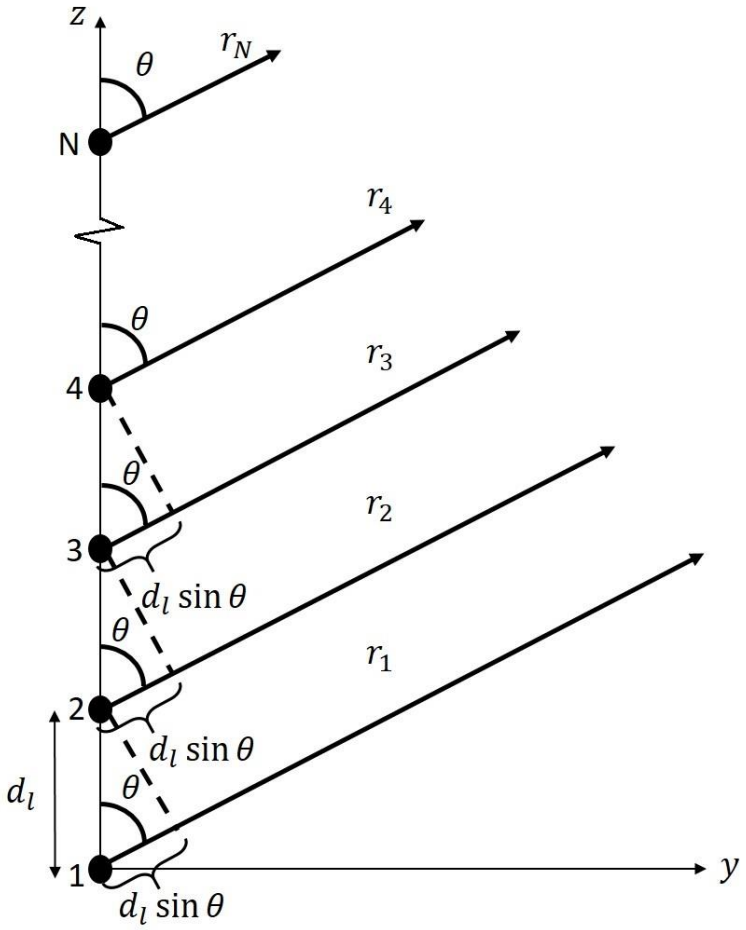

Fig. 2.6 Far-field geometry of a linear array [93]

The total field can be determined by multiplying the field of a single element of the array by the array factor of the array elements, in the case where the original elements of the array are not isotropic sources. The array factor for the linear array can be written as

$$\begin{aligned} AF &= 1 + e^{+j(kd_l\cos\theta+\delta)} + e^{+2j(kd_l\cos\theta+\delta)} + \cdots + e^{j(N-1)(kd_l\cos\theta+\delta)} \\ &= \sum_{n=1}^{N} e^{j(n-1)(kd_l\cos\theta+\delta)} \end{aligned} \tag{2.13}$$

That can be also written as

$$\begin{aligned} AF &= \sum_{n=1}^{N} e^{j(n-1)\gamma_d} \\ \text{where } \gamma_d &= (kd_l\cos\theta+\delta) \end{aligned} \tag{2.14}$$

Some examples of uniform linear arrays are the broadside array, ordinary end-fire array, Hansen-Woodyard end-fire array and scanning array whereas binomial and dolph-tschebyscheff array are the types of non-uniform array [93].

Planar Array

In a planar/rectangular array, the elements are placed in 2D rectangular grids which adds another dimension to control and shape the pattern of the array. Some exciting features of planar arrays are the flexibility to move the beam in both vertical and horizontal direction, and ability to produce symmetrical beam shape with lower side lobes [93].

Fig. 2.7 shows a planar array where M elements are arranged in the x-axis and N elements in the y-axis and form an $M \times N$ array.

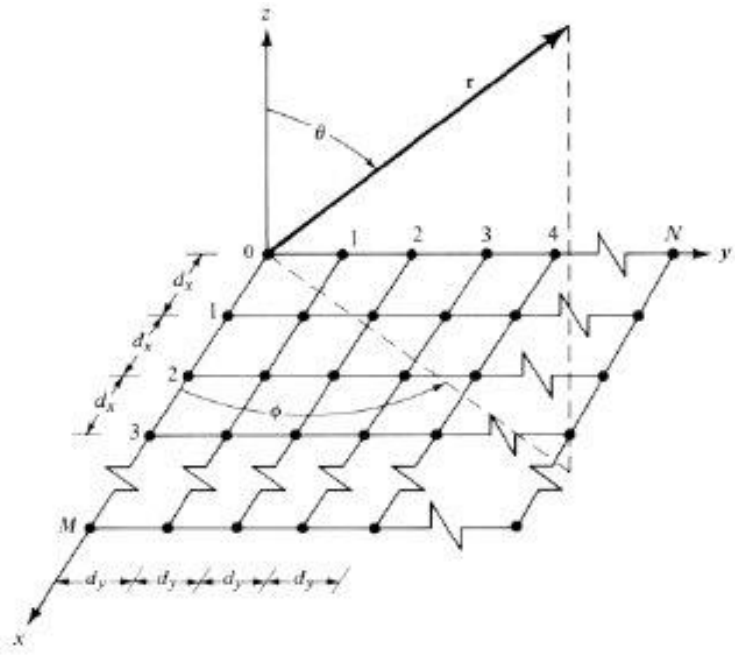

Fig. 2.7 Planar antenna geometry (directly reproduced from [93])

The element spacing in the x-direction is denoted as d_x and in the y-axis it is d_y and the progressive phases are δ_x and δ_y in the respective directions. θ and ϕ are the azimuth and elevation angles. Therefore, the antenna factor is given by

$$AF = \sum_{n=1}^{N} I_{1n} \left[\sum_{m=1}^{M} I_{m1} e^{j(m-1)(kd_x \sin\theta\cos\phi+\delta_x)} \right] e^{j(n-1)(kd_y \sin\theta\sin\phi+\delta_y)} \tag{2.15}$$

or

$$AF = S_{xm} S_{yn} \tag{2.16}$$

where

$$\begin{aligned} S_{xm} &= \sum_{m=1}^{M} I_{m1} e^{j(m-1)(kd_x \sin\theta\cos\phi+\delta_x)} \\ S_{yn} &= \sum_{n=1}^{N} I_{1n} e^{j(n-1)(kd_y \sin\theta\sin\phi+\delta_y)} \end{aligned} \tag{2.17}$$

According to (2.16), the planar array pattern is the product of the array factors of the arrays in the x and y directions.

If the amplitude excitation coefficients in the y-axis are are proportional to those along the x axis, then the amplitude of the $(mn)^{th}$ element is

$$I_{mn} = I_{m1} I_{1n} \tag{2.18}$$

For the uniform amplitude excitation of the array, $I_{mn} = I_0$. Then the array factor for planar array becomes

$$AF = I_0 \sum_{m=1}^{M} e^{j(m-1)(kd_x \sin\theta\cos\phi+\delta_x)} \sum_{n=1}^{N} e^{j(n-1)(kd_y \sin\theta\sin\phi+\delta_y)} \tag{2.19}$$

When the main beam is pointing in the $\theta = \theta_0$ and $\phi = \phi_0$ direction, the directivity, D_0 of planar array is therefore,

$$D_0 = \frac{4\pi \left[AF\left(\theta_0, \phi_0\right)\right] \left[AF\left(\theta_0, \phi_0\right)\right]^H |_{max}}{\int^2 \pi_0 \int_0^{\pi} \left[AF\left(\theta_0, \phi_0\right)\right] \left[AF\left(\theta_0, \phi_0\right)\right]^H \sin\theta d\theta d\phi} \tag{2.20}$$

The directivity of an antenna is the ratio of the radiation intensity in a particular direction from the antenna to the radiation intensity averaged across all directions. The average radiation intensity is equal to the total power radiated by the antenna divided by 4π. The direction of maximum radiation intensity is presumed if the directions are not provided.

2.5.1.3 Antenna Arrays in mmWave D-MaMIMO

From the above literature in Section 2.3 and 2.4, we have come to know that antenna array directionality is essential to operate in the mmWave frequency band and the MaMIMO architecture is the means to achieve the high gain to fulfil the 5G network requirements.

Distributed antenna arrays enable the coherent transmission through distributed beamforming which expedite the system with following benefits [96]:

- Enhanced Signal Gain
- Increased Reliability
- Scalability of the number of nodes
- Greater Spatial Diversity

However, to make the most of the spectrum, the 5G network will use both high and low frequencies. Hence, the antenna design in this kind of multi-system network will be challenging in terms of array coupling, high power heat dissipation, reliability and phase consistency in MaMIMO architecture [97]. Moreover, using 2D antenna array is possible to thrust the energy in both vertical and horizontal direction. Hence, 3D beamforming is proven beneficial for connecting users at different heights and locations [98] in a mmWave MaMIMO system. The specific use of antenna arrays for beamforming is discussed in the following section.

2.5.2 Beamforming

In future wireless communication, it seems that the major challenge will come from the immensely increased number of users with various applications and the heterogeneous nature of the network serving many different smart gadgets. So far from the discussion in Sections 2.3 and 2.4, we have come to understand that mmWave and D-MaMIMO are two of the complementary key enabling technologies for the services promised in 5G.

Fig. 2.8 Beamforming technique

A MIMO wireless communication system provides several ways to transmit the information signal and two of them are: Spatial Multiplexing and Beamforming (BF). In spatial multiplexing, data signals are transmitted independently over separately encoded streams, which are also known as "layers", from each of the multiple antennas [99][100]. On the other hand beamforming incorporates adaptive antenna array systems in which directional antenna beam patterns are produced using multiple antennas to steer the transmitted signal toward a desired user location. Fig. 2.8 is the visual representation of the BF process. An antenna array can create multiple beams at a time to serve multiple UEs. In this technique, signal strength is increased to improve SINR through coordinating the phases of transmitted signals and reduction of interference [94]. While, BF proves to be a better approach in terms of low complexity, spatial multiplexing, in general, yields the maximum channel capacity [101]. Beamforming becomes effective with larger numbers of transmit antennas (as in massive MIMO) as it reduces interference when there are many users and makes better use of the spectrum around them [102]. Progressive works have been done to study different aspects of beamforming and its implementation in mmWave Ma-MIMO . Other techniques like pre-coding, spatial filtering are essentially the same as the BF technique [103][104].

In BF, the main beam steers the maximum radiation of the antenna pattern toward the signals-of-interest (SOI) and place nulls toward the signals-not-of-interest (SNOIs). Moreover, changing the direction of the array when transmitting, a beamformer controls the phase and amplitude of the signal at each transmitter [98].

According to [105], the transmit BF directs the signal energy by assigning an individual BF vector towards a particular user hence can serve multiple spatially separated users simultaneously. However, the spatial directivity is limited by the finite number of antennas, and as a result, the users experience energy leakage which causes further interference. They propose an optimization of multi-user transmit BF where they choose the optimal BF vector to enhance the signal power at the desired user while reducing the interference due to energy leakage. However, [106] describes this solution as time consuming and comes up with an alternative optimization proposal where the BF vectors are determined by the distribution of interference i.e. the poor channels will have lower interference and vice versa.

Beamforming schemes calculate the detection and pre-coding matrices based on matrix $\mathbf{H}$ between the AP and the UE. Hence, Some of the popular linear pre-coding/detection methods are: Maximum Ratio (MR), Zero Forcing (ZF), and Minimum Mean-Square Error (MMSE). The MR technique is applied to maximize the signal-to-noise ratio (SNR) and it is carried out assuming that the detection/precoding matrix is just the conjugate transpose or conjugate of the CSI matrix, $\mathbf{H}$. In MR,

$$\tilde{\mathbf{s}} = \mathbf{H}^H \mathbf{y} \text{ (detection)}, \text{ and } \mathbf{x} = \mathbf{H}^* \mathbf{s} \text{ (pre-coding)}$$

The Zero Forcing (ZF) pre-coding addresses the inter-user interference issue for the multi-user scenario. ZF linear beamforming is the process of inverting the channel matrix at the transmitter to create orthogonal channels between the transmitter and the receivers. In ZF,

$$\tilde{\mathbf{s}} = \left(\mathbf{H}^H \mathbf{H}\right)^{-1} \mathbf{H}^H \mathbf{y} \text{ (detection)}, \text{ and } \mathbf{x} = \mathbf{H}^* \left(\mathbf{H}^T \mathbf{H}^*\right)^{-1} \mathbf{s} \text{ (pre-coding)}$$

The MMSE approach tries to minimize the overall error due to both interference and noise, by balancing between interference nulling and noise enhancement. In MMSE,

$$\tilde{\mathbf{s}} = \left(\mathbf{H}^H \mathbf{H} + RI\right)^{-1} \mathbf{H}^H \mathbf{y} \text{ (detection)}, \text{ and } \mathbf{x} = \mathbf{H}^* \left(\mathbf{H}^T \mathbf{H}^* + RI\right)^{-1} \mathbf{s} \text{ (pre-coding)}$$

It introduces a regularization term R to solve the optimization problem between the noise covariance and the transmit power. This MMSE technique is aslo referred as Regularized Zero Forcing (RZF) [107].

Based on the directions of the beam patterns BF can be classified into two categories: 1) 2D beamforming and 2) 3D beamforming.

2.5.2.1 2D Beamforming

In 2D beamforming (2DBF) the antenna elements at the BS or the AP are engaged along the horizontal axis to cover beam pattern radiation in the horizontal plane. 2DBF can offer frequency reuse, reduces inter-user interference and enhances cell capacity. Instead of omnidirectional antennas, the 2DBF provides directionality, and if a cell has more than one antenna, multiple beams can be produced to serve a large number of users in the desired direction. BF and MIMO schemes are extensively used to produce the horizontal beam pattern of mobile wireless base stations (eNodeB) to maximize performance [108].

2.5.2.2 3D Beamforming

3D beamforming (3DBF) is being considered as one of the promising technologies for mmWaves MaMIMO to serve the users at different heights. In 3DBF the radiation beam patterns are modelled to manoeuvre in both the elevation and azimuth direction, to provide more degrees of freedom, and thus it adds one more dimension to the BF scheme. This is called 3DBF. The beam moving along horizontal direction forms azimuth angle (θ) and for the vertical direction, it is elevation angle (ϕ). Fig. 2.9 shows the side and top view of the elevation and azimuth angle respectively in 3DBF technology.

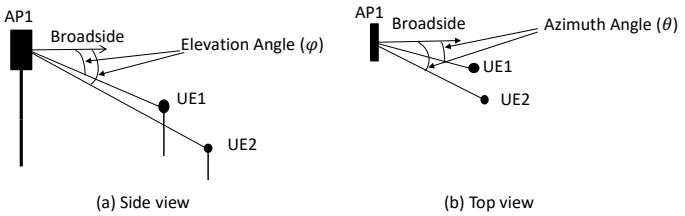

Fig. 2.9 Beamforming angles (a) Elevation angle (b) Azimuth angle

The main idea is to adapt the vertical dimension of the antenna radiation pattern and to steer the transmitted energy in a vertical direction, as in BF or pre-coding in the horizontal plane. The main advantages of 3DBF are: higher user capacity, less inter-cell and inter-sector interference, higher energy efficiency, improved coverage and increased spectral efficiency. In addition, it will make the installation locations for APs more flexible as it is able to serve the users at different altitudes with the help of down-tilt and up-tilt.

Several limitations need to be accounted for to adjust the 3D antenna geometry. 3DBF using an active antenna system (AAS) that works in both directions, regulating the antenna weights of the horizontal antenna terminals and also of each antenna element in the vertical direction. Thus, the transmit power can be better concentrated on the targeted UEs and the interference can also be reduced. The adjustment range of the vertical beam pattern is much less than in the horizontal direction. Further, the vertical beam usually is much narrower than the horizontal beam and the half-power beam-width (HPBW) is typically in the 5° to 10° range. So, the vertical beam requires a higher accuracy of the down-tilt adjustment, to improve vertical beam separation. The way to get a narrow vertical beam is to arrange a large number of transmitting elements vertically and feeding the same signal with proper phase shift between the transmitting elements. The downtilt adjustment can be realized by selectable passive feeding networks. This approach is suitable for adapting the downtilt of the full signal bandwidth but for the 3D beamforming approach dynamic beam pattern adaptation per assigned resource block is required i.e., per UE. Therefore, each transmitting element must be intended to transmit each frequency sub-band with a specific phase shift [98][108].

In [109] Nima et al. propose a transmission technique to reduce the inter-cell interference by coordinated 3D beamforming. In the horizontal side, the main focus was on inter-cell interference cancellation (ICIC) depending on the reduced CSI delay. On the other hand, in the vertical plane, the focus was on with inter-cell interference control using the elevation tilt to the locations of the targeted users. The result showed that the technique can achieve a

substantial performance gain in edge and peak throughput over conventional non-coordinated transmission system. The literature [110] focuses on the joint optimization of 3DBF and resource allocation for the small cell (SC) backhaul in HetNets. They developed a low-complexity algorithm for joint 3DBF and resource allocation and the simulation results shows the better performance of the proposed algorithm.

Deployment of 3DBF would play a pivotal role considering the high path and penetration losses at mmWave communication. The mmWave frequency spectrum, massive multiple-input multiple output systems, and ultra dense networks (UDNs) are expected to be possible candidates that can increase system capacity to meet new requirements of 5G [111]. BF is being thought of a key enabler for mmWave indoor and outdoor backhaul networks. The propagation characteristic of mmWave is characterized by a mix of LoS and NLoS propagation with varying reflections and the major challenge is to ensure accurate pointing and tracking under varying propagation conditions. Large scale antenna systems (LSAS) need to be planned with practical optimization for RF chains for transceiver to balance energy and spectrum efficiency [112].

2.5.2.3 Beamforming in Multipath Environment

Multipath occurs when a signal takes two or more paths from the transmitting antenna to the receiving antenna. In urban and rural environments, the signal might reflect off buildings, mountains or other obstacles. For multipath propagation, the challenge is to determine different angle of arrival (AOA) for both LoS and NLoS components. Generally, the AOA estimation is done at the AP side [113]. The authors in [114] constructed the optimal beamformer using a two tier eigen structure analysis of the array covariance. They showed that their constructed beamformer was considerably more advantageous than the usual beamformers in multipath fading environments. Conventional adaptive BF techniques do not perform well in the multipath environment. The multipath narrowband propagation creates coherence and it affects the performance of an adaptive array system. To overcome this problem, Liu and Langley proposed a robust adaptive BF technique called domain weighted principle component analysis (DW-PCA) for the multipath environment. The results confirmed that the DW-PCA was capable of giving a better performance than the fixed BF under the scenario of an interfering signal falling in the main beam of the fixed BF [115]. [113] proposed an approach by changing the directional property of the smart antenna array at both ends for indoor multipath scenario. In their proposed model they combine the transmitter and receiver beam steering to overcome the effect of multipath propagation. Due to mmWave scattering behaviour it is important to study the BF approach

for a multipath channel. To mitigate the attenuation problem, single beams from transmitter and receiver side are steered towards each other to reach the desired gain. However, it is not a robust approach due to blocking and reflection. Hence, a joint BF scheme using both transmitter and receiver has been proposed to provide the diverse gain [116]. While the mmWave spectrum promises far higher bandwidths than current cellular allocations, there is concern that mmWave transmissions will have significantly less favourable propagation due to severe shadowing, intermittent connectivity, and presence of higher doppler spreads. As a result, the application of mmWave bands for multipath or NLoS cellular scenarios and across long distances needs careful consideration, and the practicality of such systems has been widely discussed [117]. Hence, channel models capturing these multipath effects are studied widely. [118] provides a measurement based study on mmWave outdoor multipath scenario using BF. They exploit various types of directional antenna at different heights to estimate the AOA, multipath time delay spread, and propagation path loss. Multipath propagation of mmWave and related issues are further discussed in Chapter 6.

2.5.3 mmWave MaMIMO Beamforming

A Beamforming technique along with the MaMIMO architecture can radiate the maximum energy by steering the beams more accurately towards individual UE, hence the challenges of mmWave propagation. So, it can be said, to support the 5G data surge exploiting mmWave frequency band, MaMIMO and BF work hand in hand and can enhance user throughput, boost mobile network capacity, raise spectral and energy efficiency [119][120]. However, BF for mmWave communications throws challenges due to the large channel bandwidth, unique channel characteristics, and RF transceiver architecture design [112]. Fig. 2.10 shows the MaMIMO BF environment.

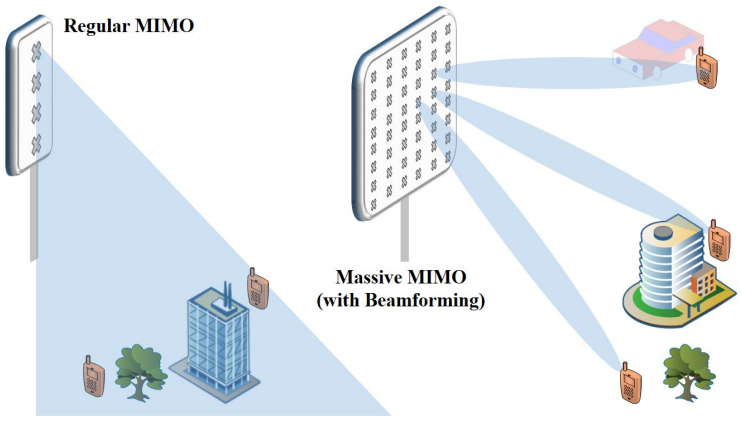

Fig. 2.10 Massive MIMO with beamforming (directly reproduced from [121])

In conventional beamformers large antenna elements are connected to the RF chains and the phase shifters and/or the RF switches provides the the beamforming and beam selection. For mmWave frequencies, phase shifters and switching networks necessitate the inclusion of RF components as well as voltage control from a hardware standpoint [122]. Moreover, one advantage of mmWave is its LoS nature which helps to control interference between systems. The small wavelength at mmWave frequency facilitates the implementation of multiple arrays within a small area and the support of BF with high directional gain that makes it possible to utilize the spatial dimension efficiently. The mmWave antennas are likely to be highly directional and in consequence the LoS plays a dominant role in propagation. However, for the LoS channel, MIMO BF system performance relies heavily on the number of arrays and the distances from surrounding arrays [123]. If the LoS component is dominant, then MaMIMO is more compatible in Ricean fading environments rather than of a Rayleigh fading environments when the scattering loss is considered [124]. As mentioned before BF processes the signal by adjusting the phase and/or amplitude, before transmitting it and therefore enhance the network throughput and reliability in a MIMO system. The BF can be designed in three different ways: analogue beamforming, digital beamforming, or a hybrid beamforming architecture. [125].

2.5.3.1 Analogue Beamforming

Analogue BF only exploits the phases of the transmitting signal to concentrate the maximum energy towards intended user. Therefore, in order to transmit a single beam in this process a single RF chain is sufficient, along with a large number of analogue phase shifters. The RF chain controls the phase and thus provides the gain. Clearly, analogue BF is simpler in terms

of hardware design and low power consumption but it falls short in terms of poor antenna gain and performance loss due to the inability to control the amplitude. In addition, analogue beamforming requires to measure CSI precisely. As a result, it is not feasible to use analogue BF practically [125]. However, there are some proposed solutions to avoid the complexity of CSI in [126][127][128].

2.5.3.2 Digital Beamforming/Pre-coding

Unlike analogue BF, digital BF uses RF chains for each antenna element to control both the phases and the amplitudes in the digital domain. Often digital beamforming is referred as pre-coding and the precoders are formed in the digital baseband. Due to the increased number of RF chains required, it is costly to adapt digital BF for mmWave MaMIMO [125][129]. Several solutions have been proposed to implement digital BF for 5G communication requirements. [129] shows the performance of MaMIMO system comparing two digital BF technologies (grid of beams and eigen based BF) and studied the digital BF thoroughly for future wireless communication. [130], implied digital BF jointly with two step CSI based pre-coding utilizing low-SHF band to avoid the disadvantages due to mmWave propagation characteristics for the MaMIMO channel. In [131], the authors suggested that for a given set of parameters fully digital beamforming can be implemented reducing the hardware complexity of the RF chain. Recently, hybrid BF (described in following section) is preferred by many researchers to digital BF because of low power consumption and hardware complexity. However, hybrid BF is limited to only a few data streams using phased sub-arrays. On the contrary, digital BF can provide multiple beams and a higher number of data stream than hybrid BF. Hence, [132] shows an asymmetric MaMIMO system for the mmWave frequency band where the number of antenna elements and transmitters of the transmitter array is larger than the number of antenna elements and receivers of the receiver array and non-reciprocal full-digital BF is performed. Interestingly, it has shown the potential of reduced hardware complexity and cost along with the benefits of digital BF.

2.5.3.3 Hybrid Beamforming

Evidently, the mmWave MaMIMO has the potential to dramatically increase the network capacity so is considered as one of the frontiers of the next generation of wireless communication networks: but to bring such a concept into practice, it is essential to reduce the cost of such complex systems. Recently, hybrid/analog-digital (AD) BF structure has received great attention as a promising solution to carve the cost and power consumption. In other words, it

can be stated that merging the features of analogue and digital BF architecture, hybrid BF is a prospective candidate in mmWave MaMIMO systems [125][133]. By introducing phase shifters and reducing the number of expensive components in digital and RF chains, such as digital-to-analog/analog-to-digital converters (DACs/ADCs) and signal mixers, hybrid BF opens up possibilities to build relatively low cost and low complexity MaMIMO systems. A very common way of allowing hybrid BF is to predefine a set of fixed beams in the DL where pilots are transmitted to a UE which selects the best beam and sends feedback to the BS [134][135]. Moreover, conventional digital BF methods involve one RF chain per antenna element which is not feasible in large-scale antenna arrays due to the high cost and high-power consumption of RF chain components in mmWave. Based on the hypothesis of full CSIT, hybrid massive MIMO can achieve the same performance as any fully digital BF scheme [136].

2.6 Zero-forcing Pre-coding

MaMIMO technology has been proven to be the ultimate solution in terms of providing higher spectral efficiency to support UDNs and achieving the expected data rate in 5G cellular network. Hence, the transmission from a large number of BS antennas to multiple users requires processing at the transmitter i.e. pre-coding to send the desired data symbols towards the intended users [137]. Zero forcing (ZF) is a linear pre-coding scheme that offers higher computational efficiency. It has the capability of exhibiting equivalent performance to dirty paper coding or other advanced non-linear pre-coding schemes, in favourable channel conditions [138][139][140]. ZF provides multiplexing gain and the multi-user diversity gain and successfully mitigates the interference among the interfering users [141]. ZF pre-coding is done by inverting the multi-user channel. The pre-coder with pseudo-inverse channel provides high performance under a total power constraint [142].

Let us consider a downlink multi-user scenario where M transmit antennas are serving K users containing a single antenna in the same time-frequency.

The received signal at the k^{th} user is expressed as

$$y_k = \mathbf{h}_k^T \mathbf{x} + z_i \tag{2.21}$$

where $\mathbf{h} \in \mathsf{C}^{M\times 1}$ is the channel vector between the BSs and users, z_i is the noise and $\mathbf{x}$ the precoded signal vector $\mathbf{x} \in \mathsf{C}^{M\times 1}$ is given by

$$\mathbf{x} = \sum_{k=1}^{K} \mathbf{w}_k s_k = \mathbf{W}\mathbf{s} \tag{2.22}$$

where, $\mathbf{w} \in \mathsf{C}^{M\times 1}$ is the pre-coding vector for user k, s_k is the data symbol. $[\mathbf{W} = \mathbf{w_1}, \mathbf{w_2}, \ldots, \mathbf{w_K}]$ is the concatenated pre-coding matrix and $\mathbf{s} = [s_1, s_2, \ldots, s_K]^T$ is the data symbol vector.

Then 2.21 can be written as

$$\mathbf{y} = \mathbf{H}\mathbf{W}\mathbf{s} + \mathbf{z} \tag{2.23}$$

where $\mathbf{y}$ is the received signal vector, $\mathbf{H} \in \mathsf{C}^{K\times M}$ is the concatenated channel matrix, and $\mathbf{z}$ is noise vector.

Now, the pre-coding matrix for ZF is given by

$$\mathbf{W}_{ZF} = \frac{1}{\alpha_{ZF}} \cdot \mathbf{H}^H \left(\mathbf{H}\mathbf{H}^H\right)^{-1} \tag{2.24}$$

where $\alpha_{ZF} = \sqrt{\mathrm{tr}\{\mathbf{H}\mathbf{H}^H\}}$ is the normalization factor that ensures that the transmit signal power remains the same after the pre-coding.

Therefore by substituting 2.24 into 2.23, the received signal vector for ZF pre-coding becomes,

$$\mathbf{y}_{ZF} = \frac{1}{\alpha_{ZF}} \cdot \mathbf{H}\mathbf{H}^H \left(\mathbf{H}\mathbf{H}^H\right)^{-1} \mathbf{s} + \mathbf{z} = \frac{1}{\alpha_{ZF}} \cdot \mathbf{s} + \mathbf{z} \tag{2.25}$$

Here, ZF pre-coding suppresses the interference to zero from non-intended users hence the name zero forcing [137]. However, in massive MIMO systems, for a large number of users, the computational complexity increases in ZF precoding. The matrix inversion causes high computation cost which affects its application [140]. Moreover, this pre-coding is fully CSI based and require perfect knowledge of the CSI which is not straightforward for practical implementation [143].

There are several papers on ZF pre-coding stating different design criteria [144][145][146]. [140] modified the ZF pre-coding scheme with reduced complexity and showed better performance than the conventional ZF approach. The authors in [147] proposed a ZFBF scheme for cell-free massive MIMO (CF-MaMIMO). They optimized the combined power control coefficient and AP power to enhance the signal-to-interference-plus-noise ratio (SINR) and the rate of the system. Moreover, [143][148][149] stated different approaches to solve the CSI issue. In [65] for a MU-MIMO DAS system ZFBF is applied on the DL where they

assumed perfect CSI. The impact of channel aging on ZF Pre-coding in CF Ma-MIMO systems for user mobility and its effect on the CSI is shown in [150] .

2.7 Singular Value Decomposition

In linear algebra, singular value decomposition (SVD) is a computational technique that is used to extract useful features from a matrix by decomposing it into different component matrices. Let us consider that $\mathbf{A}$ is a $m \times n$ matrix. The SVD of $\mathbf{A}$ can be expressed as

$$\mathbf{A} = \mathbf{U}\Sigma\mathbf{V}^H \tag{2.26}$$

where Σ is a diagonal matrix where the diagonal elements are called the singular values of $\mathbf{A}$ and can be represented as

$$\Sigma = \begin{bmatrix} \Sigma_r & 0 \\ 0 & 0 \end{bmatrix} \tag{2.27}$$

where $\Sigma_r = diag\,(\sigma_1, \ldots, \sigma_r)$ and $\sigma_1 \geq \sigma_2 \geq \cdots \geq \sigma_r > 0$ and Σ is the square root of an eigenvalue of $\mathbf{A}\mathbf{A}^H$ and r denotes the rank of the matrix. Moreover, $\mathbf{U}$ and $\mathbf{V}$ are orthogonal matrices satisfying $\mathbf{U}^H\mathbf{U} = I$ and $\mathbf{V}^H\mathbf{V} = I$. In fact in each matrix a unique Σ can be found. The columns of $\mathbf{U}$ are the eigenvectors of $\mathbf{A}\mathbf{A}^H$ and the columns of $\mathbf{V}$ are the eigenvectors of $\mathbf{A}^H\mathbf{A}$ [151].

It is shown that SVD is an efficient mathematical tool for channel estimation to obtain the MIMO channel capacity [151][152]. [153] proposes a joint transceiver combination using SVD based DL MU-MIMO eigenmode transmission that effectively cancel the multi-user interference and also shows that using low complexity ZF pre-coding at the BS exhibits substandard performance. In [154], a vector perturbation (VP) aided SVD-based transmitter approach is adapted for multi-user MIMO that improves DL and can supporting different modulation techniques. Conventional ZF pre-coding is unable to control the received power at each user, and hence suffers from poor energy distribution [155]. However, using SVD provides better power balancing and furthermore, achieves improved sum capacity to conventional ZF pre-coding [156]. But SVD invokes the collaborative detection issue. In [157] the MU-MIMO collaborative detection problem is addressed and proposed a possible solution exploiting SVD to mitigate the user interference. [88] discusses an approach using SVD-based pre-coding combined with ZF pre-coding to eliminate user interference addressing the importance of obtaining the CSI for CF-MaMIMO architecture.

2.8 Summary

In this chapter, an overview of the current state-of-art for 5G and the techniques relevant to this thesis has been documented. In addition, research carried out on distributed massive MIMO in mmWave communication have been reviewed. We have obtained the generic idea on the requirements, challenges and existing scenarios. It has been seen that several factors need to be considered in implementing D-MaMIMO scheme in the mmWave band for future wireless technologies due to the unique propagation characteristics of mmWave. The basic principle of some of the beamforming techniques are also discussed. The following chapter will present the first phase of the major contributions in this thesis.

Chapter 3

Distributed 3D Beamforming for a Single User

3.1 Introduction

Two of the most promising features of 5G and beyond are massive multi-input-multi-output (MaMIMO) and millimetre wave (mmWave) transmission. The size of an antenna element at mmWave frequencies is much reduced, and the array element spacing (usually half the corresponding wavelength) can also be reduced, making large-scale antenna arrays feasible within a limited physical size. The increased free-space path loss (FSPL) at these frequencies also requires increased antenna gain in compensation, along with steerable beams, which also calls for large-scale arrays. Moreover, additional propagation issues may also arise at mmWave frequencies, for example the increased diffraction loss may mean that line-of-sight (LoS) or strong specular reflections are required to provide strong signals to users. This (along with the increased FSPL) makes it desirable to reduce the distance between UE and AP [11][44][158][26]. Distributed massive MIMO (D-MaMIMO) or cell-free massive (CF-MaMIMO) offers fair coverage by exploiting base station diversity or macro-diversity and path loss reduction along with other advantages such as large throughput, coverage probability, and energy efficiency [55]. A large number of works have considered CF-MaMIMO or D-MaMIMO, but these mostly consider the band below 6 GHz. The comparison between collocated and fully distributed antenna systems has been made in [159][160][161][162]. In [163][16][86], a distributed approach is studied assuming multi-antenna APs, but not explicitly arranged in antenna arrays such as will be required at mmWave.

In this chapter, a practical LoS model is used, considering the 3GPP standard [164] for high frequency to analyse the key trade-offs in D-MaMIMO or CF-MaMIMO to collocated

massive MIMO, between concentrating the antenna elements in one location versus distributing the total elements over multiple APs in arrays with smaller numbers of elements. Therefore, we consider the application of D-MaMIMO, assuming that in place of a single centralized large antenna array, a number of arrays are distributed as APs across the service area. These then perform cooperative beamforming: they jointly steer coordinated beams in the direction of UE. Distributing the antennas across a larger number of APs means that on average users are closer to APs, and hence there is a higher probability of a line of sight. Several research works on D-MaMIMO (or CF-MaMIMO) has been mentioned in the previous chapter, primarily focuses on the frequency bands below 6GHz, rather than explicitly on mmWave, and most commonly it has been assumed that there is a single antenna at each AP (that can be described as fully distributed massive MIMO: FD-MaMIMO). Hence, considering mmWave, this chapter, explores the advantages of using antenna directionality rather than single omni-directional antennas at each transmitting AP and the reduced wavelength at mmWave allows this within a physically small AP. We describe this as ***partially distributed massive MIMO (PD-MaMIMO)***. Hence, we show the performances of the distributed array system for different simulation scenarios for single user as follows: a) the number of APs increases with a constant number of elements in each, b) distributing a constant total number of elements over multiple arrays as APs in arrays with smaller numbers of elements, c) used different sizes of rectangular antenna arrays. We exploit these arrays to perform explicit 3D beamforming, directing a beam towards each user, and hence full pilot based channel estimation is not necessary.

This chapter is structured as follows: the next Section describes the system and channel model for pure LoS channel, while Section 3.3 describes the 3D beamforming approach, Section 3.4 includes the numerical results and discussion and finally Section 3.5 summarizes the chapter.

3.2 System and channel model

As mentioned in sec. 3.1, we consider a pure LoS model based on the standard 3GPP standard channel model for frequencies from 0.5 to 100 GHz [164] to observe the performance of distributed 3D massive MIMO in the mmWave frequency band for an outdoor environment. In this chapter, we assume LoS propagation only which follows the Friis inverse square formula, with no multipath. We will discuss about multipath in Chapter 6. We use this model to evaluate the performance of distributed antenna arrays in a 100×100 m^2 open square area where M APs, with $N_h \times N_v$ antenna elements each, serve K single antenna UE at 26

GHz. The 26 GHz covers the 3.25 GHz of spectrum between 24.25 GHz and 27.5 GHz. In Europe, 26 GHz is one of the pioneer 5G bands for mmWave communication [165]. The APs are arranged in two ways for the distributed system: firstly, the number of elements per AP is kept the same, while in the second approach, a constant total number of elements is split into smaller arrays over the coverage area. The positions of APs are at fixed around the edges of the square in different scenarios. In this arrangement, planar antenna arrays are considered to incorporate the 3D beamforming technology. Given the size of the simulation area we assume that a unobstructed LoS path is available between all APs and the UE, and the mmWave propagation follows the inverse square law, as mentioned before, given by the Friis equation. Again because of the short link lengths we neglect the attenuation due to the atmospheric and other losses. The signals on the direct paths from each AP are assumed to be phase controlled so as to combine coherently at the user. The received power, $P_{UE,m}$ from the m^{th} AP is calculated as

$$P_{UE,m} = P_{AP} G_{AP} G_{UE} \left(\frac{\lambda}{4\pi d_m} \right)^2 \tag{3.1}$$

where P_{AP} is the transmitting power. $L = \left(\frac{4\pi d_m}{\lambda}\right)^2$: that is, the path-loss depends on the distance d_m, between the AP and the UE and $\lambda = \frac{f_c}{c}$ is the wavelength, where f_c the carrier frequency and c the speed of light. G_{AP} is the transmitting antenna gain. Here, G_{UE} is the reeving antenna gain and for this particular case is 1 as the UE has single omnidirectional antenna. Therefore we can re-write the received signal power as

$$P_{UE,m} = \frac{P_{AP} G_{AP}}{L} \tag{3.2}$$

The noise power is given by

$$P_{noise} = kFTB \tag{3.3}$$

where $k = 1.3807 \times 10^{-23}$ is Boltzman constant, F is the noise figure, T the temperature and B is the bandwidth.

Hence, the signal-to noise ratio (SNR) is given by,

$$SNR_m = \frac{P_{UE,m}}{P_{noise}} \tag{3.4}$$

3.3 3D beamforming

Beamforming is one potential enabling technology for 5G, alongside mmWave, massive MIMO etc. Many current networks employ horizontal uniform linear beamforming arrays to generate a beam pattern in the azimuth plane: this is known as 2D beamforming (2DBF). In this chapter, planar antenna arrays are used, allowing beam steering in both azimuth and elevation: this is 3D beamforming (3DBF). According to [108], deploying 3DBF for 5G wireless network can enhance the signal strength by pointing the main lobe of the array beam to an intended user. The requirements of steerable beam and gain can be achieved by beamforming technology to compensate the attenuation and propagation loss in the mmWave communication and improve the spectral efficiency of the network [166][167].

3DBF is effective in increasing throughput of the system in the vertical plane by manipulating the downtilt angle where multiple users are served at different heights such as in high-rise buildings [168]. But in this chapter, for the simulation scenario, the difference between the heights of the APs and UE is small, as a result, the elevation angle does not vary significantly and for that the azimuth angle is more vital for the performance evaluation. Since the APs and UE are at different heights, the beamforming weights are applied at the APs to direct the signal towards the UE through the available LoS path. Here, we used an array with $N_h \times N_v$ elements with G_{AP} antenna gain: a function of the azimuth and the elevation angle between the AP and the UE. Considering the gain of each of the $N_h \times N_v$ elements, $G_{n_h,n_v}(\theta,\phi)$, the array factor, $AF(\theta,\phi)$ can be written as

$$AF(\theta,\phi) = \sum_{n_h=1}^{N_h}\sum_{n_v=1}^{N_v} w_{n_h,n_v}\sqrt{G_{n_h,n_v}(\theta,\phi)} \times e^{j[(n_h-1)kd_h\sin\theta\cos\phi+(n_v-1)kd_v\sin\theta\sin\phi]} \tag{3.5}$$

where $k = \frac{2\pi}{\lambda}$ is the propagation constant in free space, the antenna spacing is $\frac{\lambda}{2}$, and θ and ϕ are the azimuth and elevation angles respectively, d_h and d_v are the antenna element spacing in horizontal and vertical direction respectively, w_{n_h,n_v} is the weight of each element. The weights are defined so as to direct a beam from the array in the direction of the LoS to the UE. The weights can then be defined as

$$w_{n_h,n_v} = \exp\left(j\frac{2\pi}{\lambda}sin\theta(n_h d_h\cos\phi + n_v d_v\sin\phi)\right) \tag{3.6}$$

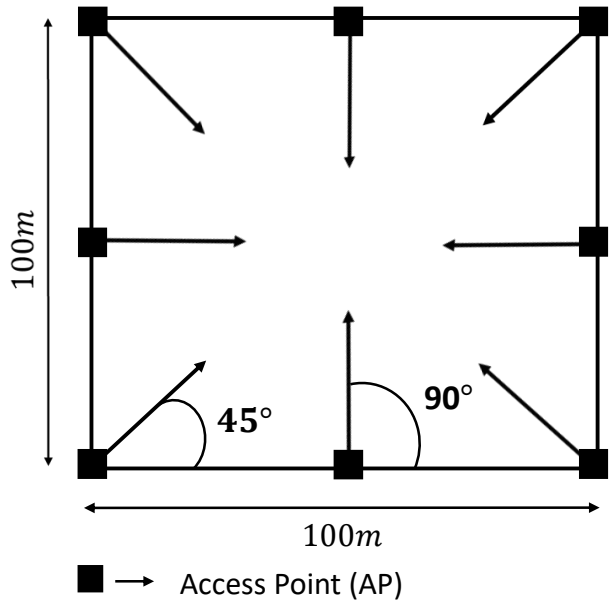

Fig. 3.1 Distribution of APs along the edges of the coverage area with fixed coordinates and their broadside directions for an instance of 8 APs

where n_h and n_v are the indices of the antenna element in the horizontal and vertical direction. Assuming 100% efficiency, the gain G_{AP} is given by

$$G_{AP} = \frac{|AF(\theta,\phi)|^2}{\int_{-\pi}^{\pi}\int_{-\pi/2}^{\pi/2}|AF(\theta',\phi')|^2 d\theta' d\phi'} \tag{3.7}$$

where θ' and ϕ' are the azimuth and the elevation angles of the signal intended for user K'.

3.4 Results and discussion

Simulation Scenario

Here, we demonstrate the system performance of distributed antenna arrays with that of a single antenna array in an outdoor square coverage area serving a mobile user equipped with a single antenna. For the simulation scenario, the APs are distributed into 1,2,4,8 and 16 arrays for different scenarios to study the scalability of APs in the overall performance. For 1,2 and 4 APs, the APs are placed at the corners of the square and their the broadsides are at 45° to the walls, directed towards the centre of the square and for 8 and 16 some of the APs are placed on the boundary of the square with 90° broadsides facing the centre. Fig.

3.1 is the schematic diagram of the AP distribution and their corresponding broadside for an instance of 8 APs. In this figure, it is shown that the APs positioned at the corners are at 45° broadside to the edge of the square and the APs installed in the middle of the line are at 90°. This is appropriate because the gain of a planar array drops with the cosine of the angle from broadside, and this configuration means that if the AP is at the corner of the square, it can cover with angle from broadside no greater than 45° whereas if the AP is at the centre of the boundary, the deviation is up to 90°. The heights of APs and UE are assumed to be 6 metres and 1.5 metres respectively. The height of the AP is chosen based on the height of a street light in a residential area in the UK, while for the UE; it is based on the average height of a person. The total transmit power is constant in every scenarios and that is 33dBm over the bandwidth of 1.5 GHz, and the receiver has a noise figure of 10dB. The simulation parameters are given in Table3.1.

Table 3.1 Simulation parameters

Parameter	**Setting**
Coverage area	$100 \times 100\ m^2$
Power per UE, P_{UE}	33dBm
Carrier frequency, f_c	26 GHz
Bandwidth	1.5 GHz
Noise figure	10 dB
Temperature	290 K
Number of UE	1
Receiving antenna gain, G_{UE}	1
Antenna efficiency	100%

Grid Points and Pre-calculation

In order to capture the SNR distribution of the square coverage area for a particular set of AP arrangements, we produce contour plots. Contour plots are generally used to depicts a 3D surface on a 2D X,Y plane. It represents two variables as X and Y and a response variable Z as contours. To model the contour plots, the whole region is required to be divided into equal grids along X and Y axis such as, the X and Y variables are the co-ordinates of the points inside the coverage area. Therefore, the entire service area is divided into grids and each grid is set to $1 \times 1\ m^2$. To provide finer resolution the split is made to 99×99 along both the axis. For the $100 \times 100\ m^2$ space, these grids induce 9801 points for the UE to be placed and their

SNR values are on the Z scales. Additionally, using these grid points we are able to make individual data sets for the antenna gains and the steering vectors for different types of AP placements. As a result, it significantly reduces the computation time. We assume the test user is positioned at different pints on this grids and capture the overall SNR profile for the entire service area. To obtain the AP gain MATLAB package for uniform rectangular array is used.

Simulation Results

In this section, we present the contour plots and numerical results from the simulation, demonstrating the distributed antenna arrays for mmWave communication in the 3D LoS environment. We show the contour plots for received SNR at each grid point at which the mobile UE is placed for different distributions of the APs, and plot the cumulative distribution function (CDF) graph to indicate the changes caused by these distributions. We used contour plots to show the different contour level to determine the different picks of the SNR values at different regions of the service area. It is seen that the signals combine coherently in the direct path as the signal amplitudes are summed at the UE from each AP and are then squared to obtain the LoS power. Then the total LoS powers give total received power at the user and the ratio of the total received power to the thermal noise provides the SNR values to plot the overall performance. In this context, we present three sets of results. For the first set of results, the number of APs are increased to incorporate the distributed system with a constant number of antenna elements in each site ensuring same beam-width per AP for all the scenarios. Furthermore, for the second set of results, the advantage of distributed antenna arrays over a single or centralized is observed by distributing a constant total number of antenna elements between smaller antenna arrays compared to centralising them in one array. We named this approach ***partially distributed massive MIMO***. In this approach, the processing power within the infrastructure is identical for all the cases. Finally, we show the results for different shapes of the APs. This set of results does not make any remarkable difference but for the multi-user case it makes a significant deviation, and will be shown in chapter 4.

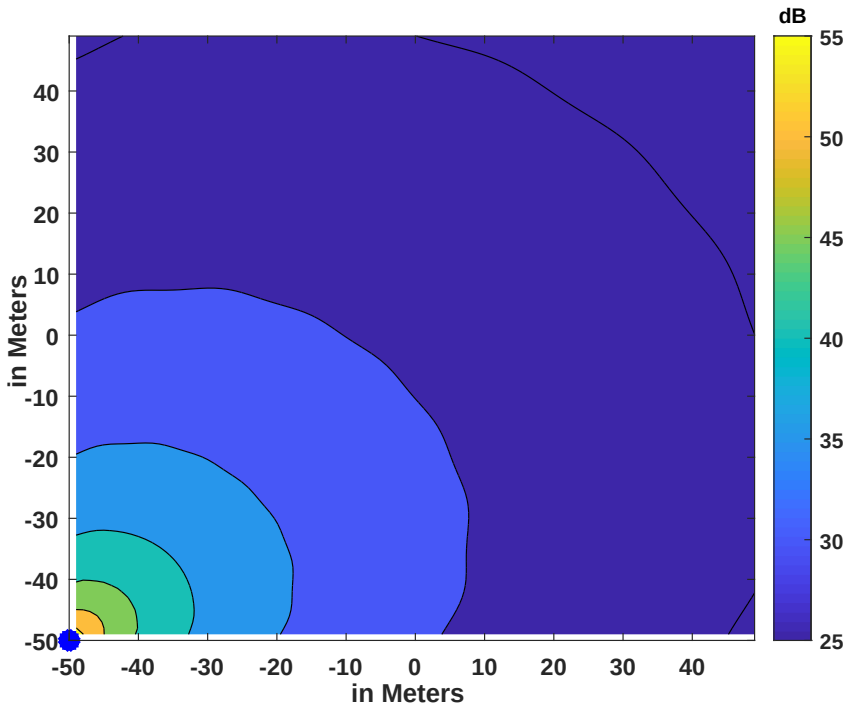

Fig. 3.2 SNR distribution for single UE from 1AP (marked in blue) in a square coverage area

Figure 3.2 - 3.9 show the contour plots and the CDFs of the SNR distribution of a single UE for different AP distributions with constant number of antenna elements in each AP. The APs are distributed in the order of 1,2,4,8 and 16. Each AP contains 100 elements using an 10×10 uniform planar array (UPA) configuration for all the distributions. The APs are placed at the corners or the middle of the edges and to ensure the maximum coverage.

Figure 3.2 represents the contour plot of the SNR of a single UE in different grid points of the coverage area while served by a single AP. In this figure, the AP is placed at the left bottom corner of the square area and pointing at the centre with 45° broadside. It is observed that the areas in the immediate vicinity of the AP are illuminated because of the high SNR but the opposite far end and the surroundings areas experience poor service due to increased path-loss and short wavelength of mmWave. As the UE is positioned away from the AP the SNR values begin to reduce and within 20 m it falls around 14 dB. If the distance between the mobile UE and the AP further increases diagonally to the opposite corner, the SNR drops drastically almost 29dB. We assume the coverage area to be a square, placing the AP at any corner or a particular point on the borders will exhibit similar performance.

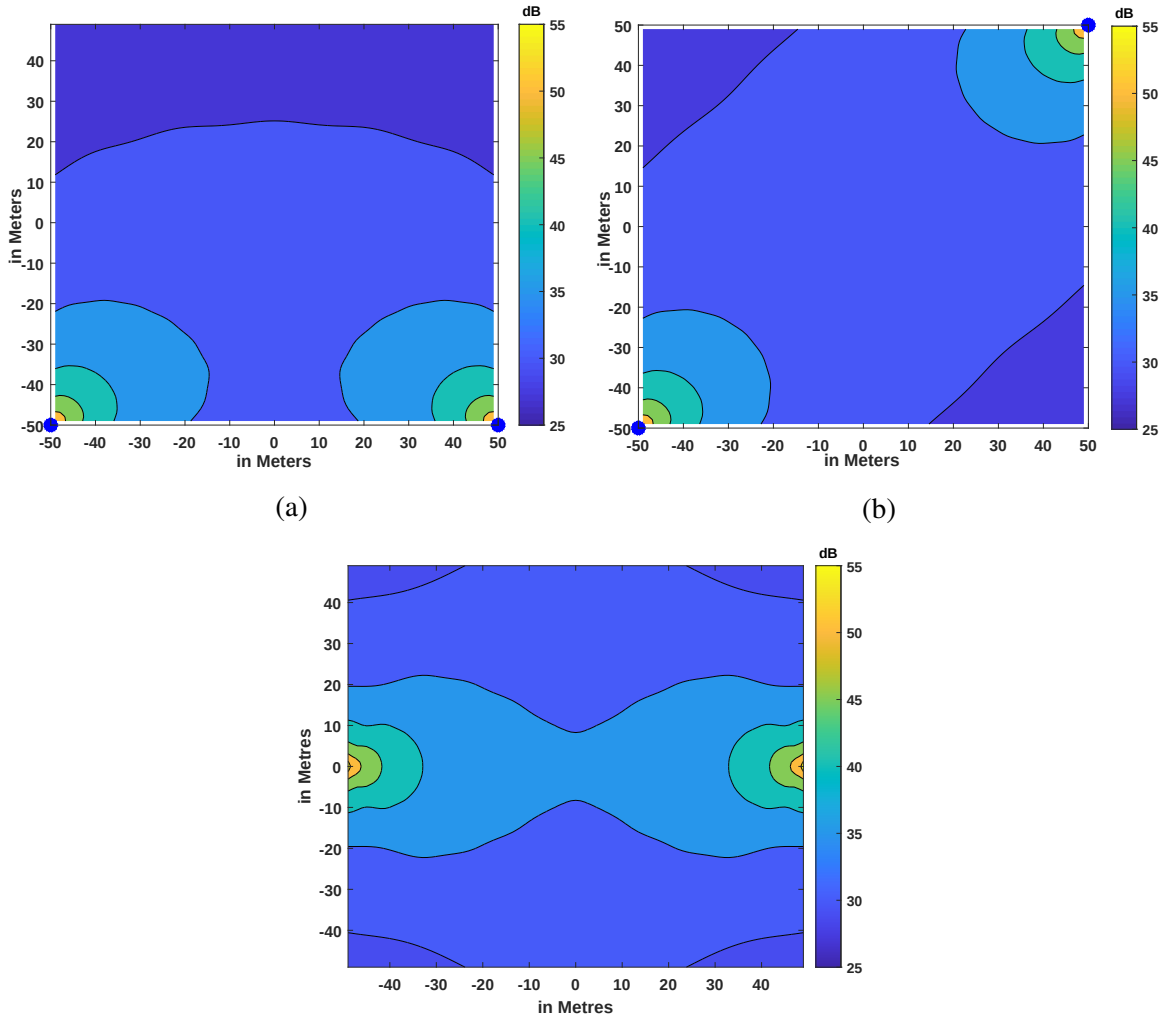

Fig. 3.3 Contour plots of different arrangements of 2APs around the edges of the square coverage area

Figure 3.3 shows the contour plots of SNR distributions of a single UE from 2 APs arranged in different patterns to explore the best performance using these APs. We organised these two APs in three sets of locations. In Fig. 3.3 (a), the APs are positioned at two bottom corners of the service area and their broadsides are at 45° towards the centre. It is seen that the SNR values at the areas near the APs are extremely high. On the other hand, the SNR distribution at the opposite end is quite low. It can be said that $\frac{1}{3}$ of the service area is affected by low SNR in this arrangement and the SNR reduces around 6 to 18dB from near AP positions to the far end. In Fig. 3.3 (b), we have moved the APs at two opposite corners of the square keeping the same broadside directions towards the centre as before. Here, it is

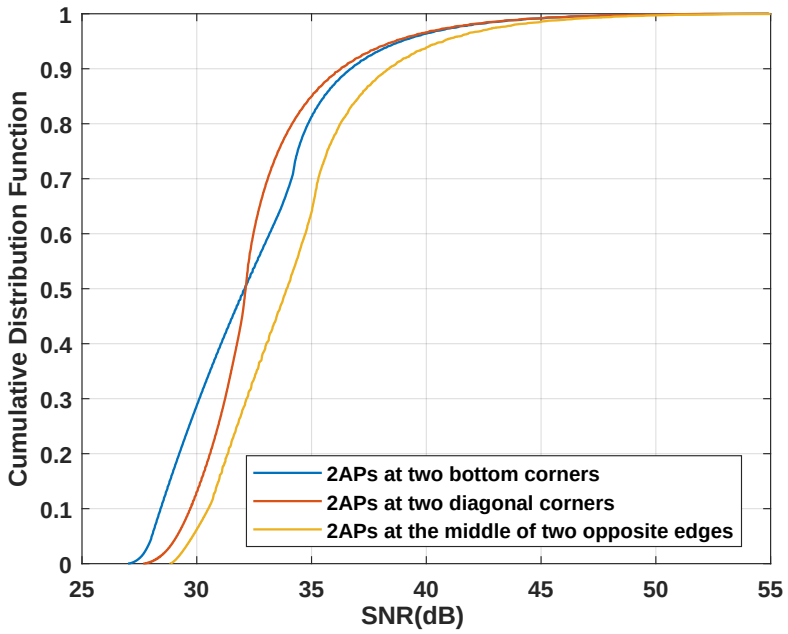

Fig. 3.4 The CDF of different 2APs arrangements in a square coverage area

seen that the areas suffer from low SNR are reduced and the SNR values are also higher than the previous case. As we have seen previously in all arrangements that the SNR is very high near the APs and beyond 20m the SNR decrease to a steady points through a wide range of space. Consequently, the areas around other two opposite corner where there are no APs, experience drops about 3dB. Nonetheless, it is not as severe as in previous arrangement. In Fig. 3.3 (c), we placed the APs at the middle of two opposite edges of the coverage area and the broadsides are at 90° inward. The distance between two APs is shorter compared to the previous arrangement and because of this reason the SNR improves in the middle section. However, the SNR around the four corners reduces by about 6dB from the centre point. Fig. 3.4 shows the CDF of these three arrangements and it is seen that at 5th percentile, the differences between the SNR of these three configurations are around 1dB and the AP arrangement in Fig. 3.3 (c) is better than the other two.

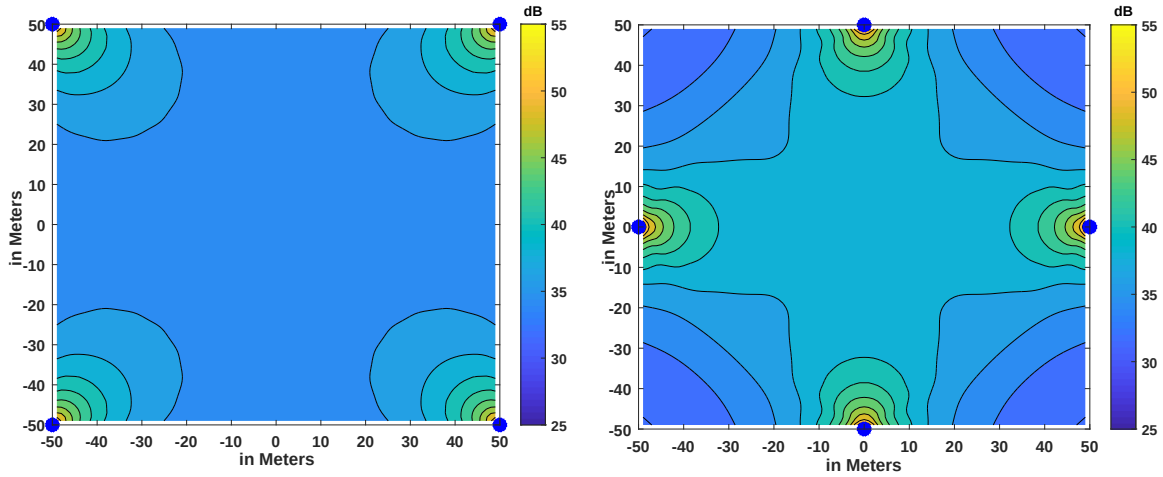

(a) (b)

Fig. 3.5 Contour plots of different arrangements of 4APs around the edges of the square coverage area

Figure 3.5 shows the contour plots of SNR distributions of a single UE from 4 APs arranged in different patterns. In set 1 (Fig. 3.5 a), the APs are positioned at the four corners of the service area with the broadside at 45° and in set 2 (Fig. 3.5 b), the APs are at the middle of the four edges of the square area with the broadside at 90°. Fig. 3.5 (a) suggests that using 4 APs at four corners provides a uniform service for the mobile UE without any prominent drop and the overall performance is increased. Whereas for Fig. 3.5 (b), due to the shorter distance between the opposite placed APs the middle part of the square experiences higher SNR but the corners exhibit a notable drop in SNR around of 6dB.

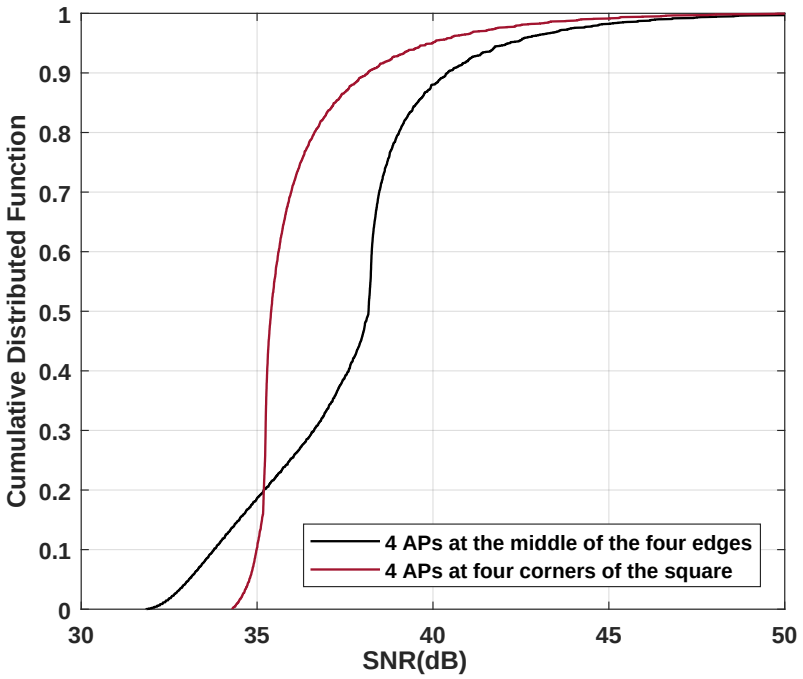

Fig. 3.6 The CDF of different 4APs arrangements in a square coverage area

Fig. 3.6 shows the CDF of these arrangements and it is observed that at 5th percentile the SNR curve of set 1 is higher that the SNR curve of set 2 by 2dB. But at 50th percentile the SNR of set 2 is improved than the SNR of set 1 by 3dB. This is due to the short distances between the APs in set 2 give rise to the SNR in the centre areas whereas the the corners suffer from poor coverage as we seen in Fig. 3.5 (b).

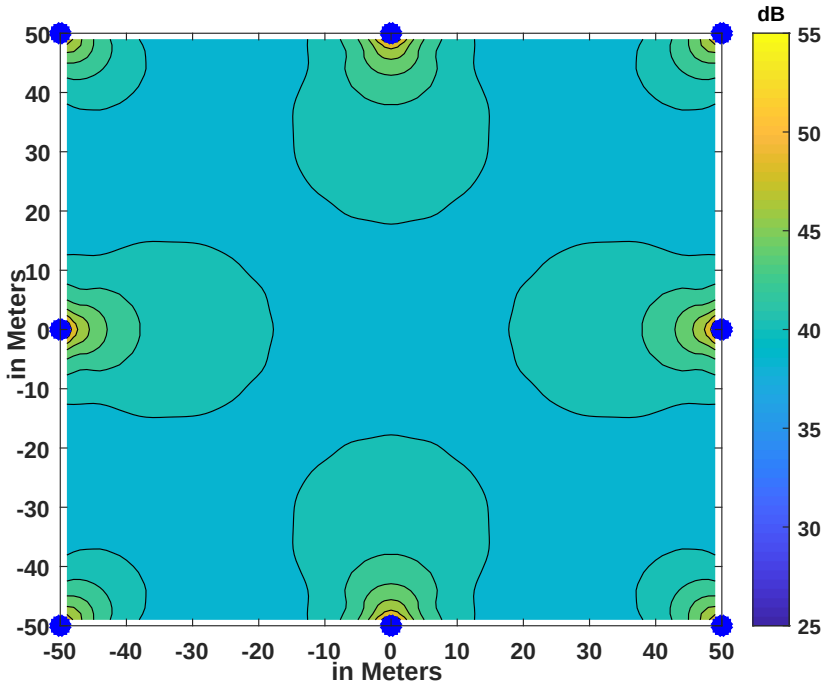

Fig. 3.7 Contour plots of the SNR distribution of 8APs around the edges of the square coverage area

Figure 3.7 illustrates the SNR performance of a UE placed at the grid points of the service area where 8 APs are serving simultaneously. Here, the APs are equally distanced from each other. Firstly, four APs are set at the corners and then the remained four are placed at the middle of two APs each side. The broadside arrangement is as shown in Fig 3.1. The SNR improves significantly by doubling the APs and the coverage is fairly uniform between the APs. The SNR rises to maximum as the UE approaches close to any AP.

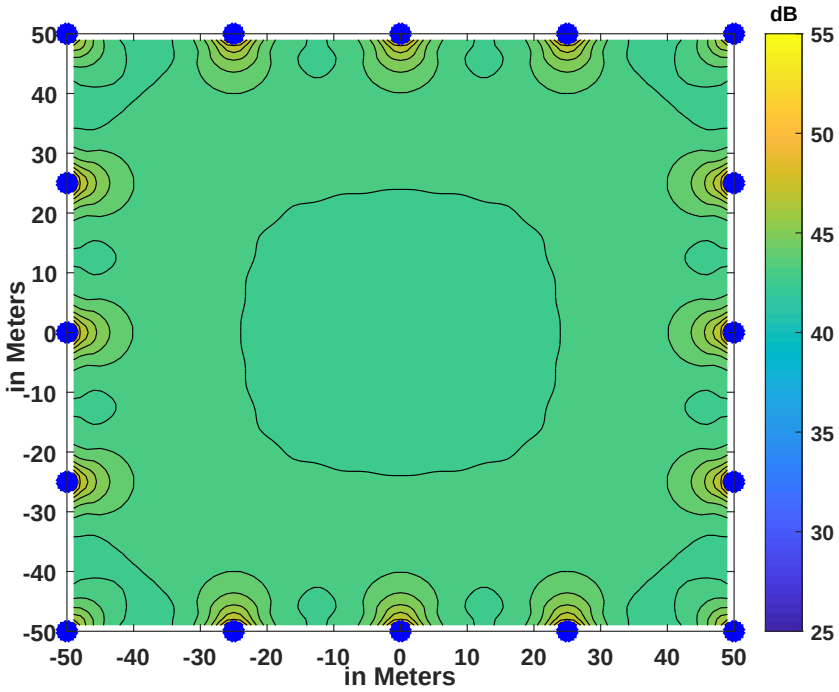

Fig. 3.8 Contour plots of the SNR distribution of 16APs around the edges of the square coverage area

Fig. 3.8 is the contour plot of the SNR experienced by the single UE from 16 APs each with 10×10 antennas. Similarly, in this configuration the APs are uniformly distributed over the edges of the service area. The performance continues to improve with increasing number of APs along with uniform coverage. However, it can also be noticed that the coverage area is extremely dense with large number APs which can increase the installation cost and processing power.

Finally, Fig. 3.9 shows the CDF of the SNR distribution for the different arrangements of APs shown in previous contour plots. It is observed that at 5th percentile, apart from 4 APs, for every doubling of the number of APs the SNR curve improves by around 4dB. From 2 APs to 4 APs the rise in SNR is almost 6dB. It is seen from the contour plots that using 4 APs instead of 2 APs in service improves the SNR significantly and the coverage becomes uniform.

Figure 3.10 presents the contour plots and the CDFs of the SNR distribution of a single UE for different AP distributions where a constant total number of antenna elements are distributed among a large number of APs. We maintained the same AP distributions as in the previous cases. The total elements are distributed into 1,2,4,8 and 16 APs. Here, we assume the total number of antenna elements is 1600.

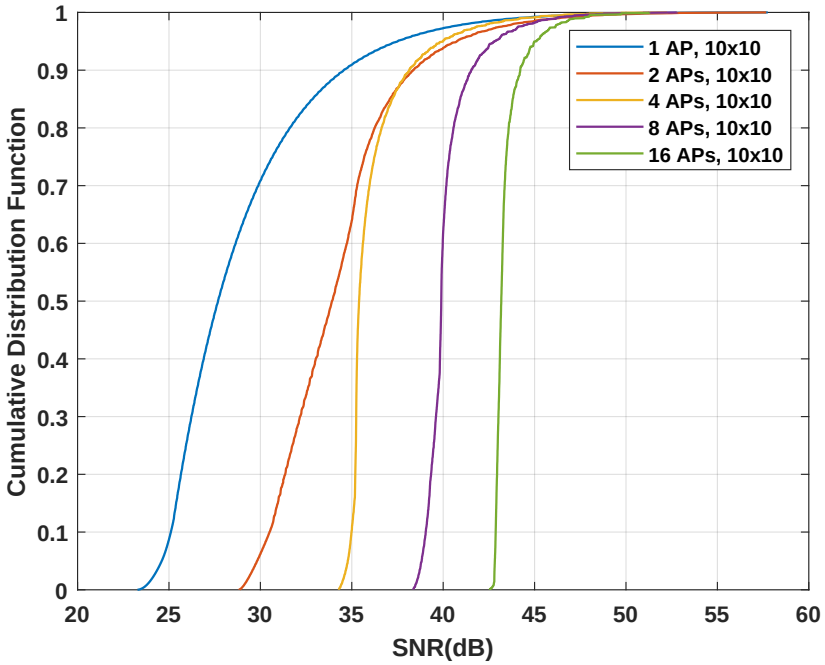

Fig. 3.9 The CDF of the SNR distribution for different number of APs with a constant number of antenna elements in each AP

Figure 3.10a shows the contour plot of the SNR distribution of a mobile UE served by a single AP. The array consists of 40×40 elements and placed at the bottom left of the area. As we have seen before for a single AP case the SNR is high near the AP but at the far corner the coverage is very poor. The drop is around 20dB. In Fig. 3.10b, the contour plot depicts the SNR distribution from two APs placed at the middle of two opposite edges. We used this positions because it is seen from Fig. 3.3 that the SNR distribution is best for this configuration. These two arrays have 28×28 elements each. Here, the total number of elements is 1568 which is less then 1600 because we are using square arrays with identical numbers of elements in horizontal and vertical directions. The SNR and the coverage improve with two APs and the drop is not as significant as in the 1 AP case and at the corners it is about 7dB from the centre.

Figure 3.10c shows the contour plot of the SNR where four APs are active. The 4 APs are located at the four corners of the service area and each contains 20×20 elements. It is noticed that the SNR significantly improves from using 2 APs by 4dB and the coverage is quite uniform throughout the service area. The contour plot of SNR with 8 APs is shown in Fig. 3.10d. The APs are distributed at equal distance from each other around the boundary of the square as shown before and each of the APs consists of 14×14 elements. Again, in this

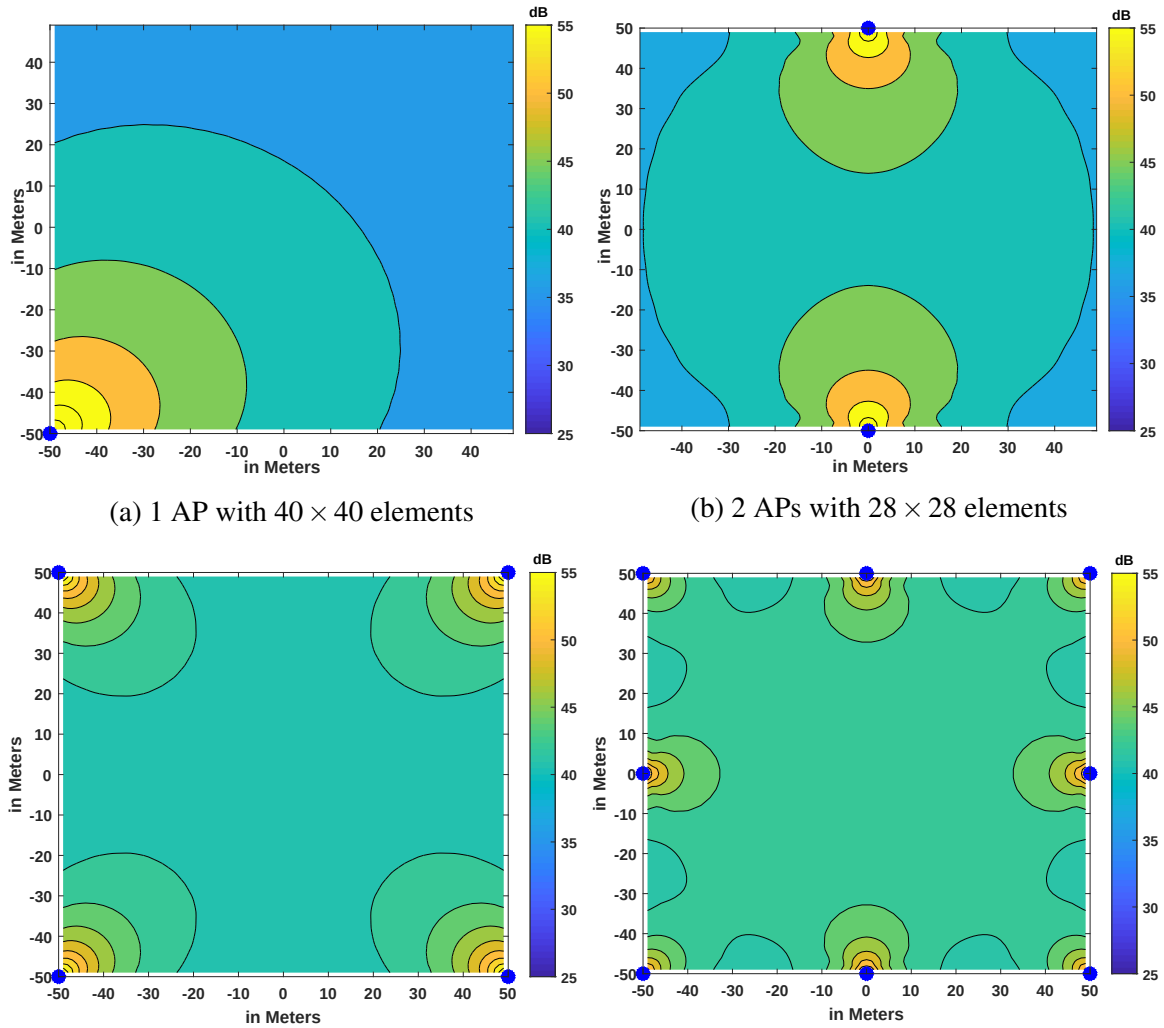

(a) 1 AP with 40×40 elements

(b) 2 APs with 28×28 elements

(c) 4 AP with 20×20 elements

(d) 8 APs with 14×14 elements

Fig. 3.10 Contour plot of received SNR for a single UE from various numbers of distributed APs with different elements

case the total number of elements is 1568 due to the use of square array. The locations and broadsides are maintained as shown in Fig. 3.1. The SNR improves by 1dB and the coverage is also consistent throughout the whole service area.

As we have observed before 3.8 shows the SNR profile of the single UE where 16 APs are operating. Each AP is equipped with 10×10 elements and equally spaced from each other. The SNR improves further by 1dB for the coverage area without any remarkable drop. However, there is a "squircle" shape which appears in the middle where the SNR falls approximately 1dB which is negligible compare to the overall performance.

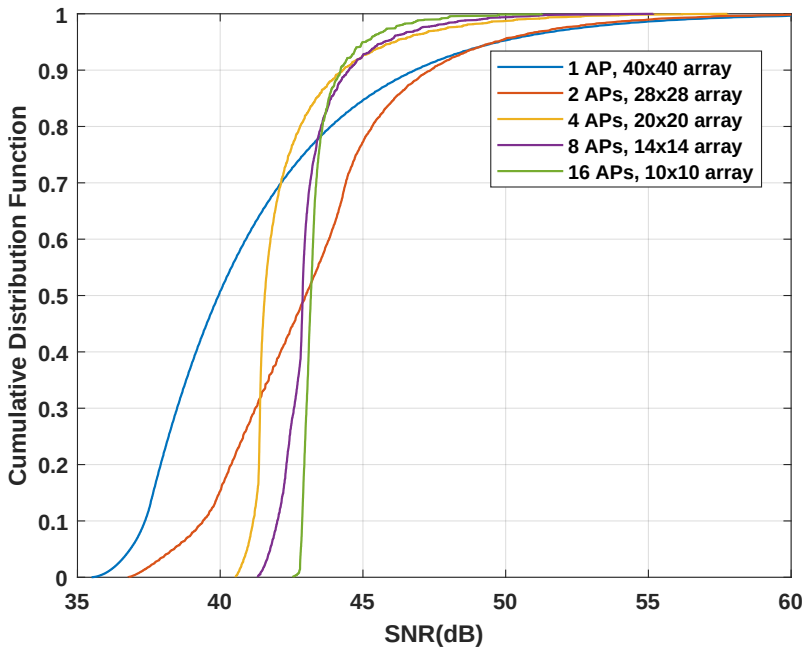

Fig. 3.11 The CDF of the SNR distribution for different number of APs with a total constant number of antenna elements divided into APs

The CDFs of the SNR for different distributions of APs are illustrated in Fig. 3.11. At the 5th percentile, from the 1 AP scenario to 2 APs, the SNR increases by almost 1.5dB. The contour plot of the 4 AP case has shown better and uniform coverage than other arrangements. Hence, the significant improvement in SNR performance is observed using 4 APs, of around 3 dB over the 2 AP case. Furthermore, for the 8 and 16 AP cases the increase in SNR is about 1 dB respectively.

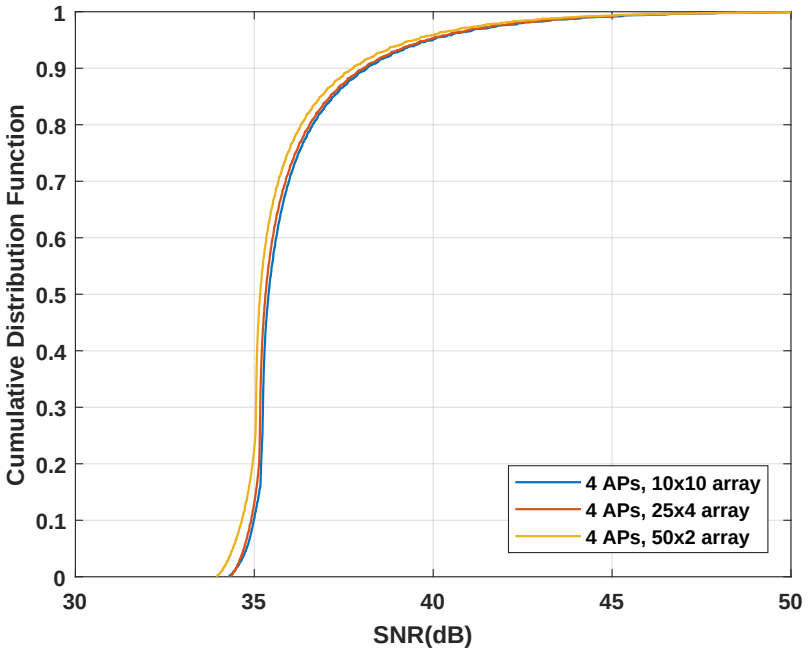

Fig. 3.12 The CDF of the SNR comparing 4APs with different sizes

Finally, 3.12 shows the CDF plot for different configurations of APs. The configurations of 4 APs at the corners are as follows: (a) each equipped with 10×10 antenna elements, (b) each AP has 25×4 elements and (c) the horizontal elements are 50 and vertical elements are 2 (i.e. 50×2). The contour plots are similar to Fig. 3.5 (a). When the horizontal elements are increased, the horizontal beam-width becomes narrower. In the scenarios considered so far, the heights of the APs and UEs are kept fixed, and as a result the elevation does not vary notably. Whereas the azimuth angle, due to large coverage area and UE placement, deviates significantly. Consequently, the beam-width for the azimuth direction plays a pivotal role. But from the contour plots it is seen that the SNR distribution for the whole coverage area is nearly identical for the studied antenna configurations and hence the CDF plots (Fig.3.12) also do not show any remarkable change. For the single UE case, the azimuth separation is indifferent. On the other hand, the azimuth separation makes a significant impact in multi-user cases, as will be seen in the following chapters.

3.5 Summary

In this chapter, we have shown the performance of a distributed massive MIMO system with planar arrays at access points in a LoS scenario, with a view in particular to millimetre-wave

transmission. We have studied three cases that draw the benefits of partially distributed antenna array system for only a single user in an outdoor square area. We applied a 3D beamforming technique to steer the beam towards the intended UE. It is observed that, if we facilitate the coverage area with distributed APs rather than concentrating all the antenna elements into one centralised array in the centre of a cell, the performance will get better with increasing number of APs. This is due to the significant gains that are available by distributing antenna elements over a number of smaller arrays. We have demonstrated the difference in the outcome with different array arrangements. Firstly, we distributed the APs with a constant number of elements and it is seen that if we continue to increase the number of APs in this manner then the processing power will also increase along with the installation cost. Secondly, we choose to split a constant total number of antenna elements between APs and observed that at certain point of distribution the further distributions make insignificant improvement in the SNR values. For this particular set of coverage area that is a square outdoor, we can conclude that placing 4 APs at the four corners with 45° broadside facing the centre, provide optimal quality of service for the UE. Finally, we have shown different configurations of APs maintaining the 4 AP arrangement and for a single UE the different shapes of the APs are less significant than with multi-users.

Chapter 4

Multi-user D-MaMIMO System using Zero-forcing Pre-coding

4.1 Introduction

In Chapter 3, we have considered a distributed 3D beamforming (3DBF) system operating at mmWave using multi-antenna access points (AP): specifically APs using planar arrays for the single user case. For a single user equipment (UE) case, the system is much simpler as these is no inter user interference. However, multi-user massive multiple-input-multiple-output (MU-MaMIMO) increases the complexity of the system with rising interference between multiple users besides the challenges due the unusual propagation characteristics while operating in mmWave band. As a result, in the multi-user environment, it is quite obvious that the performance can be affected by this induced inter-user interference [169]. Nonetheless, MU-MaMIMO draws an enormous amount of interest for 5G and beyond to achieve the high data rate and energy efficiency for ultra-dense networks (UDNs), mentioned in chapter 2. One of the purposes of this chapter is to focus on eliminating this interference from multiple users taking into account how readily we can separate the users without degrading the performance. The beamforming (BF) and zero-forcing (ZF) are two linear pre-coding techniques for the transmission of data and suppressing the multi-user interference in MU-MaMIMO systems [170][171]. However, both [105] and [106] addressed the additional interference due to energy leakage using transmit BF and proposed a solution through optimization to maximize the signal power and minimize the interference. According to [147], ZFBF can be utilized without any self-interference and it performs better than the conjugate BF technique for the high spectral and power efficient system. In conjugate BF, the pre-coding matrix is obtained by the conjugate of the estimated channel matrix whereas in ZF pre-coding vectors are the

pseudo-inverse of the estimated channel matrix [170]. Moreover, the ZF pre-coding strictly operates on the basis on perfect knowledge of the CSI [143]. Therefore, it is observed that for D-MIMO system using ZF, both CSI and phase synchronization are important factors. Any error occurring from these two factors at the transmitting end can cause power leakage and performance degradation for DL transmission [172]. As mentioned in Chapter 2, several approaches are adapted to address the CSI issue and the authors in [65] assumed perfect CSI knowledge.

It is clearly seen that applying only the BF at the transmitter may not be enough to eliminate the inter-user interference. In this chapter we have depicted that with the simulation results. We propose a partially distributed ZF algorithm at the transmitting end where the APs are are performing beamforming and show that using this ZF approach the performance is significantly better than using only BF approach for multi-user. The ZF approach is applied such that simple BF is applied at each access point (AP) with centralized ZF applied at the CPU and here we assume single-antenna users for the sake of simplicity. We assumed that the CSI is not needed. Moreover, the ZF scheme is investigated in detail, especially for two closely spaced users. We also look into a system that includes dense users for different arrangements of APs and we determine how many UEs can be effectively served using ZF approach. Here, primarily we consider a two-user case for presenting a performance analysis and then generalise to a larger number of users in the system. Firstly, for the two UE cases, we obtain the SINR values received by an UE positioned at different grid points (we have used the same grid system as mentioned in chapter 3) inside the coverage area with the presence of another UE at a fixed position, exploiting both techniques. Furthermore, the correlation between the steering vectors of these two UEs are shown on contour plots. For a larger number of UEs, we show the throughput per UE for the system. In addition, we introduce phase errors at the transmitter end to investigate the issue of stability in mmWave oscillators and exhibit the results to show the degree of degradation in the SNR performance in the multi-user system. To obtain the numerical results we make use of the open square scenario described in chapter 3, in which a LoS path is dominant.

This chapter is structured as follows: the next Section 4.2 describes the system and channel model for the pure LoS channel, while Section 4.3 describes the the partially distributed ZF algorithm and we analyze the performance of the ZF algorithm, considering the effect of two closely-spaced users on the algorithm performance. Section 4.4 includes the numerical results and discussion and finally Section 4.5 summarizes the chapter.

4.2 Multi-user Massive MIMO System Channel Model

In this chapter, the simulation scenario is maintained as we described in Chapter 3 where the M APs are distributed on the edges of an open square, assumed to be $100m \times 100m$. The height of the APs is taken as 6 metres . The APs are directional multi-antenna arrays, serving omnidirectional UEs. The UEs are distributed within the square, with height assumed to be 1.5 metres. Previously, we have seen that, for an open square outdoor environment, using 4 APs at the four corners provides optimal performance and uniform coverage. So,we prefer to keep the number of APs to 4 for the simulation scenarios but we take different number of antenna elements and their configurations into account to show the best combination. Figure 4.1 shows the simulation scenario where we assume 4 APs are placed at the corners of the square, pointing 45° to the walls as the broadside direction towards the centre of the square. Here, K number of single-antenna UEs are served by M APs, which in turn are connected to a single CPU serving the entire network. Each AP is equipped with N_T antennas, arranged as an array, in this case a planar array. Each AP steers a beam in the direction of each user: the steering vector for the beam towards k^{th} user from m^{th} AP is defined as $\mathbf{v}_{mk}$. The channel from the N_T antenna elements to the k^{th} UE is defined by the vector $\mathbf{h}_{mk}$. The K steering vectors at APm are combined to form a $N_T \times K$ matrix:

$$\mathbf{V}_m = [\mathbf{v}_{m1} \dots \mathbf{v}_{mk} \dots \mathbf{v}_{mK}] \tag{4.1}$$

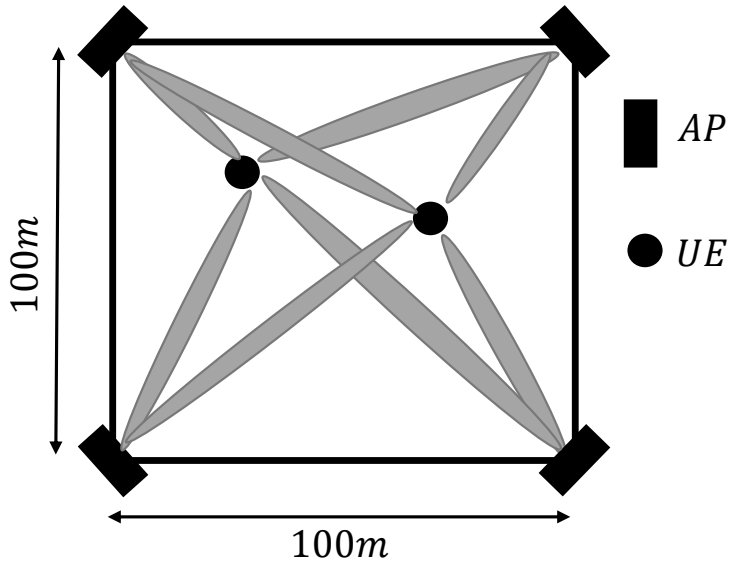

Fig. 4.1 Simulation scenario

For a downlink MU-MaMIMO system, the received signal at the i^{th} UE is given by

$$y_i = \sum_{m=1}^{M} \mathbf{h}_{im}\mathbf{x}_m + z_i \tag{4.2}$$

where $\mathbf{x}_m$ is the transmitted signal vector from the m^{th} AP, M is the number of access points, z_i is the noise at the i^{th} UE. For the channel matrix between the m^{th} AP and the i^{th} UE we can calculate the distance d_{im} and angle from broadside θ_{im} of the UE from the APm array. The channel vector $\mathbf{h}_{im}$ is then given by the Friis equation:

$$\mathbf{h}_{im} = \exp(-i\omega_{im})\sqrt{\beta_{im}}\boldsymbol{\psi}_T^H(\theta_{im}) = \exp(-i\omega_{im})\sqrt{G_T(\theta_{im})\left(\frac{\lambda}{4\pi d_{im}}\right)^2}\boldsymbol{\psi}_T^H(\theta_{im}) \tag{4.3}$$

This channel matrix is formed between the inputs to each transmit antennas and the output of the antennas at the receiver. Where β_{im} is the path power gain, including the gain of the antenna array that is $G_T(\theta_{im})$ in the direction θ_{im}. Furthermore, $\boldsymbol{\psi}_T^H(\theta_{im})$ is the steering vector of the transmit array in the direction θ_{im}, which is the direction (relative to broadside) of the i^{th} UE from the m^{th} AP. We make the normalizing assumption that $\|\boldsymbol{\psi}_T^H(\theta_{im})\|^2 = 1$. With the approximation of normalization of the steering vectors, the antenna array gain should be equal to the total number of antennas but as we have mentioned before that for planar antenna array, the gain reduces with the cosine of the angle from broadside. Hence, we include the antenna array gain into the channel matrix, $\mathbf{h}_{im}$. λ is the wavelength and ω_{im} is the phase shift corresponding to this path: since it depends on the exact path length relative to the wavelength (which is small) we will treat it as a uniform random variable between $\pm\pi$. Then the transmitted signal vector is in turn given by:

$$\mathbf{x}_m = \sum_{k=1}^{K} \mathbf{v}_{mk}s_{mk} \tag{4.4}$$

where $\mathbf{v}_{mk}$ is the pre-coding vector applied at the APm to the signal intended for the UEk, and s_{mk} is that signal at the APm intended for the UEk. Again we assume that $\|\mathbf{v}_{mk}\|^2 = 1$, which implies that the total transmitted power from m^{th} AP is $\overline{\|\mathbf{x}_m\|^2} = \sum_{k=1}^{K}\overline{|s_{mk}|^2} = \overline{\|\mathbf{s}_m\|^2}$ and the total power over all the APs is $\sum_{m=1}^{M}\overline{\|\mathbf{s}_m\|^2} = \overline{\|\mathbf{s}\|^2}$ ($\mathbf{s}_m$ and $\mathbf{s}$ is defined in 4.8).

Then the received signal becomes:

$$y_i = \sum_{m=1}^{M} \mathbf{h}_{im} \sum_{k=1}^{K} \mathbf{v}_{mk} s_{mk} + z_i = \sum_{m=1}^{M} \sum_{k=1}^{K} \exp(-i\omega_{im}) \sqrt{\beta_{im}} \boldsymbol{\psi}_T^H(\theta_{im}) \mathbf{v}_{mk} s_{mk} + z_i \tag{4.5}$$

We suppose that the pre-coding vector $\mathbf{v}_{mk}$ steers a beam in the direction of UEk, i.e. $\mathbf{v}_{mk} = \exp(i\omega_{mk}) \boldsymbol{\psi}_T(\theta_{mk})$. We write the normalized correlation between the steering vectors from APm, UEi and UEk, $\boldsymbol{\psi}_T^H(\theta_{im}) \boldsymbol{\psi}_T(\theta_{mk})$ as $\rho_{ik,m}$, with $\rho_{ii,m} = 1$. Then:

$$y_i = \sum_{m=1}^{M} \sum_{k=1}^{K} \exp(i(\omega_{mk} - \omega_{im})) \sqrt{\beta_{im}} \rho_{ik,m} s_{mk} + z_i \tag{4.6}$$

We may write this as:

$$\mathbf{y} = \sum_{m=1}^{M} \grave{\mathbf{H}}_m \mathbf{s}_m + \mathbf{z} = \grave{\mathbf{H}} \mathbf{s} + \mathbf{z} \tag{4.7}$$

where

$$\begin{aligned} [\mathbf{H}_m]_{ik} &= \exp(i(\omega_{mk} - \omega_{im})) \sqrt{\beta_{im}} \rho_{ik,m} \\ \mathbf{s}_m &= \begin{bmatrix} s_{1m} \dots s_{mk} \dots s_{mK} \end{bmatrix}^T \\ \grave{\mathbf{H}}_m &= \begin{bmatrix} \mathbf{h}_{1m} \dots \mathbf{h}_{mk} \dots \mathbf{h}_{mK} \end{bmatrix} \textit{ and} \\ \mathbf{s} &= \begin{bmatrix} \mathbf{s_1} \\ \vdots \\ \mathbf{s}_M \end{bmatrix} \end{aligned} \tag{4.8}$$

4.3 Beamforming for the Multi-user Case

Again we consider a downlink multi-user environment where M APs are communicating with K users [91]. The received signal at the intended i^{th} UE from the m^{th} AP is given by

$$y_i = \sum_{m=1}^{M} \mathbf{H}_{im} \mathbf{v}_{im} s_{im} + \sum_{m=1}^{M} \sum_{k=1, k \neq i}^{K} \mathbf{H}_{mk} \mathbf{v}_{mk} s_{mk} + z_i \tag{4.9}$$

where $\mathbf{H}_{im}$ is the channel matrix between the i^{th} UE from the m^{th} AP. Here, $\mathbf{v}_{im}$ is the BF vectors and s_{im} denotes the transmitted data intended for user i. The second term is the interference caused by the multi-user nature of the system and z_i is the noise at i^{th} UE. Now, let us assume for the i^{th} user s_i can be estimated from y_i in 4.9. i.e.,

$$\hat{s}_i \triangleq \frac{\mathbf{v}_{im}^* \mathbf{H}_{im}^* y_i}{\|\mathbf{H}_{im}\mathbf{v}_{im}\|^2} \tag{4.10}$$

Then:

$$\hat{s}_i = s_{im} + \frac{\mathbf{v}_{im}^* \mathbf{H}_{im}^* \sum_{m=1}^{M} \sum_{k=1,k\neq i}^{K} \mathbf{H}_{mk}\mathbf{v}_{mk}s_{mk}}{\|\mathbf{H}_{im}\mathbf{v}_{im}\|^2} + \frac{\mathbf{v}_{im}^* \mathbf{H}_{im}^* z_i}{\|\mathbf{H}_{im}\mathbf{v}_{im}\|^2} \tag{4.11}$$

For the i^{th} user the output signal-to-interference-noise ratio (SINR) is given by

$$SINR_i = \frac{\|\mathbf{H}_{im}\mathbf{v}_{im}\|^2}{\sigma_i^2 + \frac{\sum_{m=1}^{M}\sum_{k=1,k\neq i}^{K}\|\mathbf{v}_{im}^*\mathbf{H}_{im}^*\mathbf{H}_{mk}\mathbf{v}_{mk}\|^2}{\|\mathbf{H}_{im}\mathbf{v}_{im}\|^2}} \tag{4.12}$$

4.4 ZF Pre-coding for Multi-user Case

We first consider the CPU pre-coding matrix required in order to separate the signals to each user. We may stack the M length-K vectors of fronthaul signals from the CPU, and hence define a $K \times MK$ composite channel matrix between this vector and the received signal vector across the UEs:

$$\mathbf{H} = \left[\mathbf{H}_1\mathbf{V}_1 \ldots \mathbf{H}_m\mathbf{V}_m \ldots \mathbf{H}_M\mathbf{V}_M\right] \tag{4.13}$$

The CPU pre-coding matrix is then the pseudo-inverse of this matrix:

$$\overline{\mathbf{V}} = \mathbf{H}^H(\mathbf{H}\mathbf{H}^H)^{-1}\mathbf{A} \tag{4.14}$$

$\mathbf{A}$ is a $K \times K$ diagonal matrix chosen to ensure that the norm of the k^{th} column of the pre-coder, $\|[\overline{\mathbf{V}}_k\|^2 = \sum_{m=1}^{MK}|\overline{V}_{mk}|^2 = 1, \forall k$, and hence that the pre-coder does not change the transmitted power – that is the k^{th} diagonal element of $\mathbf{A}$:

$$A_{kk} = \frac{1}{\sqrt{\|[\mathbf{H}^H(\mathbf{H}\mathbf{H}^H)^{-1}]_k\|^2}} \tag{4.15}$$

Then the length K received signal vector at the UEs, omitting noise:

$$\tilde{\mathbf{y}} = \mathbf{H}\overline{\mathbf{V}}\mathbf{s} = \mathbf{H}\mathbf{H}^H(\mathbf{H}\mathbf{H}^H)^{-1}\mathbf{A}\mathbf{s} = \mathbf{A}\mathbf{s} \tag{4.16}$$

and thus A_{kk}^2 is the power gain for the k^{th} user between the input of the CPU precoder and the receiver at the UE.

4.4.1 Determinant of G

The performance of the system will be strongly dependent on the determinant of $\mathbf{G} = \mathbf{H}\mathbf{H}^H$, which appears as a divisor in the calculation of its inverse and thus as a multiplier in the calculation of $\mathbf{A}$: hence if the determinant is small we can also expect the received signal at the user to be small. Thus we next investigate the conditions under which the determinant tends to zero: that is, when the matrix $\mathbf{G}$ becomes ill-conditioned.

Now $\mathbf{H}_m\mathbf{V}_m$ is a $K \times K$ matrix in which the kk'-th element:

$$[\mathbf{H}_m\mathbf{V}_m]_{kk'} = \mathbf{h}_{mk}\mathbf{v}_{mk'} = \exp(i\omega_{mk})\sqrt{\beta_{mk}}\mathbf{v}_{mk}^H\mathbf{v}_{mk'} \tag{4.17}$$

and:

$$\mathbf{v}_{mk}^H\mathbf{v}_{mk'} = \begin{cases} \|\mathbf{V}_{mk}\|^2 = 1, k = k' \\ \rho_{mkk'}, k \neq k' \end{cases} \tag{4.18}$$

where $\rho_{mkk'}$ denotes the correlation coefficient between the steering vectors towards the k^{th} and the k'^{th} users from the m^{th} AP.

The most fundamental question in analysing the performance of this system is the extent to which a pair of closely spaced users may be separated, and for this reason we now focus on the two user case. Since ZF is used it is in principle possible to remove mutual interference between them as long as the matrix $\mathbf{G}$ can be accurately inverted: however as discussed above when the determinant is small, for given transmit power the received signal on the downlink will be reduced, and hence the signal to noise ratio (SNR) will be reduced. (On the uplink an equivalent process will occur, but in this case the ZF detection at the CPU will have the effect of enhancing the received noise – but again an equivalent degradation in SNR will occur).

Now:

$$\mathbf{G} = \sum_{m=1}^{M} (\mathbf{H}_m\mathbf{V}_m)(\mathbf{H}_m\mathbf{V}_m)^H \tag{4.19}$$

and hence the kk'-th element is given by:

$$
\begin{aligned}
[\mathbf{G}]_{kk'} &= \sum_{m=1}^{M}\sum_{i=1}^{K}[\mathbf{H}_m\mathbf{V}_m]_{ki}[\mathbf{H}_m\mathbf{V}_m]^*_{k'i} \\
&= \sum_{m=1}^{M}\sum_{i=1}^{K}\left(\exp\left(i\left(\omega_{im}-\omega_{km}\right)\right)\sqrt{\beta_{km}}\rho_{mki}\left(-i\left(\omega_{im}-\omega_{k'm}\right)\right)\sqrt{\beta_{k'm}}\rho^*_{mk'i}\right) \\
&= \sum_{m=1}^{M}\left(\exp\left(i\left(\omega_{k'm}-\omega_{km}\right)\right)\sqrt{\beta_{km}\beta_{k'm}}\sum_{i=1}^{K}\rho_{mki}\rho^*_{mk'i}\right)
\end{aligned}
\tag{4.20}
$$

The diagonal elements simplify to:

$$
[\mathbf{G}]_{kk} = \sum_{m=1}^{M}\beta_{km}\sum_{i=1}^{K}|\rho_{mki}|^2 \tag{4.21}
$$

For the two-user case of course k,k',i take only the values 1 and 2, and for $k,k' = i, \rho_{mki}, \rho^*_{mk'i} = 1$, and we can simplify the notation by writing $\rho_{m12} = \rho^*_{m21}$ as ρ_m. The matrix can then be written as

$$
\mathbf{G} = \begin{bmatrix}
\sum_{m=1}^{M}\beta_{1m}\left(1+|\rho_m|^2\right) & \sum_{m=1}^{M}2\exp\left(-i\left(\omega_{1m}-\omega_{2m}\right)\right)\sqrt{\beta_{1m}\beta_{2m}}\rho_m \\
\sum_{m=1}^{M}2\exp\left(i\left(\omega_{1m}-\omega_{2m}\right)\right)\sqrt{\beta_{1m}\beta_{2m}}\rho^*_m & \sum_{m=1}^{M}\beta_{2m}\left(1+|\rho_m|^2\right)
\end{bmatrix}
\tag{4.22}
$$

The determinant is given by the product of the diagonal terms minus the product of the off diagonals, and is given as

$$
\begin{aligned}
det\left(\mathbf{G}\right) &= \sum_{m=1}^{M}\sum_{m'=1}^{M}\beta_{1m}\beta_{2m'}\left(1+|\rho_m|^2\right)\left(1+|\rho_{m'}|^2\right) \\
&- \sum_{m=1}^{M}\sum_{m'=1}^{M}4\exp\left(-i\left(\omega_{1m}-\omega_{1m'}-\omega_{2m}+\omega_{2m'}\right)\right)\times\sqrt{\beta_{1m}\beta_{1m'}\beta_{2m}\beta_{2m'}}\rho_m\rho_{m'}^{*} \\
&= \sum_{m=1}^{M}\Bigg(\beta_{1m}\beta_{2m}\left(1-|\rho_m|^2\right)^2 \\
&+ \sum_{m'=1}^{m-1}\Bigg(\left(\beta_{1m}\beta_{2m'}+\beta_{1m'}\beta_{2m}\right)\left(1+|\rho_m|^2\right)\left(1+|\rho_{m'}|^2\right) \\
&- 8\cos\left(\omega'_{mm'}\right)\sqrt{\beta_{1m}\beta_{1m'}\beta_{2m}\beta_{2m'}}|\rho_m||\rho_{m'}|\Bigg)\Bigg)
\end{aligned}
\tag{4.23}
$$

in which $\omega'_{mm'}=\omega_{1m}-\omega_{1m'}-\omega_{2m}+\omega_{2m'}-\omega_{\rho_m}+\omega_{\rho'_m}$ where ω_{ρ_m} is the phase of ρ_m.

The expression 4.23 leads to our main result:

Theorem: The matrix $\mathbf{G}$ is singular, and hence the pre-coder cannot be obtained, if and only if the following are simultaneously true for all $m,m',m'<m$:

$$
\begin{aligned}
\beta_{1m}\beta_{2m'} &= \beta_{1m'}\beta_{2m} && (a)\\
|\rho_m| &= |\rho_{m'}| = 1, \text{and} && (b)\\
\omega'_{mm'} &= 0 && (c)
\end{aligned}
$$

Proof: We can rewrite:

$$
\begin{aligned}
&\left(\beta_{1m}\beta_{2m'}+\beta_{1m'}\beta_{2m}\right)\left(1+|\rho_m|^2\right)\left(1+|\rho_{m'}|^2\right)-8\cos\left(\omega'_{mm'}\right) \\
&\qquad\sqrt{\beta_{1m}\beta_{1m'}\beta_{2m}\beta_{2m'}}|\rho_m||\rho_{m'}| \\
&= \frac{1}{2}\left[\left(|\rho_m|-|\rho_{m'}|\right)^2+\left(1-|\rho_m||\rho_{m'}|\right)^2+4\left(1-\cos\left(\omega'_{mm'}\right)\right)|\rho_m||\rho_{m'}|\right] \\
&\qquad\times\left(\sqrt{\beta_{1m}\beta_{2m'}}+\sqrt{\beta_{1m'}\beta_{2m}}\right)^2 \\
&+\frac{1}{2}\left[\left(|\rho_m|-|\rho_{m'}|\right)^2+\left(1-|\rho_m||\rho_{m'}|\right)^2+4\left(1+\cos\left(\omega'_{mm'}\right)\right)|\rho_m||\rho_{m'}|\right] \\
&\qquad\times\left(\sqrt{\beta_{1m}\beta_{2m'}}-\sqrt{\beta_{1m'}\beta_{2m}}\right)^2
\end{aligned}
$$

In this expression the terms $\left(1-\cos\left(\omega'_{mm'}\right)\right)$ and $\left(1+\cos\left(\omega'_{mm'}\right)\right)$ are clearly non-negative: all other terms are quadratic and thus also non-negative. Since $\sqrt{\beta_{1m}\beta_{2m'}}+\sqrt{\beta_{1m'}\beta_{2m}}$ is always positive and non-zero (except, trivially, as $\beta_{1m}\beta_{2m'}$ and $\beta_{1m'}\beta_{2m}$ both tend to zero) the first term is zero if and only if $|\rho_m| - |\rho_{m'}| = 0$, $1-|\rho_m||\rho_{m'}| = 0$, and $1-\cos\left(\omega'_{mm'}\right)=0$. The second term is zero either if $|\rho_m| - |\rho_{m'}| = 0$, $1-|\rho_m||\rho_{m'}| = 0$, and $1+\cos\left(\omega'_{mm'}\right)=0$, or if $\sqrt{\beta_{1m}\beta_{2m'}}-\sqrt{\beta_{1m'}\beta_{2m}}=0$. Since $1+\cos\left(\omega'_{mm'}\right)\neq 0$ if $1-\cos\left(\omega'_{mm'}\right)=0$, both terms can only be zero if $|\rho_m| - |\rho_{m'}| = 0$, $1-|\rho_m||\rho_{m'}| = 0$, and $1-\cos\left(\omega'_{mm'}\right)=0$, and $\sqrt{\beta_{1m}\beta_{2m'}}-\sqrt{\beta_{1m'}\beta_{2m}}=0$. These statements are simultaneously true under the joint conditions listed in the theorem. The inner summation in 4.23 contains $m-1$ terms of this form: the determinant is zero only if these are all zero. Hence the conditions must be satisfied for all $m' < m$. There is also an additional term $\beta_{1m}\beta_{2m}\left(1-|\rho_m|^2\right)^2$ in the outer summation, which will also be zero if $|\rho_m|=1$. And of course all terms of the outer summation must be zero, so the conditions must hold for all $m \leq M$.

4.4.2 Implications and Specific Cases

The theorem also indicates under what conditions the determinant may be small, in addition to the trivial condition that all path losses are large. These are the conditions under which the conditions (a), (b) and (c) of the theorem are nearly fulfilled. Assuming the Friis law applies, condition (a) requires that $d_{1m}d_{2m'} \approx d_{1m'}d_{2m}$, which is clearly fulfilled if UE1 and UE2 are close to one another. (In fact it might also be fulfilled if they both lie on the perpendicular bisector of the line between the two APs). However, since path loss varies relatively slowly with location, it might be approximately fulfilled for quite a wide range of locations.

Condition (b) requires that the steering vectors of the two users from both APs are strongly correlated, which implies that their relative angle from the APs is close. Again this is likely to mean that the UEs must be close together, but in this case the correlation of the steering vectors also depends on the size of the arrays: the larger the aperture, the smaller the correlation, and hence the smaller the distance must be to affect the determinant significantly.

Condition (c) depends on the relative phases of the signals from the two APs at the two UEs: while these may be correlated when the UEs are very close together (at a distance comparable with a wavelength), this is very unlikely in practice, and thus $\omega'_{mm'}$ may be treated as random. It is made up of four random variables with uniform distribution over 2π, and since it is the sum of these taken modulo 2π that affects the determinant, this also can be treated as having the same uniform distribution. Then if the random phase is close to zero, and assuming both conditions (a) and (b) also apply, the determinant and hence the signal

strength may be significantly reduced. Note that we can obtain a "worst case" for the random fading caused by this by setting $\omega'_{mm'} = 0$ in the simulation.

There are some special cases which may be of particular interest. First, if there is only one AP, the outer summation in 4.15 has only one term, with $m = 1$, and the inner summation has no terms. Hence the determinant becomes:

$$det\left(\mathbf{G}\right) = \beta_{11}\beta_{21}\left(1-|\rho_1|^2\right)^2 \tag{4.24}$$

This will be diminished if the steering vectors of the two users are strongly correlated, that is, if they are close together in angle, whether or not they are also close together in space. For two APs there are two terms in the outer summation of 4.22 and only one in the inner. The determinant is:

$$\begin{aligned} det\left(\mathbf{G}\right) &= \beta_{11}\beta_{21}\left(1-|\rho_1|^2\right)^2 + \beta_{12}\beta_{22}\left(1-|\rho_2|^2\right)^2 \\ &+ \left(\beta_{12}\beta_{21}+\beta_{11}\beta_{22}\right)\left(1-|\rho_2|^2\right)\left(1-|\rho_1|^2\right) \\ &- 8\cos\left(\omega'_{21}\right)\sqrt{\beta_{12}\beta_{11}\beta_{22}\beta_{21}}|\rho_2||\rho_1| \end{aligned} \tag{4.25}$$

As before, this will approach zero only if $|\rho_1| = |\rho_2| = 1$, which will occur only if the two UEs are close together in angle from both APs. In this case the expression becomes:

$$\begin{aligned} det\left(\mathbf{G}\right) &= 4\left(\beta_{12}\beta_{21}+\beta_{11}\beta_{22}\right) - 8\cos\left(\omega'_{21}\right)\sqrt{\beta_{12}\beta_{11}\beta_{22}\beta_{21}} \\ &= 4\left(\sqrt{\beta_{12}\beta_{21}}-\sqrt{\beta_{11}\beta_{22}}\right)^2 + 8\cos\left(1-\cos\left(\omega'_{21}\right)\right)\sqrt{\beta_{12}\beta_{11}\beta_{22}\beta_{21}} \end{aligned} \tag{4.26}$$

Again this may approach zero if $\beta_{12}\beta_{21} \approx \beta_{11}\beta_{22}$, provided also $\omega'_{21} \approx 0$. Note however that in this case the determinant depends on only one angle, and if the other conditions are fulfilled there is a relatively high probability that this angle is small.

For a larger number of APs there may be many more terms in the expression. For M APs there are $M(M-1)/2$ inner summation terms, each depending on an uncorrelated random angle, and hence the probability that all terms will approach zero becomes very small, even if the users are close together. In addition the users are much less likely to have correlated steering vectors from all the APs unless they are very close together. This shows the benefit of a distributed massive MIMO system in this scenario.

4.4.3 Phase Errors at Transmitting APs

In a distributed MU-MaMIMO for mmWave communication, the phase of signals from all the operating APs require to be controlled accurately. This can be achieved by ensuring the stability of the oscillators and channels. In this chapter, we have investigated the effect of induced phase error in mmWave oscillators. In practice, the phase synchronization at the APs may be imperfect, which would mean there is a random phase error ϑ_m in all the signals transmitted from the m^{th} AP. This can be modelled by multiplying the vector $\mathbf{S}$ of input signals to the APs by a diagonal error matrix:

$$\mathbf{E} = \begin{bmatrix} exp(i\vartheta_1)\mathbf{I}_1 & 0 & \dots & 0 \\ \vdots & & \ddots & \vdots \\ 0 & & \dots & 0 \quad exp(i\vartheta_M)\mathbf{I}_1 \end{bmatrix} \tag{4.27}$$

The received signal is then:

$$\tilde{\mathbf{y}} = A\mathbf{H}\mathbf{E}\overline{\mathbf{V}}\mathbf{s} + \mathbf{z} = A\mathbf{H}\mathbf{E}\mathbf{H}^H(\mathbf{H}\mathbf{H}^H)^{-1}\mathbf{s} + \mathbf{z} \tag{4.28}$$

However, the matrix $\mathbf{B} = \mathbf{H}\mathbf{E}\mathbf{H}^H(\mathbf{H}\mathbf{H}^H)^{-1}$ is no longer an identity matrix, and no longer diagonal, which gives rise to inter-user interference. The signal is given by the diagonal elements and the interference by the off-diagonals. The signal to interference plus noise ratio at UEi is given by:

$$SINR_i = \frac{B_{ii}^2}{\sum_{m=1,m\neq i}^{M} B_{im}^2 + \frac{\sigma_z^2}{A^2}} \tag{4.29}$$

4.5 Results and Discussion

To illustrate these implications for the scheme we compute numerical results for the scenario described in Section 4.2 above, and illustrated in Fig. 4.1, showing results for 4 APs. As we have seen in chapter 3, that for a square shaped open area using 4 APs at four corners ensures the best quality of service in terms of processing power and cost of the system. The total transmit power per AP in 2UE case is 33dBm. The noise figure at the receivers is 10 dB in a bandwidth of 1.5 GHz and carrier frequency is 26 GHz. The APs are at 6 metres in height, and the UEs at 1.5 metres.

In this section, the results are shown to illustrate the performance of MU-MaMIMO environment using BF and ZF pre-coding techniques. Moreover, it is observed that for a particular arrangements of APs, the number of UEs that can be served in the proposed

simulation area of coverage and the effectiveness of using ZF pre-coding to eliminate the noise to provide best service to the UEs. For the simplicity of the analysis we have started with only 2 UEs. We show the variation in correlation between the steering vectors of the UEs throughout the service area. To prepare the contour plot to project the correlation we divided the area into grids as described in chapter 3. Here, we are assuming that one user is fixed in position (-10,15,1.5) metres with respect to the centre of the square. The simulation parameters are given in Table 4.1.

Table 4.1 Simulation parameters

Parameter	**Setting**
Coverage area	$100 \times 100\ m^2$
Power per UE, P_{UE}	33dBm
Carrier frequency, f_c	26 GHz
Bandwidth	1.5 GHz
Noise figure	10 dB
Temperature	290 K
Number of AP	4
Receiving antenna gain, G_{UE}	1
Antenna efficiency	100%

Figure 4.2 shows contour plots for the average correlation coefficient of steering vectors from all 4 APs versus the position of the fixed UE, for 10×10 arrays (Fig. 4.2a), 20×20 arrays (Fig. 4.2b) and 50×2 arrays (Fig. 4.2c). The figures show that correlation is consistently high (above 0.8) only in a very restricted area around the fixed user. This is the region that lies within the intersection of the beams from each of the APs, and hence the correlation peak is more confined, and the correlation away from it smaller. As mentioned in condition (b) of the theorem in Section 4.4.2, the correlation of the steering vectors depends on the size of the arrays. Particularly, in this case the horizontal size of the AP array. The larger aperture results in smaller correlation. The reason behind this is the width of the correlation peak is determined by the beamwidth, which in turn is determined by the aperture of the arrays. Fig. 4.2a shows larger correlation region among three figures, where the APs are 10×10 arrays and the beamwidths of the arrays are about $\frac{50.8\lambda}{Aperture} = 10^{\circ}$. Whereas for 20×20 arrays (Fig. 4.2b) the beamwidths are about 5° and for 50×2, they are around 2°. Hence, it is evident that as the beamwith becomes narrower, the correlation region reduces. In Fig. 4.2c, a significant reduction in correlation region is observed for 50×2 arrays.

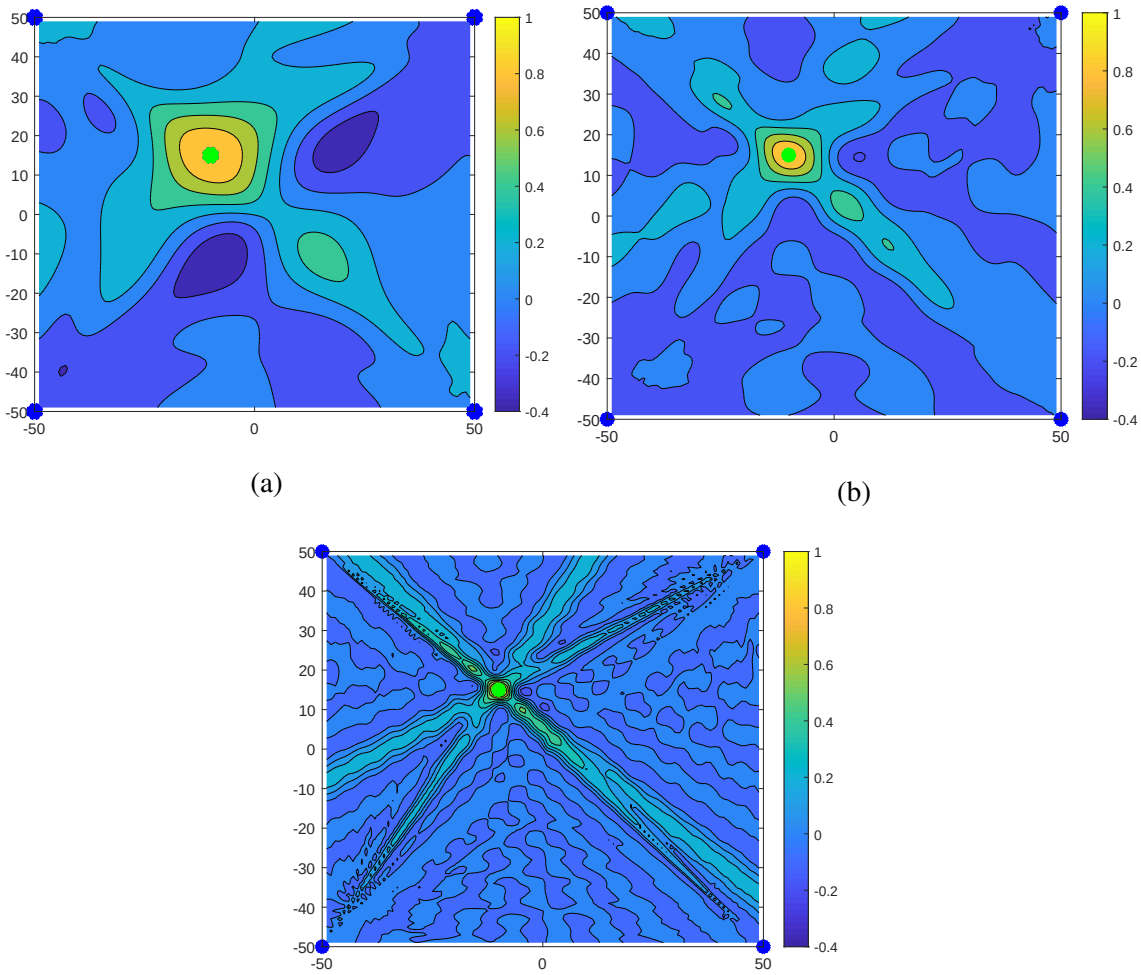

(a)

(b)

(c)

Fig. 4.2 Correlation of steering vectors of fixed user (marked in green), and test user, as test user moves around service area from 4 APs (marked in blue), (a) 10×10 array; (b) 20×20 array and (c) 50×2 array

Figure 4.3 shows the contour plots of the SINR experienced by the UE placed in each grid position in the presence of a fixed UE in position (-10,15,1.5) where 4 APs are transmitting using only beamforming technology. Fig. 4.3a shows the SINR contour for 10×10 arrays and, it is observed that due to the presence of the fixed UE the performance is heavily affected (the SINR value is around 7dB) in the area where both the UEs are highly correlated. The fixed UE is positioned close to the AP placed at (-50,50,6) and it is seen that along the vicinity of the fixed UE, the SINR values continue to drop diagonally through the opposite corner where another AP is placed. The areas near the two other APs exhibit better SINR as expected. At the upper right corner the SINR is around 40dB and to the lower left corner, it

is above 30dB. In Fig. 4.3b and 4.3c, we can see that the pattern of the of the contour plot follows as in Fig. 4.3a but the affected area reduces and the SINR improves as shown in their respective correlation plots. This is due to the narrower beamwidth for 20×20 and 50×2 cases and in addition, for 20×20 array, the array gain increases as well. The 50×2 arrays provides the best performances as the SINR values are over 30dB in most places (yellow zones).

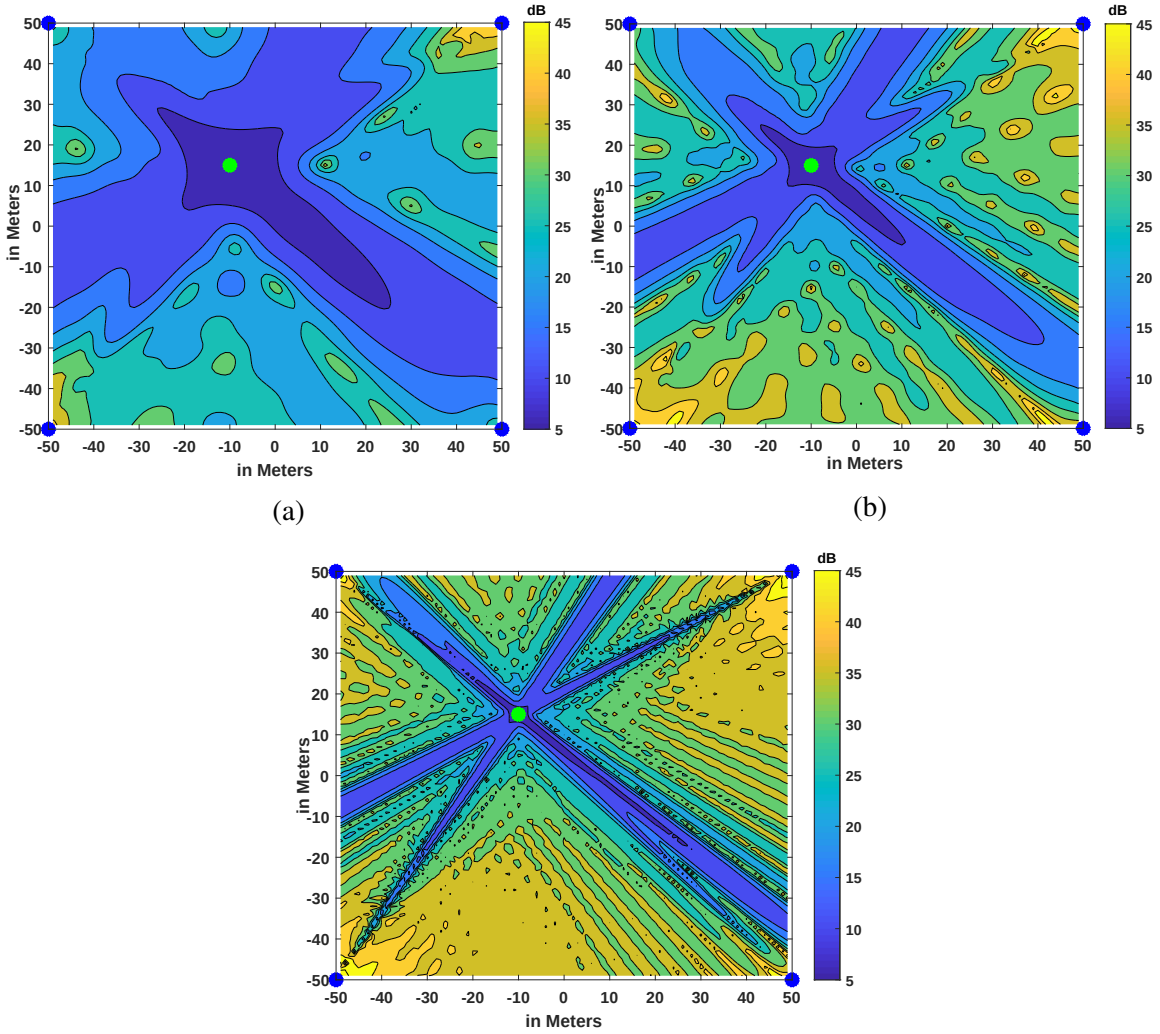

Fig. 4.3 Contour plots for the SINR of a fixed user (marked in green) and and test user, served by 4 APs (marked in blue), (a) 10×10 array; (b) 20×20 array and (c) 50×2 array

Figure 4.4 illustrates the resulting SNR with 4 APs, using ZF pre-coding technique. The simulation scenario is maintained like the previous cases for 2 UEs. Here, we set the random phase shift on the path between all APs and all UEs to zero, resulting in a “worst

case" scenario, as discussed above in condition (c) of the theorem in Section 4.4.2. If the random phase is set to zero, for instance where two UEs are close to each other and strongly correlated, the signal strength may be significantly reduced. Fig. 4.4a and 4.4c have identical total number of antenna elements i.e 100 in each array with different arrangements. It is seen in both figures that there is a large region around the centre of the service area with uniform SNR of around 38 dB. For 10×10 array case (Fig. 4.4a), the immediate vicinity around the fixed UE suffers very low SNR of almost 8dB that is approximately 30dB drop and the affected region is large compare to 50×2 case. In Fig. 4.4c with four 50×2 arrays, the affected region due to high correlation between two UEs reduces remarkably because of the narrower horizontal beam. For 20×20 arrays the overall SNR increases as the gain increases up to around 44dB and small amount of area near the fixed UE suffers low SNR (about 26dB) due to the higher array gain emerging from the increased number of antennas.

Figure 4.5 shows the contour plots of the SNR for 2 UE case where 4 APs are serving. Similar to the previous scenario where we applied ZF based pre-coding to eliminate the interference between the UEs but here the phase shifts on the paths between all APs and all UEs are randomly chosen for each grid position. We maintain the same three antenna arrangements as in the previous figure. It is observed that, unlike the "worst case", near the grid where two UEs are placed very closely, the SNR randomly varies. We can see the rise of SNR in places and some black spots where the SNR falls rapidly. This is because of the constructive and destructive merging of the signals with random phase shifts. The overall SNR follows as the previous figure where we have seen performance boost using 20×20 arrays (Fig. 4.5b). The SNR variation in 10×10 (Fig. 4.5a) and 20×20 array case is prominent than in 50×2 (Fig. 4.5c) array case. As the beamwidth from 50×2 array is narrower the variation is less hence the performance is more uniform and the SNR drop is around 3dB in few places. Whereas, for 10×10 and 20×20 array scenario the SNR goes down almost 7dB to 9dB in places (shown in black spots). For 50×2 arrays, the SNR values are above 38dB almost throughout the area and for 20×20 the SNR values are increased over 44dB excepts the major drops near the intersection between the UEs.

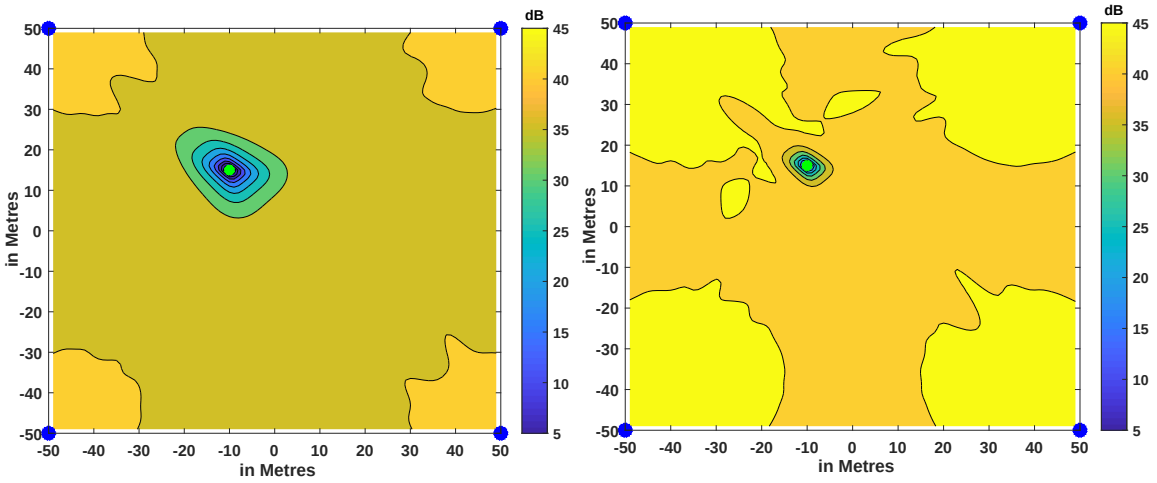

(a) (b)

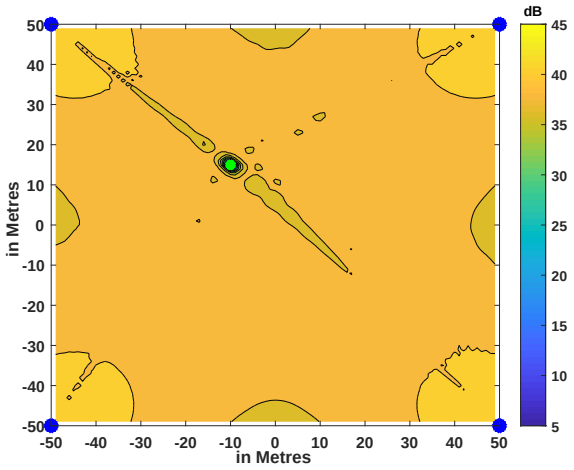

(c)

Fig. 4.4 SNR for case of 4APs versus position of test user for 2 user case, with a fixed user marked in green – in a "worst case" SNR, with $\omega_{mm'}$ set to zero, (a) 10×10 array; (b) 20×20 array and (c) 50×2 array

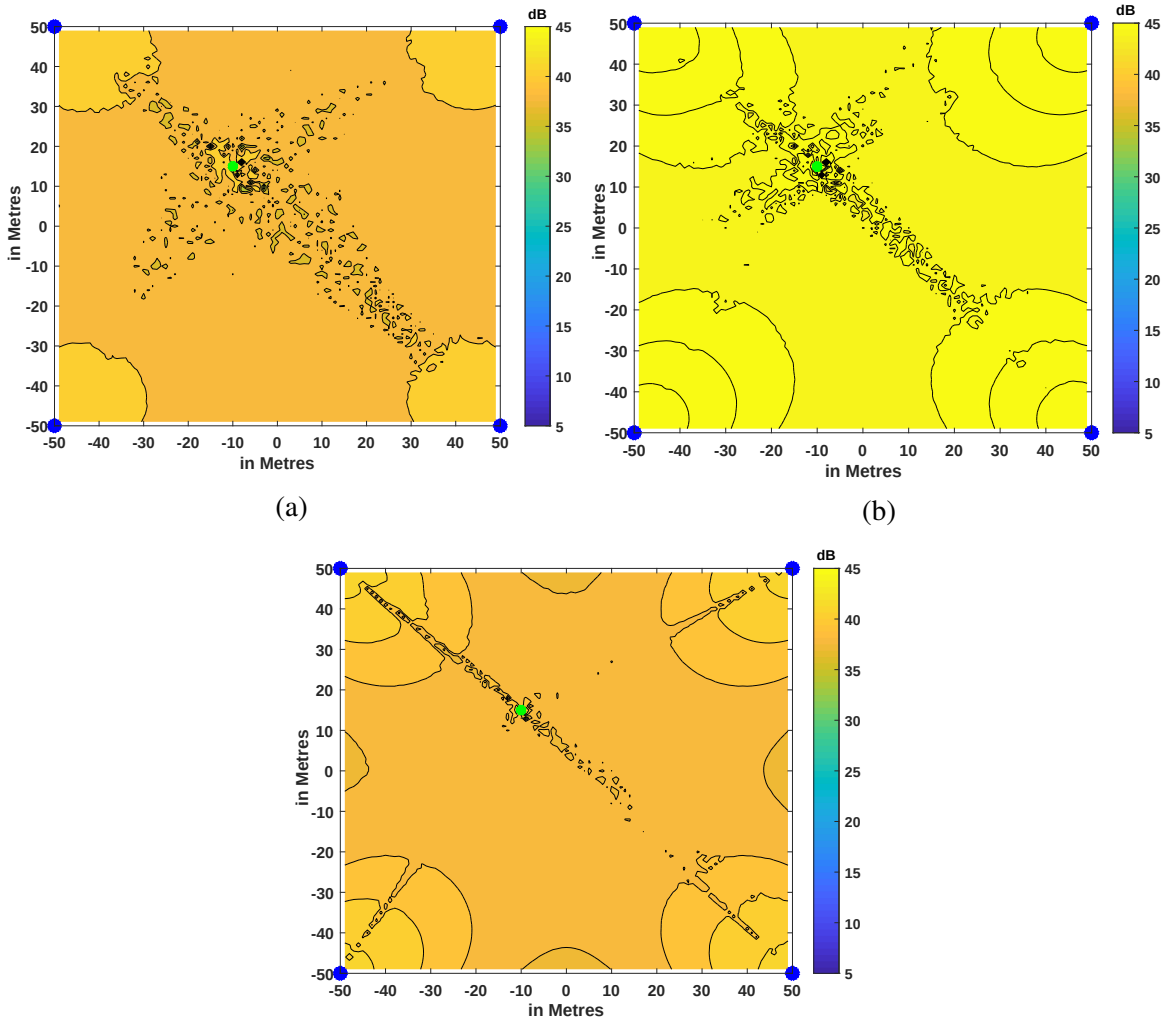

Fig. 4.5 Contour plot for SNR in 2 AP, two user case, showing practical case with random phase shifts (a) 10×10 array; (b) 20×20 array and (c) 50×2 array

Figure 4.6 shows the cumulative distribution function (CDF) of the SNR for the two user case, comparing the "worst case" scenario used in Fig. 4.4, in which all AP-UE phase shifts are set to zero, with the results of randomly chosen phase shifts in Fig. 4.5 for different arrangements of APs. The CDF of SNR values are of the UE placed at the grid points with the presence of a fixed UE at at (-10,15,1.5) point. It is seen that if we increase the antenna elements per AP the SNR improves due to increasing antenna gain. For the same total number of elements but different shaped arrays i.e 10×10 and 50×2, the changes in SNR value is not very noticeable above 10^{th} percentile. At 5^{th} percentile, the difference is around 2dB for the "worst case" to the randomise phase case for for 10×10 array. Moreover, there is a

long “tail” of low SNR for the “worst case” corresponding to locations very close to the fixed user where the steering vector correlation is high. However, in the case of randomised phase the probability of reaching these low SNR values is much reduced, showing that even users that are very close to one another may in principle be separable due to the differences in phase. Moreover, it is seen that the SNR increased around 3dB where the number of antenna elements are increased from 400 to 1600 using 10×10, 15×15 and 20×20 arrays.

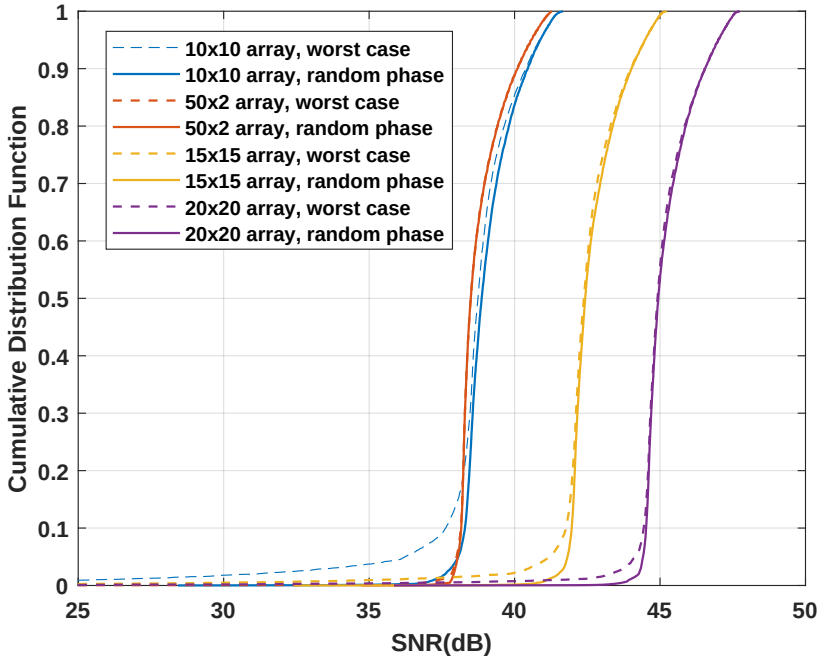

Fig. 4.6 The CDF of SNR for different AP arrangements

In Fig. 4.7, we compare these both techniques that we discussed for 10×10 (4.7a) and 50×2 (4.7b) arrays. We choose these two that have identical total number of antenna elements but in different arrangements. In both plots we can see that as we have kept the difference in heights between the AP and UE small using only the BF technique on 2 UEs degrades the performance significantly. For 10×10 arrays, at 10^{th} percentile, the SINR level drops to approximately 27dB and at 50^{th} percentile, the difference is around 20dB. Moreover, when we look into the 50×2 array system, at 10^{th}, this variation is around 22dB but at 50^{th} percentile, the difference in their SINR values reduced to around 7dB. This is because of the shaping of the beamwidth. As we have discussed before that when the antennas elements are greater in the horizontal direction than that are of in the vertical direction, the beamwidth becomes narrower which in turns reduces the high correlation space (shown in Fig. 4.2c) and exhibits better user separation.

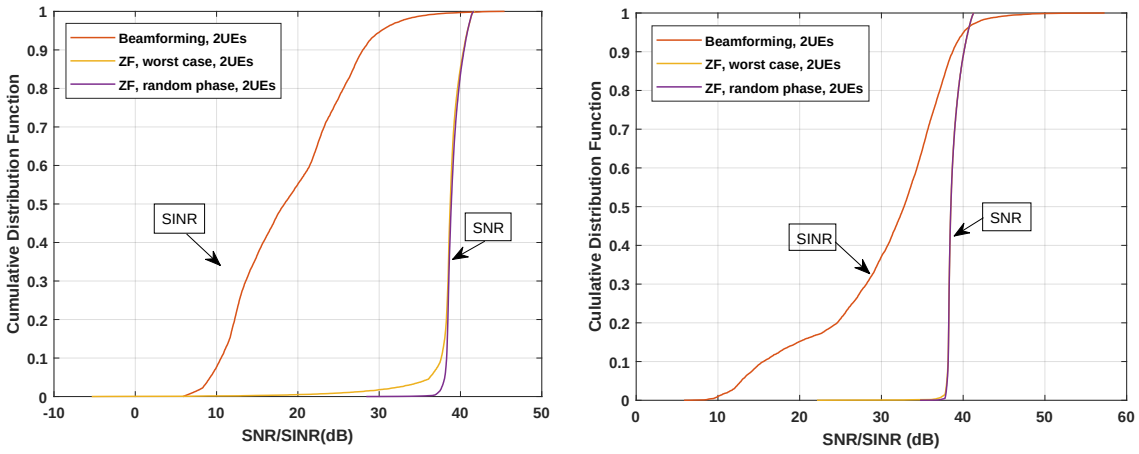

(a) (b)

Fig. 4.7 The CDF of SNR for different scenarios, (a) 10×10 array; and (b) 50×2 array

For a distributed MU-MaMIMO approach in mmWave band, one of the major concerns is the synchronization of all the operating APs. So far we have observed in this chapter that it is feasible to perform accurate ZF pre-coding on the downlink of a mmWave distributed system. Hence, it is important to control the phase of signals from multiple APs accurately enough to combine coherently at the UE. This would require oscillators and channels which are sufficiently stable for a phase estimate acquired on the uplink to be usable on the downlink. It is to be noted that there is less of an issue for uplink ZF detection, since channel estimates acquired on the uplink can then be used immediately. This requires investigation in the context of data on stability and phase noise in mmWave oscillators. To encounter this issue we introduced various degrees of phase error at the transmitting signals. The phase error follows the random gaussian and uniform random distribution. Fig. 4.8 shows the SNR values at 10^{th} percentile of the distribution for different degrees phase noises utilizing various configurations of AP arrays. From Fig. 4.8a, it is clearly seen, that the 50×2 arrays show the best curve among all the AP configurations used for a gaussian distribution of phase noise. We can notice that for small deviations such as 2° and 5° the SNR values are slightly shifted. From 0° to 5° the SNR drops about 2dB. Whereas, for 10×10 arrays the SNR reduced approximately 10dB. Moreover, for 15×15 and 20×20 arrays, the SNR is significantly higher at 0° but the SNR decreases more than 10dB for a small deviation such as 5°. The performance continues to degrade with increasing deviation in the generated phase noise. It is seen that with 20° deviation the SNR drops around 10dB. It can be said that the synchronization of all the operating APs should be considered carefully. The uniform

random distribution of the phase noise is shown in Fig. 4.8b to highlight the changes for higher degrees of deviation.

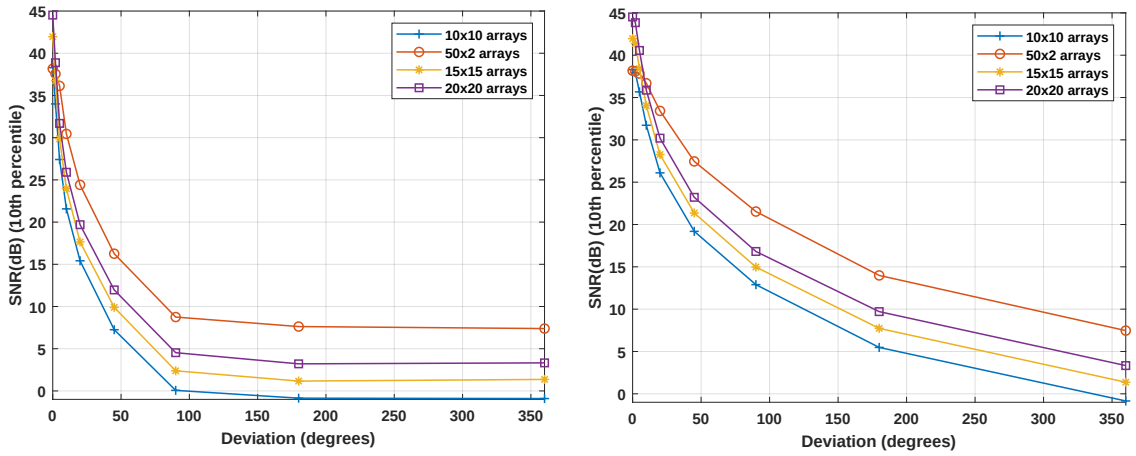

(a) (b)

Fig. 4.8 The SNRs at the 10^{th} percentile of the distribution using different AP arrays, where the added noise follows (a) random gaussian distribution; and (b) uniform random distribution

Up to this point, we have discussed the distributed MU-MaMIMO system using ZF precoding for only two users for the simplicity of analysis. This is very unlikely for a practical scenario. However, this approach can easily be adapted for a system that incorporates a large number of users for a given AP distribution. Fig. 4.9 presents the throughput per UE at the 10^{th} percentile of the distribution. This graph answers an important question of scaling up distributed MU-MaMIMO system: How many users can be served by a specific distribution of APs with given number of antenna elements for an outdoor LoS environment? The APs are placed at four corners of the square area (as discussed in 4.2). The throughput is calculated by an attenuated and truncated form of the Shannon bound defined in 3GPP standards (3GPP TR 38.921 V17.0.0 (2021-03)) [173]. The following equations are adapted to approximate the throughput over a channel with a given SINR:

$$Throughput(SINR), bps/Hz = \begin{cases} 0, & \text{for } SINR < SINR_{MIN} \\ \alpha \cdot S(SINR), & \text{for } SINR_{MIN} \leq SINR < SINR_{MAX} \\ \alpha \cdot S(SINR_{MAX}), & \text{for } SINR \geq SINR_{MAX} \end{cases} \tag{4.30}$$

where, $S(SINR)$ is the Shanon bound, $S(SINR) = log_2(1 + SINR)$ bps/Hz, α is the attenuation factor, 0.6 for DL, representing implementation losses, $SINR_{MIN}$ is the minimum

SNR of the code set that is -10dB for DL and $SINR_{MAX}$ is the maximum SNR of the code set, 30dB for DL. For a large number of users the transmitting power per AP is considered around 25dBm.

It is observed that 10×10 array distribution can serve up to 60 users using ZF algorithm. Whereas, with identical total number of antennas (i.e. 400), 25×4 and 50×2 systems can incorporate 90 and 150 users respectively. The user throughput can be increased significantly only by changing the shape of the arrays as well as the number of users that can be occupied. We can see that for 40 randomly distributed UEs, at 10^{th} percentile, the throughput per UE is below 1 bps/Hz for 10×10 arrays, whereas for 25×4 and 50×2 arrays, the values are approximately 3 and 3.37 bps/Hz respectively. Interestingly, in the 50×2 array system up to 120 users, the throughput per UE is above 1 bps/Hz which is twice the number of users that can be served by 10×10 arrays. Increasing the antennas per array, such as 15×15 and 20×20 arrays show improved throughput because of higher gain and narrow beamwidth. The 20×20 array system can provide service to up to 160 UEs, that is 10% of the total number of antenna elements at the transmitting end ($20 \times 20 = 400 \Rightarrow 400 \times 4 = 1600$). Similarly, 15×15 arrays serve users almost 10% of the total number of antenna elements in all the APs. Here, both the 20×20 and 50×2 array system is better in user separation and outperform other arrangements due to the narrower beamwidth and high gain. Up to 80 UEs because of high gain the 20×20 AP arrangement exhibits the best throughput per UE but beyond 80 UEs the 50×2 arrays outperform the 20×20 AP arrangement.

Figure 4.10 shows the 10th percentile of the total throughput for MU-MaMIMO system for different AP arrangements. We have provided results for three different types of AP configurations maintaining the total number of elements in them and other two AP arrangements with increasing the number of elements. The curves are promising regarding showing that similar throughput can be achieved using smaller number of antenna elements per AP compared to larger arrays by just changing the shape of the arrays. Here, we can observe that, at 10^{th} percentile, both 15×15 and 25×4 array arrangement have achieved almost similar throughput (orange and purple curves), except that with15×15 arrays we can serve up to 100 UEs. Similarly, both 20×20 and 50×2 arrays exhibit higher throughput: around 193 bps/Hz. The difference is, for 20×20 the highest throughput is achieved at a lower number users (70 UEs) than that of 50×2 arrays and can provide service up to 160 UEs. Whereas, in the 50×2 array scenario, the peak is at 90 UEs and can serve up to 150 UEs.

Fig. 4.11 shows the 10^{th} percentile of throughput per UE for large numbers of users for different levels of phase error utilizing various configurations of AP arrays. Fig. 4.11a presents the throughput for 10×10 arrays, 4.11b represents the performance for 20×20

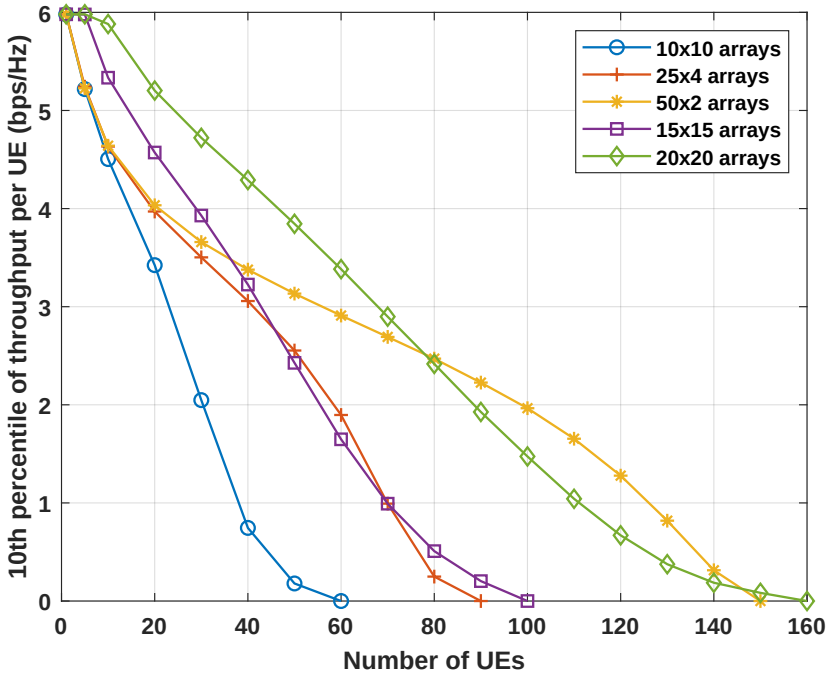

Fig. 4.9 10^{th} percentile of throughput per UE for multi-user scenario using different AP arrangements

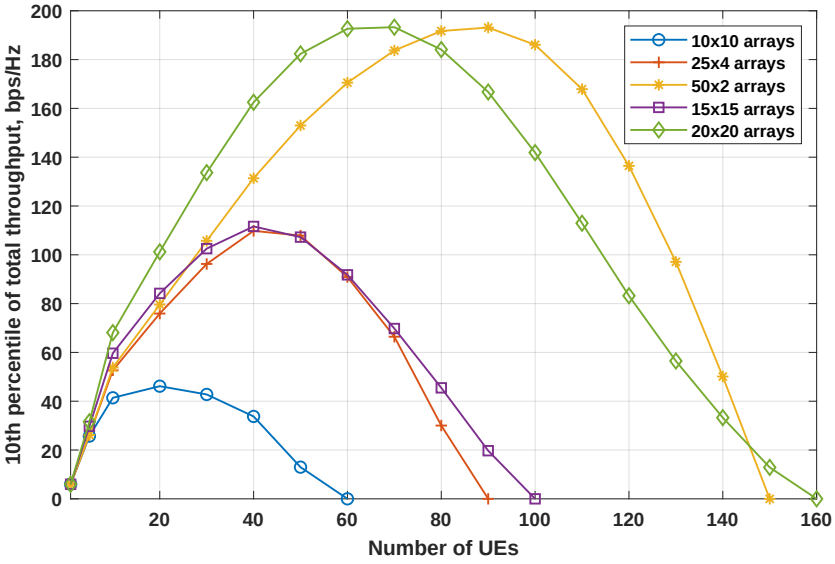

Fig. 4.10 10^{th} percentile of total throughput for multi-user scenario using different AP arrangements

arrays and 4.11c is for 50×2 arrays. As we have seen before regarding the 2 UE cases, at lower deviation of 0° and 5° the performance does not degrade badly. Among these 50×2 is least affected by these lower degree of deviation. Beyond 20° divergence the number of users served decreases along with the decreasing throughput per UE. It is evident that for 20° phase deflection, the induced error degrades the throughput per UE remarkably in all three arrangements and it continues to decrease for greater deviations. It can be said that the 50×2 array system surpasses other arrangements and with 90° divergence it serves up to 40 users which is highest among these three configurations.

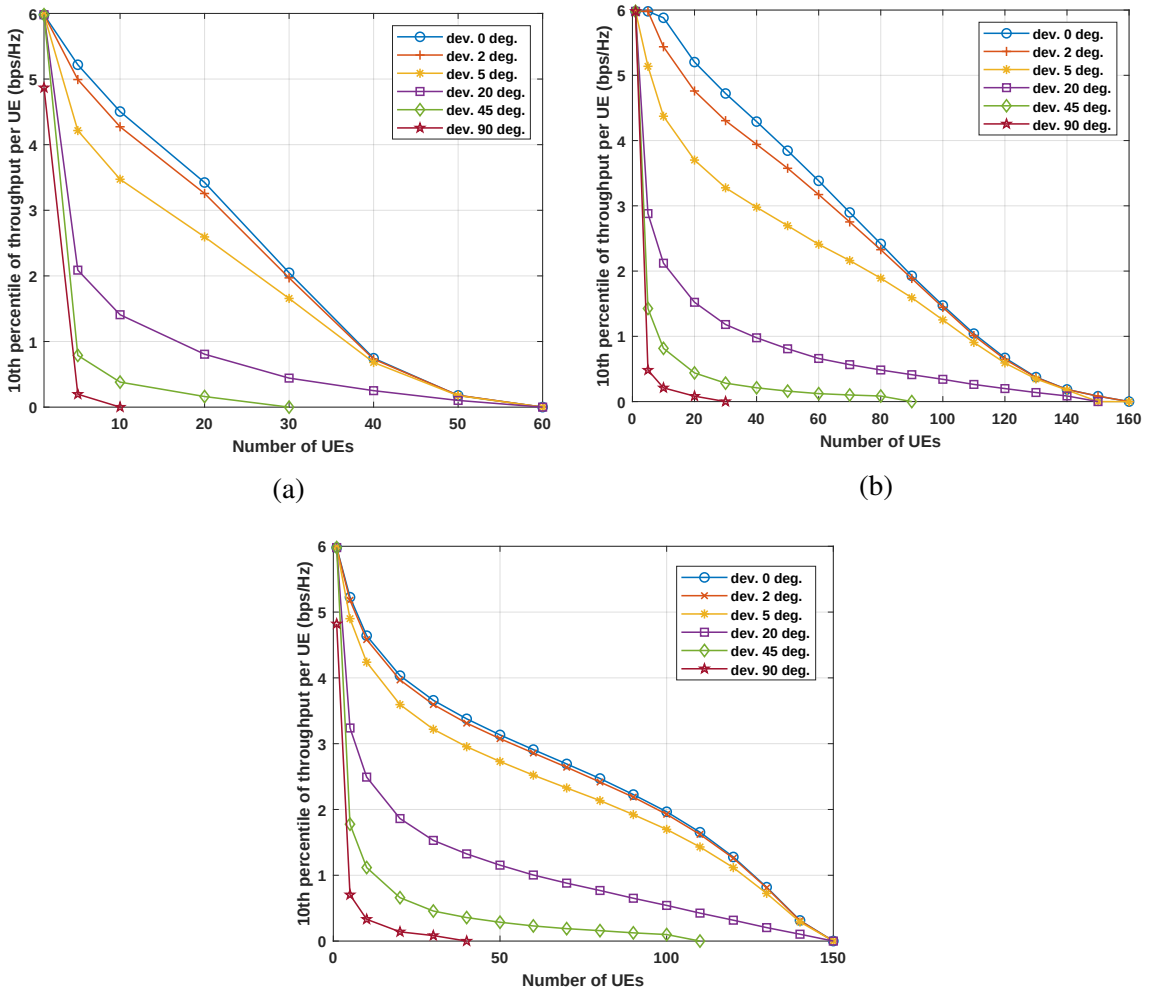

(a) (b)

(c)

Fig. 4.11 10^{th} percentile of throughput per UE including the various degrees of induced phase noise for multi-user scenario using different AP arrangements (a) 10×10 array; (b) 20×20 array and (c) 50×2 array

4.6 Summary

In this chapter, we have described the performance of a distributed multi-user massive MIMO system using BF and ZF pre-coding in a LoS scenario, with a view in particular to mmWave transmission. To reduce the complexity of the analysis, we have shown the simulation results for the two-user case for this chapter. We have also provided the results for a system with a large number of users using the ZF scheme. We have shown that the correlation between the steering vectors from 4 APs towards 2 UEs and the SINR performance using only beamforming. It is observed that using only the BF approach is not good enough to eliminate the inter-user interference. In order to effectively cancel the inter-user interference, a ZF pre-coding scheme is proposed. We have analysed in particular the numerical conditioning of the calculation of the ZF pre-coder by examining the determinant of the effective channel matrix. We prove a theorem defining three criteria to ensure a non-vanishing determinant of the pairwise effective channel matrix, the ZF approach successfully cancels the interference. Moreover, one of the crucial findings in this chapter is: for a certain coverage area, how many users can be effectively served by the distributed APs using ZF pre-coding. These simulation results will be useful in designing the AP distribution and their configuration for a desired number of users and coverage area for MU-MaMIMO architecture. It is clearly seen that an arrangement of AP arrays where the number of antenna elements is greater in the horizontal direction than in the vertical direction, the performance outperforms a square UPA array system. One of the important findings in this chapter is that just by changing the shape of the array, similar throughput can be achieved as for a square array with a much larger number of antenna elements. And finally, we address the phase synchronization issue for the distributed APs. We have shown how the phase error affects the received signal and degrades the overall performance. The performance decreases with an increasing degree of deviation. Hence, it is very important to design stable oscillators for mmWave communication.

Chapter 5

Multi-user D-MaMIMO System with Multi-antenna APs and UEs

5.1 Introduction

In previous chapters, directional multi-antenna arrays were in use at the transmitting end of the distributed massive multiple input multiple output (D-MaMIMO) system in millimetre wave (mmWave) communication, serving users equipped with only single antennas. However, this chapter considers multi-antenna arrays at the access point (AP) and at the user equipment (UE). We have observed in chapter 2 that multi-antenna arrays were employed in various studies on MaMIMO systems, either only at the APs or at both the AP and the UE. Modern user devices such as laptops, tablets and smart vehicles can accommodate multiple antennas to improve the multiplexing gain for better spectral efficiency [69]. Moreover, the mmWave band allows smaller antenna size and more compactness along with wider bandwidth which makes the multi-antenna user devices more feasible. According to [174] the deployment of five or ten antennas per device is quite reasonable in mmWave frequencies. As a result, evaluating the performance of mmWave D-MaMIMO with multiple antennas at the UEs is critical. The impact of various antennas at the user end requires to be studied to improve the systems' architecture. [69] studied cell-free MaMIMO (CF-MaMIMO) systems using multiple antennas at the AP and the UE. They have shown that, compared to single-antenna UEs, exploiting multi-antenna UEs enhances per-user net throughput. However, they have made this comparison for a limited number of elements at the transmitting AP as well as the users. [85] proposed a user centric approach for CF-MaMIMO at mmWave frequencies. In this approach each AP only transmits towards the UE that experience the best reception, which reduces the required backhaul capacity. However, in this approach, there is a chance

that some UEs may not be served by any of the APs. Generally, obtaining correct channel state information (CSI) for CF mmWave MaMIMO systems is a difficult task, and due to the large bandwidth and the close proximity of the APs, the combined channel from the APs to a UE is highly spatially correlated [87]. Several studies have been conducted on the capacity analysis of small scale MIMO considering perfect CSI [144][85] and imperfect CSI [85][175][176], although [174][177] assume that the UEs have the statistical CSI. However, [174] adopts MaMIMO with large antenna arrays but for centralised MaMIMO. In [88], for the multi-antenna multi-user scenario a combination of eigenmode decomposition and zero-forcing (ZF) is developed and water-filling is applied for optimal power distribution. The authors in [178] consider centralised MIMO system with multi-antenna UEs. They applied singular value decomposition (SVD) and ZF to reduce multi-user (MU) MIMO problem into the MU multiple-input-single-output (MISO) problem. While most of the papers deal with MaMIMO systems using smaller arrays, we propose a D-MaMIMO system with larger antenna arrays in mmWave communication. We assume perfect CSI is available. We present the comparison between single antenna UEs and multi-antenna UEs using a zero-forcing (ZF) pre-coding scheme. In the multi-antenna UE case, ZF pre-coding is applied between the UEs and among multiple elements of the same UE. We propose an approach combining eigenvalue decomposition (EVD) with ZF pre-coding to improve the system capacity by sending a single data stream toward individual users instead of multiple streams. The EVD decomposes the channel into parallel sub-channels among the UE antenna elements. Afterwards, the largest eigenvalue was detected to deliver the single data stream toward the intended UE. Then, we applied ZF between the UEs to cancel the interference. This will increase the probability of uniform user service. Furthermore, we compare the results of multi-antenna UEs with the results of single-antenna UEs from the previous chapter.

This chapter is structured as follows: the next Section 5.2 describes the system and channel model for the pure LoS channel, while Section 5.2.1 describes the ZF algorithm for multi-antenna UEs and Section 5.2.2 proposed the approach where EVD is combined with ZF pre-coding. Section 5.3 includes the numerical results and discussion and finally Section 5.4 summarizes the chapter.

5.2 System and Channel Model

In this chapter, we maintained the simulation scenario from previous chapters, considering a $100m \times 100m$ open square area containing 4 directional APs at four corners pointing towards the centre with 45° broadside to the walls. The APs and UEs are at 6 metres and 1.5 metres in

height respectively. We used uniform planar arrays (UPA) as APs and uniform linear arrays (ULA) as UEs. Fig. 5.1 depicts the proposed mmWave D-MaMIMO system.

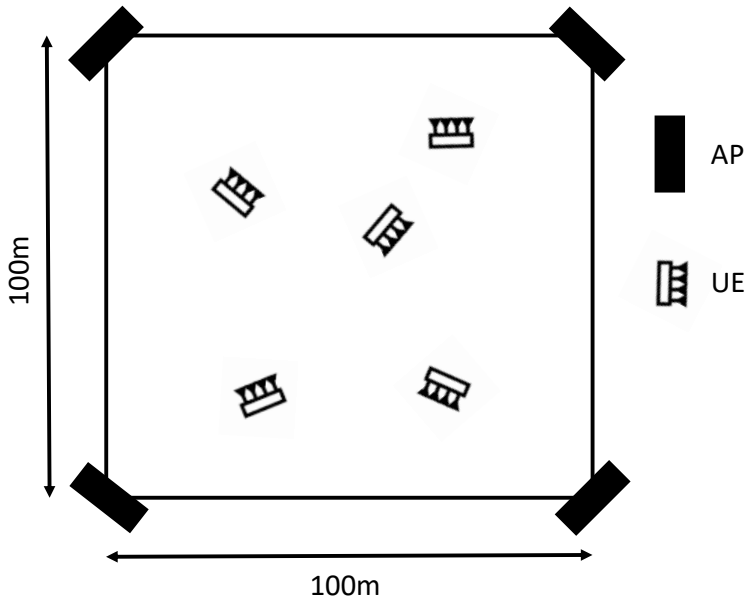

Fig. 5.1 Simulation scenario for multi-antenna APs and UEs [88]

Let us assume a downlink MU-MaMIMO system consisting of M APs and K UEs. The APs and UEs are equipped with N_T and N_R antennas each respectively. A backhaul network connects all the APs to a central processing unit (CPU). We also assume that the UE antennas are sufficiently close together that a single beam from each AP can cover them all. Therefore the received signal at the i^{th} UE is given by

$$\mathbf{y}_i = \sum_{m=1}^{M} \mathbf{H}_{im}\mathbf{x}_m + \mathbf{z}_i \tag{5.1}$$

where $\mathbf{x}_m$ is the transmitted signal vector from the m^{th} AP and $\mathbf{z}_i\,(N_R \times 1)$ is the noise at the i^{th} UE. The channel matrix between the m^{th} AP and the i^{th} UE can be written as:

$$\mathbf{H}_{im} = \exp\left(-i\vec{\omega}_{im}\right)\sqrt{\beta_{im}}\boldsymbol{\psi}_T^H\left(\theta_{im}\right) \tag{5.2}$$

where $\vec{\omega}_{im}$ is a $(N_R \times 1)$ vector giving the phase of the LoS path from APm to each element of UEi, i denotes the square root of -1, β_{im} is the path power gain. Again, $\boldsymbol{\psi}_T^H\left(\theta_{im}\right)$ is the $(1 \times N_T)$ steering vector of the transmitter array in the direction θ_{im}, which is the direction (relative to broadside) of UEi from APm and we assume, similar to chapter 4, that $\|\boldsymbol{\psi}_T^H\left(\theta_{im}\right)\|^2 = 1$.

The transmitted signal vector is in turn given by:

$$x_m = \sum_{k=1}^{K} \mathbf{V}_{km}\mathbf{s}_{km} \tag{5.3}$$

where $\mathbf{V}_{km}$ is the $(N_T \times N_R)$ pre-coding matrix applied at the m^{th} AP to the signals intended for the i^{th} UE, and $\mathbf{s}_{km}$ is the $(N_R \times 1)$ vector of those signal at APm intended for the UEk. Here, we assume $\|\mathbf{V}_{km}\|^2 = N_R$. Then the $(N_R \times 1)$ received signal vector at UEi:

$$\mathbf{y}_i = \sum_{m=1}^{M} \mathbf{H}_{im} \sum_{k=1}^{K} \mathbf{V}_{km}\mathbf{s}_{km} + \mathbf{z}_i = \sum_{m=1}^{M}\sum_{k=1}^{K} \exp\left(-i\vec{\omega}_{im}\right)\sqrt{\beta_{im}}\boldsymbol{\psi}_T^H\left(\theta_{im}\right)\mathbf{V}_{km}\mathbf{s}_{km} + \mathbf{z}_i \tag{5.4}$$

We suppose that each column of the pre-coding vector $\mathbf{V}_{km}$ steers a beam in the direction of UEk, but is phase shifted to compensate for the different phase shifts of the channel i.e. $\mathbf{V}_{km} = \boldsymbol{\psi}_T\left(\theta_{km}\right)\exp\left(i\vec{\omega}_{km}\right)^T$.

Then:

$$\mathbf{y}_i = \sum_{m=1}^{M}\sum_{k=1}^{K} \sqrt{\beta_{im}}\exp\left(-i\vec{\omega}_{im}\right)\boldsymbol{\psi}_T^H\left(\theta_{im}\right)\boldsymbol{\psi}_T\left(\theta_{km}\right)\exp\left(i\vec{\omega}_{km}\right)^T\mathbf{s}_{km} + \mathbf{z}_i \tag{5.5}$$

Then we write the normalized correlation between the steering vectors from APm, UEi and UEk, $\boldsymbol{\psi}_T^H\left(\theta_{im}\right)\boldsymbol{\psi}_T\left(\theta_{km}\right)$ as $\rho_{ik,m}$, with $\rho_{ii,m} = 1$. Then we can write:

$$\mathbf{y}_i = \sum_{m=1}^{M}\sum_{k=1}^{K} \sqrt{\beta_{im}}\rho_{ik,m}\exp\left(-i\vec{\omega}_{im}\right)\exp\left(i\vec{\omega}_{km}\right)^T\mathbf{s}_{km} + \mathbf{z}_i \tag{5.6}$$

Now the $\vec{\omega}_{im}$ and $\vec{\omega}_{km}$ can be written as:

$$\vec{\omega}_{im} = \omega_{im} + \begin{bmatrix} 0 \\ \vdots \\ n\omega_{d,im} \\ \vdots \\ N_R\omega_{d,im} \end{bmatrix};\ \vec{\omega}_{km} = \omega_{km} + \begin{bmatrix} 0 \\ \vdots \\ n\omega_{d,km} \\ \vdots \\ N_R\omega_{d,km} \end{bmatrix} \tag{5.7}$$

where $\omega_{d,im}$ is the difference between the received phase between two adjacent elements (referred to as A and B in Fig. 5.2) of the receive antenna array at UEi (as mentioned earlier the UEs are assumed to be linear arrays) from APm. Fig. 5.2 shows the geometry for calculating the phase difference. If the broadside of this array has an angle $\phi_{A,im}$ with the direction of APm, and element spacing l_i, then:

$$\omega_{d,im} = \frac{2\pi l_i}{\lambda} \sin \phi_{A,im} \tag{5.8}$$

If the element spacing l_i is $\frac{\lambda}{2}$ then $\omega_{d,im} = \pi \sin \phi_{A,im}$.

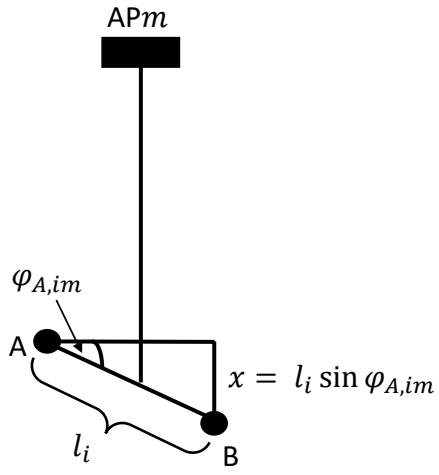

Fig. 5.2 Schematic for determining the phase difference between two adjacent elements of UE antennas

Now:

$$\begin{aligned}
\Upsilon_{ik,m} &= \exp(-i\vec{\omega}_{im}) \exp(i\vec{\omega}_{km})^T \\
&= \exp(i(\omega_{km} - \omega_{im})) \\
&\times \begin{bmatrix}
1 & \cdots & \exp\left(n' i\omega_{d,km}\right) & \cdots & \exp\left(N_R i\omega_{d,km}\right) \\
\vdots & & \vdots & & \vdots \\
\exp\left(-ni\omega_{d,im}\right) & \cdots & \exp\left(n' i\omega_{d,km} - ni\omega_{d,im}\right) & \cdots & \exp\left(N_R i\omega_{d,km} - ni\omega_{d,im}\right) \\
\vdots & & \vdots & & \vdots \\
\exp\left(N_R i\omega_{d,im}\right) & \cdots & \exp\left(n' i\omega_{d,km} - N_R i\omega_{d,im}\right) & \cdots & \exp\left(N_R i\omega_{d,km} - N_R i\omega_{d,im}\right)
\end{bmatrix}
\end{aligned} \tag{5.9}$$

Then equation 5.6 becomes:

$$\mathbf{y}_i = \sum_{m=1}^{M} \sum_{k=1}^{K} \sqrt{\beta_{im}} \rho_{ik,m} \Upsilon_{ik,m} \mathbf{s}_{km} + \mathbf{z}_i = \mathbf{H}_i \mathbf{s} + \mathbf{z}_i \tag{5.10}$$

From equation 5.10,

$$
\begin{aligned}
\mathbf{H}_i &= [\mathbf{H}_{1,i} \cdots \mathbf{H}_{m,i} \cdots \mathbf{H}_{M,i}] \\
\mathbf{H}_{m,i} &= \left[\mathbf{H}_{m,i1} \cdots \mathbf{H}_{m,ik} \cdots \mathbf{H}_{m,iK}\right] \\
\mathbf{H}_{m,ik} &= \sqrt{\beta_{im}}\rho_{ik,m}\Upsilon_{ik,m} \\
\mathbf{s} &= \begin{bmatrix} \mathbf{s}'_1 \\ \vdots \\ \mathbf{s}'_M \end{bmatrix} \text{ with } \mathbf{s}'_m = \begin{bmatrix} \mathbf{s}_{1m} \\ \vdots \\ \mathbf{s}_{Km} \end{bmatrix} \\
m &= 1 \cdots M
\end{aligned}
$$

5.2.1 ZF Pre-coding

Now, we may stack the vectors $\mathbf{y}_1 \ldots \mathbf{y}_K$ to form a single length $K \times N_R$ column vector, and write as:

$$
\mathbf{y} = \begin{bmatrix} \mathbf{y}_1 \\ \vdots \\ \mathbf{y}_i \\ \vdots \\ \mathbf{y}_K \end{bmatrix} = \begin{bmatrix} \mathbf{H}_1 \\ \vdots \\ \mathbf{H}_i \\ \vdots \\ \mathbf{H}_K \end{bmatrix} \mathbf{s} + \begin{bmatrix} \mathbf{z}_1 \\ \vdots \\ \mathbf{z}_i \\ \vdots \\ \mathbf{z}_K \end{bmatrix} = \mathbf{H}\mathbf{s} + \mathbf{z} \tag{5.11}
$$

We further apply a global pre-coding matrix $\mathbf{V}$ at a central processing unit (CPU), whose outputs are the set of signals input to the precoders at the APs, forming the vector $\mathbf{s}$, i.e.:

$$
\mathbf{s} = \mathbf{V}\mathbf{s}' \tag{5.12}
$$

where $\mathbf{s}'$ is the vector of the data symbols to be transmitted to user 1 to K. Applying the zero-forcing:

$$
\mathbf{V} = \mathbf{H}^H \left(\mathbf{H}\mathbf{H}^H\right)^{-1} \tag{5.13}
$$

5.2.2 ZF Pre-coding with Eigenvalue Decomposition

In this proposed approach only one data stream is sent to each UE, where the N_R antenna signals are combined using a weight vector derived from the receive-end eigenvector of the strongest eigenmode.

We can determine optimum combining weight vectors at UEi by performing an eigenvalue decomposition of:

$$\mathbf{H}_i\mathbf{H}_i^H = \sum_{m=1}^{M}\sum_{k=1}^{K}\mathbf{H}_{m,ik}\mathbf{H}_{m,ik}^H = \sum_{m=1}^{M}\beta_{im}\sum_{k=1}^{K}|\rho_{ik,m}|^2\Upsilon_{ik,m}\Upsilon_{ik,m}^H \tag{5.14}$$

Now:

$$\Upsilon_{ik,m}\Upsilon_{ik,m}^H = \exp(-i\vec{\omega}_{im})\exp(i\vec{\omega}_{km})^T\exp(-i\vec{\omega}_{km})\exp(i\vec{\omega}_{im})^T = N_R\Phi_{im}$$

where, the $(n,n')^{th}$ element will have $\Phi_{im}(n,n') = \exp\left(i\omega_{d,im}(n-n')\right)$. Then equation 5.14 becomes:

$$\mathbf{H}_i\mathbf{H}_i^H = N_R\sum_{m=1}^{M}\beta_{im}\Phi_{im}\sum_{k=1}^{K}|\rho_{ik,m}|^2 \tag{5.15}$$

The optimum combining weight vector $\mathbf{u}_i$ at this UE is the eigenvector corresponding to the largest eigenvalue of $\mathbf{H}_i\mathbf{H}_i^H$. The combined received signal r_i at UEi is then:

$$r_i = \mathbf{u}_i^H\mathbf{y}_i = \mathbf{u}_i^H\mathbf{H}_i\mathbf{s} + \mathbf{u}_i^H\mathbf{z}_i \tag{5.16}$$

We then form a vector $\mathbf{r}$ by concatenating these outputs across all UEs by

$$\mathbf{r} = \begin{bmatrix}\mathbf{u}_1^H\mathbf{H}_1\\ \vdots\\ \mathbf{u}_i^H\mathbf{H}_i\\ \vdots\\ \mathbf{u}_K^H\mathbf{H}_K\end{bmatrix}\mathbf{s} + \begin{bmatrix}\mathbf{u}_1^H\mathbf{z}_1\\ \vdots\\ \mathbf{u}_i^H\mathbf{z}_i\\ \vdots\\ \mathbf{u}_K^H\mathbf{z}_K\end{bmatrix} = \grave{\mathbf{H}}\mathbf{s} + \grave{\mathbf{z}} \tag{5.17}$$

We then use a precoder $\overline{\mathbf{V}}$ at the CPU:

$$\overline{\mathbf{V}} = \grave{\mathbf{H}}^H\left(\grave{\mathbf{H}}\grave{\mathbf{H}}^H\right)^{-1} \tag{5.18}$$

where the dimension of $\grave{\mathbf{H}}$ is $N_R \times (N_R \times K \times M)$.

5.3 Results and Discussion

The performance of the proposed schemes is investigated through MATLAB simulations using the scenario described in Section 5.2 and illustrated in Fig. 5.1. We have deployed the distributed approach utilizing four directional APs with different configurations while the multi-antenna UEs are randomly distributed throughout the coverage area. The total transmit

power per AP is decreased to 17dBm for this chapter. This is due to the resultant high SNR values from using multi-antenna UEs. We obtained the user throughput by a truncated form of the Shannon bound defined in 3GPP standards [173] and for the downlink, the expected SNR ranges from -10dB to 30dB. The noise figure at the receivers is 10dB in a bandwidth of 1.5 GHz and the carrier frequency is 26 GHz.

In this section, the results exhibit the performance of the MU-MaMIMO system where multiple antenna arrays are used at both transmitter and receiver sides. We study the ZF pre-coding technique for multi-antenna UEs and compare its user throughput with the approach of Section 5.2.2, including EVD along with ZF pre-coding. Furthermore, we demonstrate the performance differences between the single antenna and multi-antenna UEs. With these proposed methodologies, observations have been made to determine the number of users to be served by distributed APs with various arrangements.

Figure 5.3 presents the 10th percentile of the throughput per UE for a MU D-MaMIMO system using multi-antenna UEs served by 4 APs with different array arrangements. We assumed that each UE is equipped with 2 elements with random broadside direction. The throughput per UE is calculated by the attenuated and truncated form of the Shannon bound used in Chapter 4. The formula is given by equation 4.30 where the minimum SNR is -10dB and the maximum SNR is 30dB for the downlink. We have applied only the ZF pre-coding between the users and the elements. It is seen that at the 10th percentile the throughputs per UE for a single user is almost 9 bps/Hz for 10×10, 25×4, and 50×2 arrays due to the array gain from having the same total number of elements per AP but configured differently. However, at 5 or more random users, the average throughput per UE of 10×10 array arrangement begin to fall drastically and the throughput goes to zero for only 20 users. As mentioned earlier we assume that the minimum SNR of the code set is -10dB based on QPSK and 1/8 rate (downlink), hence the minimum acceptable average throughput per UE is 0.083 bps/Hz. So we can say that for 10×10 distributed APs, up to 20 users could be served such that they all achieve at least this minimum throughput at least 90% of the time. Now if we consider the same total number of antenna elements at the transmitting end and change the array configuration, i.e. increase the horizontal antenna elements and reduce in the vertical direction, a larger number of users can be served. Using 25×4 arrays, we can increase the number of users to 40 and with further increase of antenna elements in the x-plane, 50×2 distributed arrays can serve up to 60 users effectively. However, the beamwidth in the azimuth direction of 50×2 arrays are narrower than 10×10 and 25×4 arrays. The beamwidths of 10×10, 25×4 and 50×2 arrays are about 10°, 4° and 2° respectively. The correlation between the channels reduces significantly for 50×2 distributed arrays. For

15×15 and 20×20 arrays, the throughput per UE is higher due to the increased number of antenna elements per UE as well as the path gain. We can observe that 15×15 arrays can serve up to 30 users, and using 20×20 arrays, the number of users to be served is up to 50.

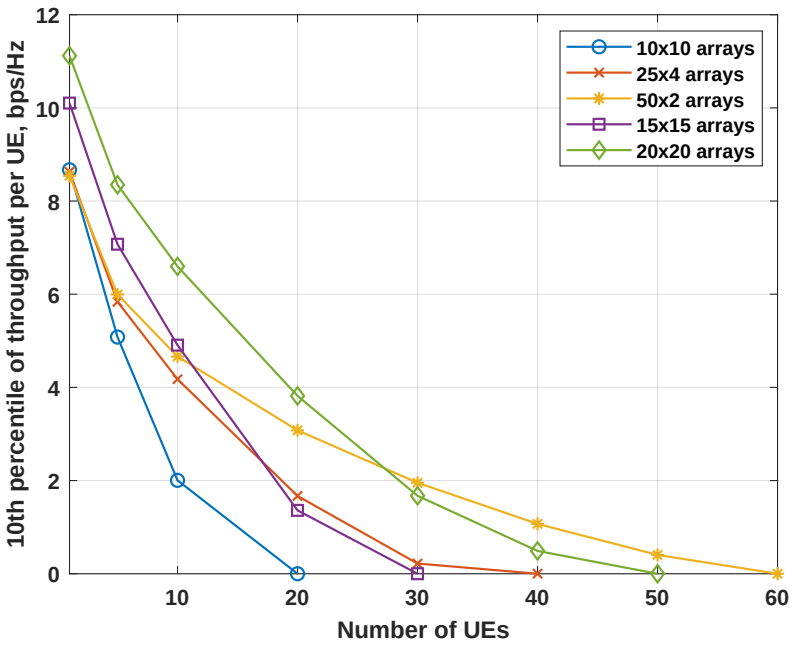

Fig. 5.3 Average throughput per UE for multi-antenna user scenario using ZF pre-coding for different AP arrangements (Number of antenna elements at each UE = 2)

Figure 5.4 is obtained by using the proposed EVD-based ZF pre-coding scheme on a MU D-MaMIMO system as described above. The overall performance is significantly improved compared to using only the ZF pre-coding, except for very small numbers of users. However, the pattern of the graph remains very similar to the previous plot: for a lower number of UEs the 10th percentile throughputs for 10×10, 25×4, and 50×2 arrays are almost identical, and for a single UE the throughput per UE is around 6 bps/Hz at 10th percentile. As the number of users increases the 50×2 arrays outperforms the other two arrangements. These distributed arrays can serve up to 50, 90, and 160 users respectively. 15×15 and 20×20 arrays can provide coverage for up to 90 and 160 users. Interestingly 20×20 and 50×2 arrays both provide service for around up to 150 users at the 10th percentile.

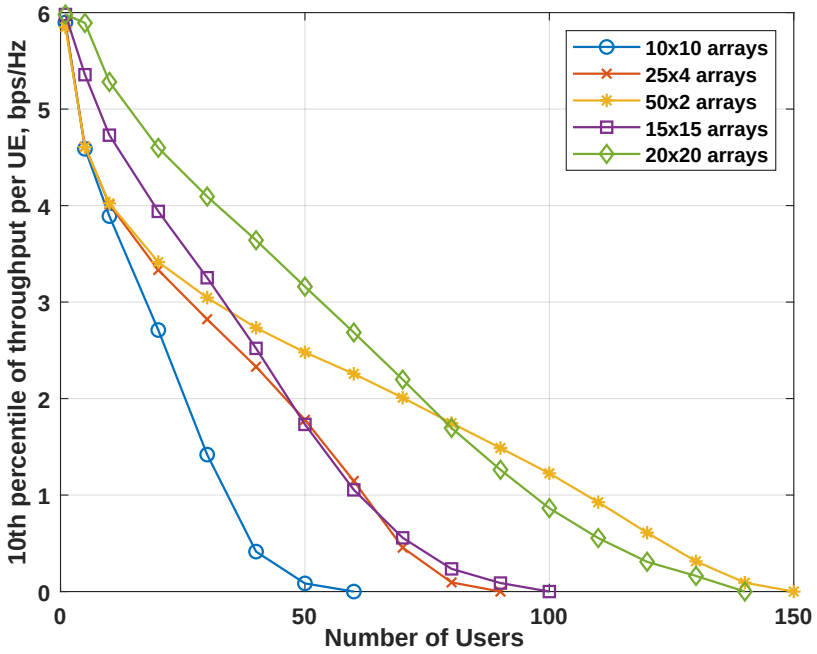

Fig. 5.4 Average throughput per UE for multi-antenna user scenario using EVD based ZF pre-coding for different AP arrangements (Number of antenna elements at each UE = 2)

In Fig. 5.5, a comparison has been made between a single antenna UE case and a multi-antenna case using the ZF pre-coding and the proposed EVD-based ZF pre-coding schemes. It is observed that using only the ZF pre-coding for multi-antenna UE scenarios seems to perform well for a very limited number of users regardless of the array arrangements. However, the throughput per UE is higher compared to the other two curves as multiple data streams are sent to the UEs. In the 20×20 array system, a single UE can experience almost double the throughput of the single antenna UE and that is around 11 bps/Hz. Furthermore, it is evident that only a small number of users can be served in this scenario with higher throughput. Even 20×20 arrays using ZF can serve only the same number of users as the 10×10 arrays for single antenna UEs i.e. 50. It also can be said from Fig. 5.5 that the 10×10 array distribution does not prove to be sufficient in providing good service to a system with large number of users compared to other array arrangements using any of the approaches discussed above. As we have seen in Chapter 2, ZF performs well when the number of UE is much smaller than the number of transmitting antennas. Here we can observe that in the 20×20 array distribution where the total number of antenna elements is 4 times greater than in the 10×10 array distribution, the number of users served is almost twice that using single antenna UE with ZF pre-coding. Therefore it can be said that the 20×20 array distribution

can provide coverage for a number of single antenna users (around 150) which is around 10% of the total number of AP elements (i.e. 1600) using ZF pre-coding. On the other hand, using 50×2 arrays with many fewer antenna elements in total is beneficial as they can provide coverage for the same number of users by applying the proposed EVD-based ZF approach for multi-antenna UE cases i.e. selecting the the strongest eigenvector, and it saves processing power. The 50×2 arrays serve a number of users which is nearly 40% of the total number of antennas. For a lower number of UEs, the throughput per UE is higher for the 20×20 arrays than for other antenna distributions. The average throughput for 40 users is roughly 1 bps/Hz higher for 20×20 array distribution compared to the 50×2 array distribution, but as the number of users grows, the gap becomes less, and beyond 80 users, the 50×2 array distribution outperforms the 20×20 array case marginally.

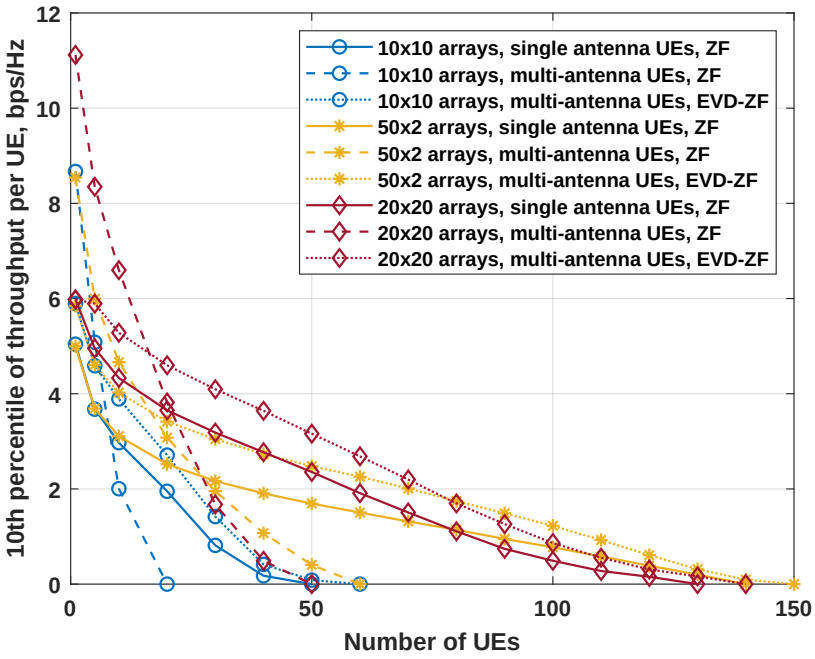

Fig. 5.5 Average throughput per UE for multi-antenna user scenario using difference approaches for different AP arrangements (Number of antenna elements at each UE = 2)

Figure 5.6 presents the average total throughput versus the number of users for different arrangements of APs by applying EVD-based ZF pre-coding . We assume the number of antenna elements per UE is 2. This graph shows the average total throughput of the users for a given array configuration. It is evident that 20×20 distributed arrays can provide much higher overall throughput i.e. the average total throughput is about 180 bps/Hz, than that of any other AP arrangements. However, the highest peak is seen for 60 users, and as the

interference rises, the curve begins to fall and goes down to zero for 180 users. So it can be said that for this AP arrangement, 60 users can be accommodated utilising maximum system capacity and beyond 60 users the interference becomes as issue as ZF can not completely eliminate the inter-user interference. On the other hand for 50×2 array distribution the maximum average total throughput is about only about 12% less. For 90 or more users the total throughput with 50×2 arrays is greater than for 20×20 arrays, showing that the former is less affected by interference as the beamwidths of the 50×2 arrays are narrower than the 20×20 arrays. Other AP arrangements have shown lower overall throughput serving smaller numbers of users.

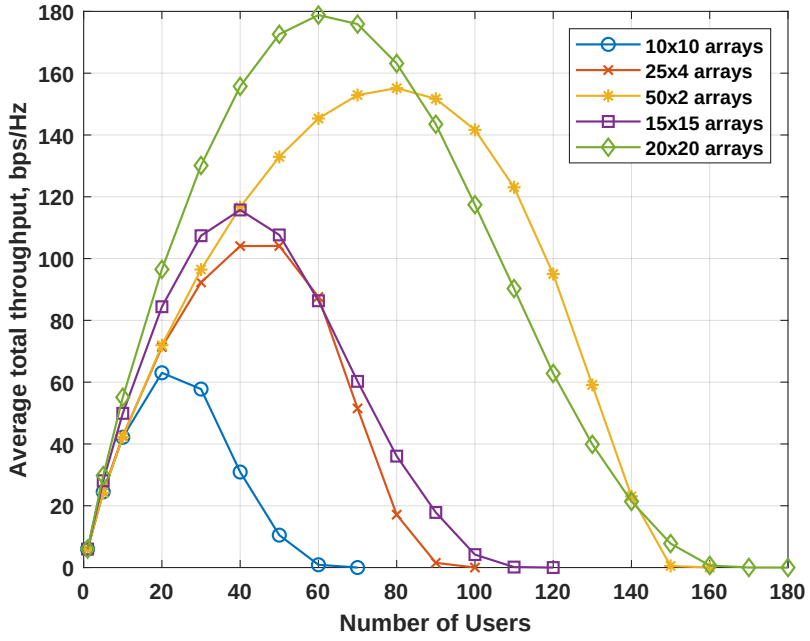

Fig. 5.6 Average total throughput for multi-antenna user scenario using EVD based ZF pre-coding for different AP arrangements (Number of antenna elements at each UE = 2)

In the sequel, we show the CDF of the SNR for different numbers of antenna elements per UE for a) 50×2 b) 20×20 array distribution. From Fig. 5.6 we have observed that the maximum throughput is achieved for 80 users in the coverage area for 50×2 arrays. So in Fig. 5.7a we choose 60 users to served by the same antenna arrangements and increased the number of elements per UE. We have discussed that it is feasible to deploy multiple antennas at the UEs depending on the size and shape of the device. It is seen that at the bottom 10% percent, it is certainly beneficial to increase the number of antenna elements from 2 to 4 as it improves the SNR by around 3dB. However, from 2 to 10 elements the improvement is less

significant. On the other hand on the top end, the spread of the distribution of SNR increases though it is not very advantageous to increase the elements at the UE up to 10. Moreover, for 20×20 array distribution, it is possible to accommodate 60 users with maximum capacity (Fig. 5.6). Fig. 5.7b shows the CDF where 60 users are served. At the 10th percentile, the increase in SNR with increasing number of elements per UE is better compare to the 50×2 array. Similarly the increase in SNR with increasing number of elements at the UE decreases. Therefore, increasing the number of antenna elements per UE is useful to some degree using this EVD-based ZF.

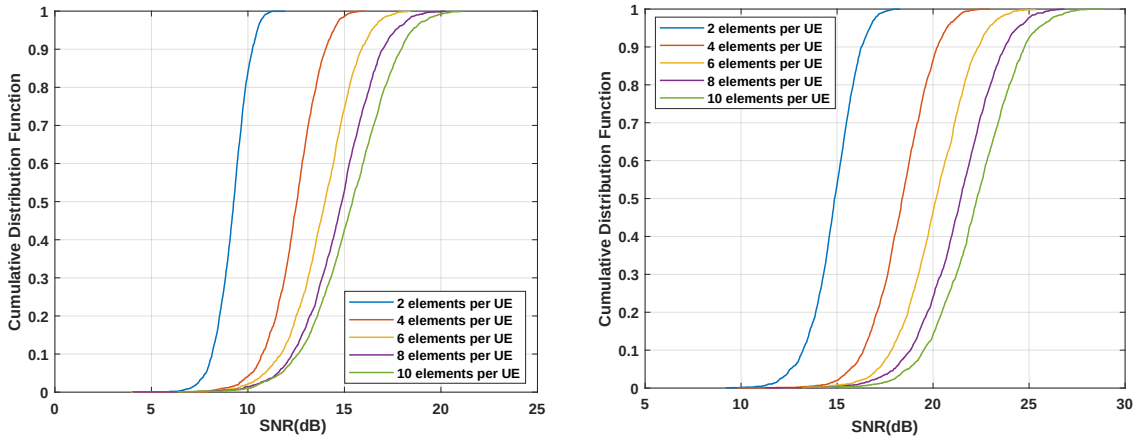

Fig. 5.7 The CDF of different number of antenna elements per UE a) 50×2, b) 20×20 antenna arrays

Fig. 5.8 presents the 10th percentile of the SNR plotted against the number of UEs utilizing different numbers of antenna elements per UE. It is more clear from this figure that for a small number of users it is beneficial to increase the number of elements at the UEs. For 40 UEs and the 50×2 arrays the SNR improves by around 3dB when the number of UE antennas increases from 2 to 4, but by a about 2dB with a further increase to 4 antennas, and only by a further 1dB for the increase to 8 antennas (Fig. 5.8a). Since -10dB is the minimum SNR of the code set, the received SNR allows 140 users in the area for the 50×2 arrays, with 2 UE antennas. Increasing the number of antenna elements to 8 at the UE will only serve a few more users. Similarly it is also observed for the 20×20 array, that the improvement in the SNR with an increasing number of UE antenna elements becomes less significant. However, for a small number of users, the increase in SNR for increasing antenna elements is better for 20×20 compared to the 50×2 array distribution. However for higher number

of users the increase in SNR is around 5dB when the number of UE antennas increases from 2 to 8.

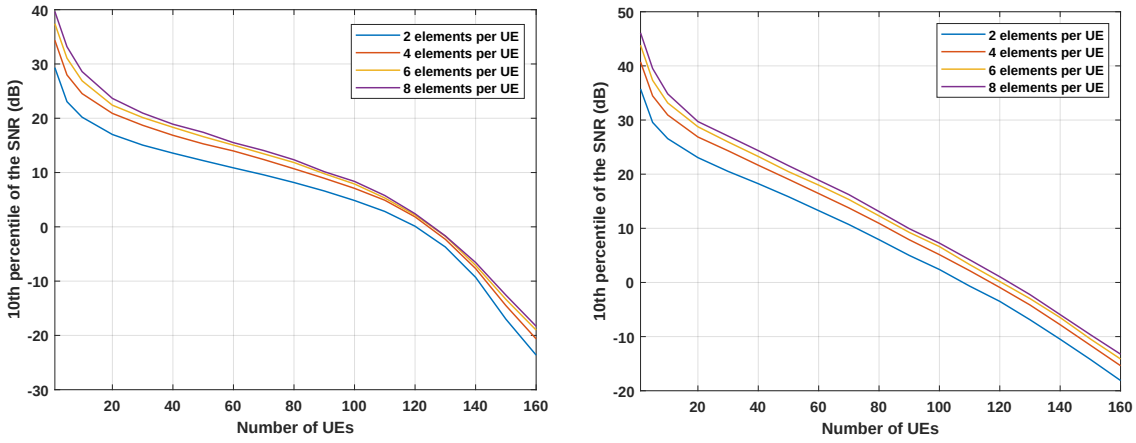

Fig. 5.8 10th percentile of SNR against increasing number of UEs for different number of antenna elements a) 50×2, b) 20×20 array distribution

5.4 Summary

In this chapter, we have described the performance of a D-MaMIMO system deploying multi-antenna users. We have particularly investigated the system performance using ZF pre-coding and EVD-based ZF in an LoS scenario in mmWave communication. We have seen that applying only ZF pre-coding between the UEs and their sub-channels to the elements on the UEs improves the throughput but serves a smaller number of users. However, our proposed EVD-based ZF improves the system performance with acceptable throughput serving a larger number of users. We have made a comparison between single antenna UE and multi-antenna UE scenarios and it is observed that using EVD-based ZF significantly enhances the number of users to be served effectively due the diversity of the multi-antenna UEs, if the number of data streams is reduced to one. In addition, if we increase the number of antenna elements per UE then the throughput improves further and hence additional antenna elements are beneficial for the mmWave D-MaMIMO system. It is, however, only useful to add a few extra antennas at the UE. The number of antenna elements to be deployed at the UEs should be entirely dependent on the device architecture. Moreover, by increasing the elements at UEs, the transmitting power per AP can be reduced maintaining the required throughput. We

can also conclude from this study that the benefits of ZF pre-coding becomes limited with increasing numbers of users.

Chapter 6

Impact of K-factor in mmWave Transmission

6.1 Introduction

The increased path-loss in millimetre wave (mmWave) can be compensated by directional antennas by increasing the gain in the desired direction. Hence, mmWave frequencies such as 60 GHz, primarily depend on line-of-sight (LoS) links between APs and UEs because of the high path-loss and poor penetration. However, the LoS can experience blockage from even human presence as well as other environmental objects. It is seen that at 60 GHz, the received signal strength can be attenuated by around 20dB from a human shadowing between the direct links [179]. Moreover, reflections, diffractions and scattering from different obstacles in the system may result in viable non-LoS (NLoS) links with acceptable data rates. For mmWave cellular systems, these rich scattering multipath provide both possibilities and constraints. Stable NLoS paths can present feasible alternatives to LoS paths, allowing for better link efficiency or higher redundancy. Nonetheless, the additional interference from these multipath should be addressed for better network performance [180]. It is observed that the propagation nature of mmWave NLoS paths differs from lower frequencies. Due to the weak diffraction at mmWave, the NLoS links are dominated by reflections and scattering. Because of the energy losses from scattering, mmWave NLoS paths suffer significantly more attenuation than sub-6GHz NLoS paths. In addition, the penetration losses differ from indoor to outdoor scenarios and are higher in mmWave. It is not feasible to employ the same base stations for indoor and outdoor environments. Furthermore, in the angular domain, mmWave channels are sparse containing clusters, including additional scattering paths along with the LoS path [181]. A multipath cluster is a collection of rays that may be distinguished from one

another and share common properties such as time and spatial domain characteristics. In the mmWave radio channel the impulse response is formed by the aggregate of individual MPCs inside all clusters. Suppose for N_t transmit and N_r receive antennas, the channel matrix of clusters and rays for a MIMO system can be defined as

$$H(t) = \sum_{n_{cl}}^{N_{cl}} \sum_{p}^{N_p} H_{n_{cl},p}(t)$$

where N_{cl} is the total number of clusters consisting of N_p rays within each cluster and $H_{n_{cl},p}(t)$ is a channel contribution of the p^{th} ray in the n_{cl}^{th} cluster at time instant t.

As a result, in order to characterise the channel impulse response, it is necessary to distinguish the parameters of each cluster [22]. Several works have been performed considering Rayleigh and Ricean fading channel. Because of the short links between APs and UEs, the LoS path is frequently dominant over multipath signals in the mmWave channel. It is seen that the performance of the MIMO channel is affected by the Ricean K-factor [182]. The Ricean K-factor is the ratio of signal power in the dominant path to that in the scattered and reflected paths and is an important channel parameter in mmWave communication [183]. [184] considers the scattering in a NLoS environment for an indoor mmWave communication system. It presents measurement results showing that at mmWave the Ricean distribution is a better fit than Rayleigh, and that the K-factor increases with antenna directivity and bandwidth. [164] presents channel models for mmWave frequencies. However, mmWave AP antennas have narrow beamwidth, and only scatterers close to the line of sight direction to the user will be illuminated. Hence, it is unnecessary to consider scatterers far from the user terminal in terms of angle. Motivated by importance of addressing the K-factor for Ricean fading mmWave channel, this chapter introduces the concepts of the ***Environmental*** and the ***Effective*** K-factor, and derives a closed form expression to show the impact of antenna array gain and scatterer distribution on the effective K-factor of a Ricean channel. For this purpose, we use a ring of scatterers model [185] based on scatterers at a defined distance from the user. This has been widely used at sub-6 GHz frequencies. It allows the radius to be varied to simulate different angular spreads. We exploit antenna arrays to perform explicit beamforming, directing a beam towards each user, which means that the illumination of the scatterers, and hence the scattered power, depends on the beam-width of the array.

6.2 System and Channel Model

The ring of scatterers model is a purely geometry-based scattering model where the users are surrounded by multiple local scatterers on the circumference of a ring of a given radius, as shown in Fig. 6.1. The principles of multipath scattering and reflection generally also apply at mmWaves and it is also expected that multipaths arrive at an AP in a cluster subtending a small angle around the LoS component (which we assume to be always present). The model is sufficiently flexible to vary the proportion of scattered power relative to the main line of sight path, and hence can also simulate a range of K-factors.

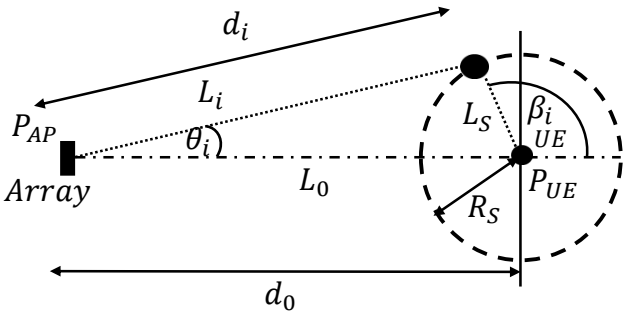

Fig. 6.1 One ring scattering model for single user and transmitting antenna array for one scattering scenario (plan view)

In this model, we position one directional antenna array with $N_h \times N_v$ elements serving a single user equipment (UE) with a single antenna element at same height. A ring of R_s radius is considered around the UE at a distance L_0 from the antenna array where N_s scatterers are assumed to be distributed randomly around the ring shown as a thin dashed solid line (Fig.6.1). The i^{th}multipath is assumed to experience a path loss L_i, given by the inverse square law, on the path between the transmitting array and the scatterer. All paths from scatterers to a user to have the same scattering loss L_s as the scatters are positioned on the circumference of the ring that we assumed. The L_s is the ratio of power that finally arrives at the UE to power that arrives at the scatterer, because most of the power that arrives at the scatterer is scattered in all directions, with only a small proportion going to the direction of the UE. Hence, the resulting multipath signals combine incoherently, resulting in Ricean fading. The propagation model follows the inverse square law of the Friis path loss equation. The received power, $P_{UE,m}$ from the m^{th} AP is given by equation 3.1 and the antenna gain is given by the equation 3.7. The carrier frequency is considered 26 GHz similar as in earlier chapters. We ignore atmospheric and other losses due to the short distance between the AP and the UE.

6.3 Environmental and Effective Ricean K-factor

Based on the antenna directionality we define *effective* K-factor, distinct from the *environmental* K-factor. The concepts are illustrated in Fig. 6.2.

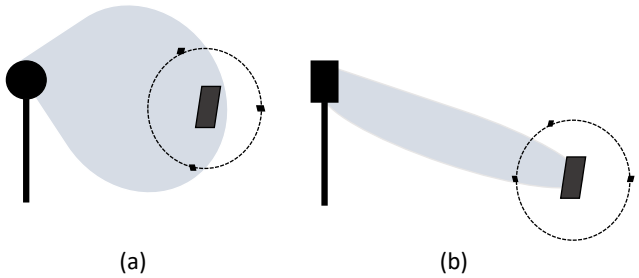

Fig. 6.2 Concepts of (a) environmental K-factor and (b) effective K-factor

6.3.1 Environmental Ricean K-factor

For a given scenario if the UE and the AP are both equipped with omni-directional single antennas placed at a specific distance d_0 then the K-factor is environmental. From Fig.6.1, where a single AP antenna is transmitting towards the UE, and suppose the UE is surrounded by N_s scatterers, then the environmental K-factor (K_{env}) is the ratio of the power in LoS path, P_0 to the power in the multipath, $P_{s,env,i}$. The environmental K-factor is then given by

$$K_{env} = \frac{P_{LoS}}{P_{NLoS}} = \frac{\frac{P_{AP}G_{AP}G_{UE}}{L_0}}{\frac{P_{AP}G_{UE}}{L_s}\sum_{i=1}^{N_s}\frac{G_{APi}}{L_i}}$$

As both the AP and UE are omnidirectional $G_{AP} = G_{UE} = 1$.

$$K_{env} = \frac{1}{\frac{L_0}{L_s}\sum_{i=1}^{N_s}\frac{1}{L_i}} \approx \frac{L_s}{N_s} \tag{6.1}$$

The approximation applies if $d_0 \gg R_s$, and hence $L_i \approx L_0, \forall i$

6.3.2 Effective Ricean K-factor

On the other hand, the *effective* K-factor takes into account the gain of the AP antenna array in the direction of the UE and each multipath. Hence, it depends on the antenna gain of the AP and the path loss. For calculating the *effective* K-factor we need to multiply the power on the i^{th} multipath by the transmit antenna gain $G_{AP}(\theta_i)$, and on the LoS by $G_{AP}(0)$, as $\theta = 0$ in the LoS path. Assuming that the distribution of each scatterer location is uniform

around the ring of scatterers, i.e. $p(\beta) = \frac{1}{2\pi}$, then average received scattered power from each scatterer is

$$P_{s,eff,i} = \int_{-\pi}^{\pi} \frac{P_{AP}G_{AP}(\theta_i)}{L_i L_s} \left(\frac{1}{2\pi}\right) d\beta \tag{6.2}$$

Then effective K-factor (K_{eff}) becomes

$$\begin{aligned} K_{eff} &= \frac{P_0}{\sum_{i=1}^{N_s} P_{s,eff,i}} = \frac{\frac{P_{AP}G_{AP}(0)}{L_0}}{N_s P_{s,eff,i}} \\ &= \frac{\frac{P_{AP}G_{AP}(0)}{L_0}}{N_s \int_{-\pi}^{\pi} \frac{P_{AP}G_{AP}(\theta_i)}{L_i L_s} (\frac{1}{2\pi}) d\beta} \\ &= \frac{N_s}{2\pi L_s} \int_{-\pi}^{\pi} \frac{L_0 G_{AP}(\theta_i)}{L_i G_{AP}(0)} d\beta \end{aligned} \tag{6.3}$$

Now both θ_i and L_i are in principle the functions of β, so we can write

$$d_i \sin(\theta_i) = R_s \sin(\beta_i) \tag{6.4}$$

and, using the cosine rule,

$$d_i^2 = d_0^2 + R_s^2 + 2d_0 R_s \cos(\beta_i) \tag{6.5}$$

So that

$$\theta_i = \arcsin\left(\frac{R_s \sin(\beta_i)}{\sqrt{d_0^2 + R_s^2 + 2d_0 R_s \cos(\beta_i)}}\right) \tag{6.6}$$

Assuming inverse square path loss,

$$L_i \propto d_i^2 = d_0^2 + R_s^2 + 2d_0 R_s \cos(\beta_i) \tag{6.7}$$

and hence

$$\begin{aligned} \frac{L_i}{L_0} &= \frac{d_0^2 + R_s^2 + 2d_0 R_s \cos(\beta_i)}{d_0^2} \\ &= 1 + \left(\frac{R_s}{d_0}\right)^2 + \frac{2R_s}{d_0} \cos(\beta_i) \end{aligned} \tag{6.8}$$

Assuming arrays are $N_h \times N_v$: we can treat this as a horizontal array of vertical columns as the elevation angle is assumed to be 0 for all instance, each of which has gain N_v. Assume LoS beam is steered at an azimuth angle of α from the normal of the array. Then

$$\begin{aligned} G_{AP}(\theta_i) &\propto N_v \left| \sum_{m=1}^{N_h} \exp\left(j2\pi d_h(\sin(\alpha)-\sin(\alpha+\theta))\right)\right|^2 \\ &= C_0 N_v \left| \sum_{m=1}^{N_h} \exp(j2\pi d_h(\sin(\alpha)-\sin(\alpha+\theta)))\right|^2 \\ &= 4N_v \left(\sum_{m'=1}^{\frac{N_h}{2}} \cos((2m'-1)d_h\pi(\sin(\alpha)-\sin(\alpha+\theta)))\right)^2 \end{aligned} \tag{6.9}$$

where C_0 is a proportionality constant and d_h denotes the antenna element spacing divided by the wavelength. $G_{AP}(0) = C_0 N_v N_h$, and hence

$$\frac{G_{AP}(\theta_i)}{G_{AP}(0)} = \frac{4}{N_h}\left(\sum_{m'=1}^{\frac{N_h}{2}} \cos((2m'-1)d_h\pi(\sin(\alpha)-\sin(\alpha+\theta)))\right)^2 \tag{6.10}$$

Then

$$K_{eff} = \frac{d\phi}{\frac{2N_s}{\pi N_h L_s}\int_{-\pi}^{\pi} \frac{\left(\sum_{m'=1}^{\frac{N_h}{2}} \cos((2m'-1)d_h\pi(\sin(\alpha)-\sin(\alpha+\theta_i)))\right)^2}{1+\left(\frac{R_s}{d_0}\right)^2+\frac{2R_s}{d_0}\cos(\beta)}} \tag{6.11}$$

where

$$\theta_i = \arcsin\left(\frac{R_s\sin(\beta)}{\sqrt{d_0^2+R_s^2+2d_0R_s\cos(\beta)}}\right)$$

For the case when $d_0 \gg R_s$ a number of approximations are possible. We may approximate $G_{AP}(\theta)$ as a sinc function (arising from treating the array as a uniformly illuminated aperture of width $N_h d_v$), then,

$$G_{AP}(\theta) = N_v N_h \,\mathrm{sinc}(N_h d_h \pi(\mathrm{sinc}(\alpha)-\sin(\alpha+\theta)))^2 \tag{6.12}$$

This approximation is accurate in the main lobe and the first pair of side lobes of the directional response. Moreover if θ is small, $\sin(\alpha)-\sin(\alpha+\theta) = \sin(\alpha)(1-\cos(\theta)) - \sin(\theta)\cos(\alpha) \approx -\sin(\theta)\cos(\alpha)$. Also we can approximate $d_i \approx d_0$ and hence $\sin(\theta_i) \approx$

$\frac{R_s}{d_0}\sin(\theta_i)$. While it might seem logical to also make the approximation $L_i \approx L_0, \forall i$, this does in fact give rise to a more significant inaccuracy in the integrand. Then the final equation for effective K-factor is given by

$$\begin{aligned} K_{eff} &\approx \frac{1}{\frac{N_s}{2\pi}\int_{-\pi}^{\pi}\left(\frac{L_i}{L_0}\right)\mathrm{sinc}(N_h d_h \pi \cos(\alpha)\sin(\theta_i))d\beta} \\ &= \frac{2\pi}{N_s}\left(\int_{-\pi}^{\pi}\left(1+\left(\frac{R_s}{d_0}\right)^2+\frac{2R_s}{d_0}\cos(\beta_i)\,\mathrm{sinc}\left(\frac{N_h d_h R_s}{d_0}\pi\cos(\alpha)\sin(\beta)\right)^2\right)\right)^{-1} d\beta \\ &= \frac{\pi\Gamma d_0^2}{N_s(d_0^2+R_s^2)(J_1(2\pi\Gamma)(\pi^2\Gamma H_0(2\pi\Gamma)-1)-\pi\Gamma J_0(2\pi\Gamma)(\pi H_1(2\pi\Gamma)-2))} \end{aligned} \tag{6.13}$$

where $\Gamma = d_h N_h \cos(\alpha) R_s/d_0$, $J_k(z)$ denotes the Bessel function of the k^{th} kind, and $H_k(z)$ denotes the Struve H function [186]. Here, $\Gamma = d_h N_h \cos(\alpha)$ is the effective aperture of the array towards the LoS direction in the horizontal plane. Note that (6.13) depends primarily on the ratio of R_s/d_0.

6.4 Results and Discussion

In this section, we compare the simulation results with the analytical results for the effective K-factor. In the simulation environment, an AP with a given number of antenna elements is placed 100m from an UE equipped with a single antenna. The antenna element spacing is 0.5λ. There is a ring of scatterers assumed around the UE where the number of scatterers, N_s is 8 and the radius of the ring, R_s is varied. The total transmit power, P_{AP} is 33dB. The scattering loss, L_s is taken as 15dB. Thus the environmental K-factor, $K_{env} = \frac{L_s}{N_s} = \frac{31.6228}{8} = 3.95 \approx 6$dB.

The graphs show that the simulation results are close to the analytical approximation for K_{eff} for ring radius R_s up to 10m, for antenna arrays up to 10×10, which covers most cases of interest. In Fig. 6.3, the graph shows the values of environmental and effective K-factor with varying radius of the ring for different numbers of antenna elements. Here, we evaluated planar antenna arrays with 10×10,7×7 and 5×5 antenna elements. As the number of antenna elements decreases, the beam width increases and the values of effective K-factor approach the environmental K-factor. It can also be observed that the effective K-factor increases with increasing radius of the ring because the scattered power falling within the AP beamwidth decreases, while the LoS path loss remains the same. For the

10×10 array this effect can be very significant, increasing the K-factor by up to 6dB, which will also significantly improve the performance of a communication system of this link. The analytical values are close to the simulation results except for the case of 10×10 elements, since the approximation (6.13) is then less accurate. Hence for $R_s = 20$ and the 10×10 array the difference between the simulation and the analytical results is approximately 1dB, whereas for 7×7 and 5×5, the analytical results closely match the simulation results.

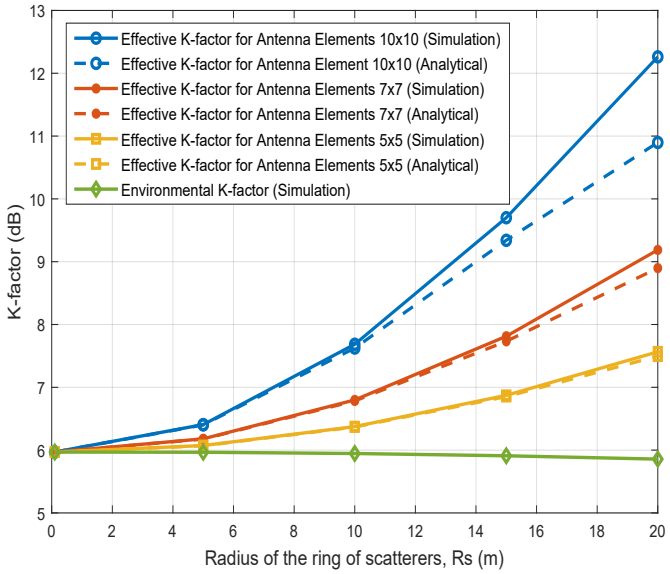

Fig. 6.3 Estimation of K-factor with varying radius of scatterer ring for different antenna array sizes

Figure 6.4 presents the evaluation of effective K-factors with varying radius for different values of azimuth angle, α. The trend of increasing K-factor with increasing radius is consistent but the K-factor decreases when the azimuth angle deviates from broadside angle. This is due to the increasing beamwidth and decreasing array gain with increasing azimuth angle. The analytical results follow the simulation results.

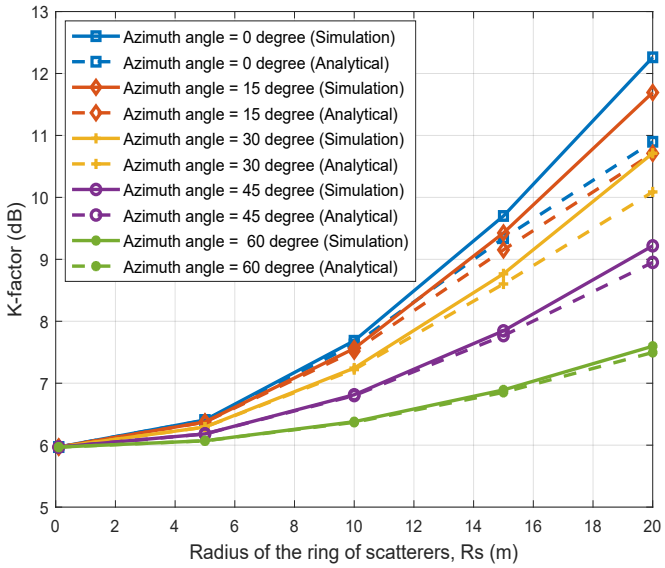

Fig. 6.4 Estimation of Effective K-factor with varying radius of scatterer ring for different values of azimuth angle α

In this scenario, one directional antenna is serving a user with a single omni-directional antenna. The AP and UE positions are fixed for each instance. The distance d is varied from 25m to 200m, considering the total area and the scattering radius, which are 200m and 20m respectively. The K-factors are estimated for APs with different element configuration. In Fig. 6.5, the average K-factor decreases when the UE is far from the AP, because all the scatterers are then equally illuminated, so that:

$$K_{factor} \rightarrow \frac{L_s}{N_s}$$

For a 10×10 antenna array, the change in the average K-factor is about 16dB, as the beam is very narrow, resulting in a reduced probability of the scatterer power falling into the beam. As a result, at least for small d, the multipath power is small compared to the power in the direct path. On the other hand, for the small antenna array cases (3×3 array and 2×2 array) the beam-width is wider, so the difference between LoS and multipath power is less. It is seen that for the 2×2 antenna array case the average K-factor is almost constant for distances from 50 to 200m, because the scatterers are fully illuminated over all this range.

Table 6.1 Array Distribution

Number of APs	**Array Size**
2	7×7
4	5×5
11	3×3
25	2×2

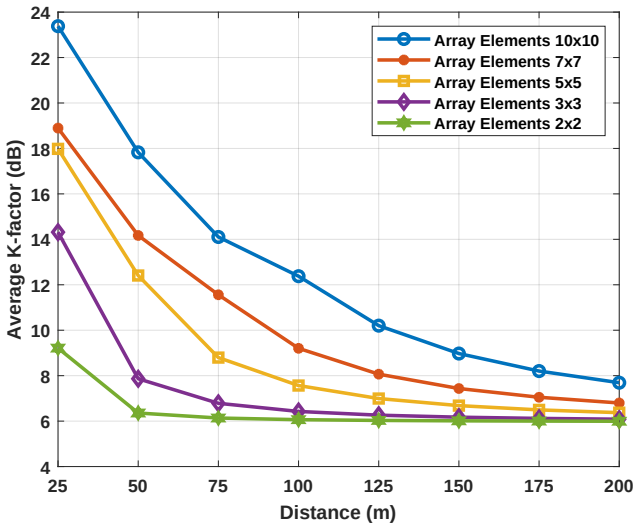

Fig. 6.5 Estimated average K-factor with distance for different antenna array size where L_S is 15dB

Figure 6.6 shows the received SNR at a single UE from APs with different distribution. The AP distribution is given in Table 6.1. The APs and UE are randomly distributed inside a $200m \times 200m$ square area.

It is seen that depending on the scattering loss, the powers coming from the multipath components contributes significantly for distributed antenna array systems in mmWave communication. The scattering loss, L_s affects the SNR values such that less scattering loss results in greater scattered powers at the user. In Fig. 6.6, the median SNR is observed with different scattering losses for different distributions of APs. The SNR decreases with increasing L_S. For 2 APs (7×7 array), the SNR drops almost 3dB as the L_s goes from 0dB to 15dB. Whereas for 25 APs (2×2 array), the SNR falls more than 6dB which is twice than the case for 2 APs.

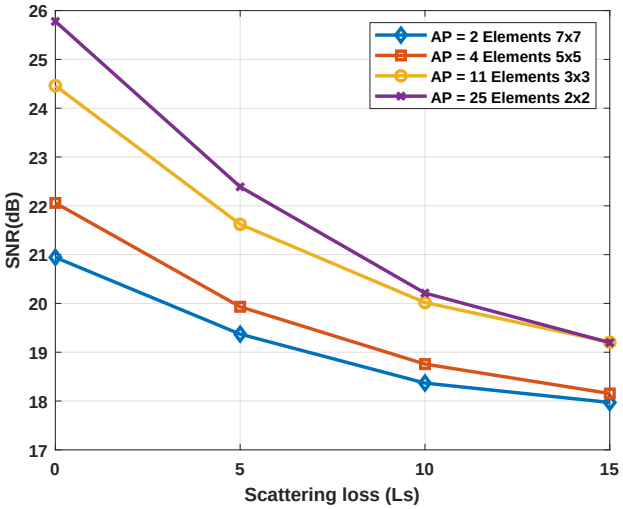

Fig. 6.6 The signal-to-noise ratio for different scattering loss and array size

6.5 Summary

In this chapter, we have introduced the concepts of *Environmental* and *Effective* K-factor considering the effect of a directional antenna on the K-factor of a Ricean channel for a one ring scattering multipath model in mmWave communication. This enables us to evaluate the effect of fading, assuming the presence of a line of sight and Ricean fading. The results show increasing effective K-factor with increasing radius of the ring of scatterers and antenna array size, resulting in a more “deterministic" propagation, with reduced probability of severe fading. It also emphasises the importance at mmWaves of narrow beam-widths from large arrays, and the importance of LoS paths. The simulation results compare with the derived analytical model for effective K-factor and the results are close to the simulation. It also shows that the average K-factor of the Ricean fading decreases with increasing AP and UE distance. Finally, we also note that on the assumption that the LoS signal strength is constant, performance improves with reducing scattering loss as the multipath powers contribute significantly to the total power.

Chapter 7

Conclusion and Future Work

7.1 Conclusions

According to the literature review presented in Chapter 2, wireless networks have already begun exploring millimetre wave (mmWave) bands in order to achieve the required data rate for uninterrupted transmission for the envisaged applications and services in 5G. Hence this thesis has addressed the pivotal engagement of mmWave in 5G communications. The enabling technologies such as distributed massive MIMO (D-MaMIMO) and beamforming (BF) have been investigated to mitigate the free space path loss and attenuation in mmWave propagation. It has seen that increasing the effect of multiple antenna array systems provides large throughput and fair coverage for multiple users. Furthermore, as we are moving closer to 6G technology, D-MaMIMO or cell-free (CF) MaMIMO has seen particularly well suited to support unplanned ultra-dense network (UDN) deployments by obviating the requirement for actual cells and allowing the network to adapt to the user distribution utilizing the array beams. It has been observed that a large number of directed beams with an appropriate pre-coding scheme have served dense users while enhancing system performance where the number of transmitting antennas are much higher than the number of users. In this thesis we have considered a square outdoor environment with multiple users where the access points (APs) and user equipments (UEs) the access points (APs) and user equipments (UEs) are not significantly different in height. In such scenarios in which the users are distributed horizontally, there is little benefit in 3D beamforming. This also implies that it is preferable to have the AP antenna arrays non-square in order to improve azimuth discrimination for these scenarios.

In Chapter 3, the benefits of 3D BF for the line-of-sight (LoS) mmWave propagation model have been considered by employing distributed antenna arrays. It is shown that

significant gains are available by distributing antenna elements over several smaller arrays through a large coverage area, rather than concentrating them in a centralised array. For the numerical results, we have considered an open square area and observed the SNR performance of single-user equipment (UE) for different arrangements of access points (APs). Uniform planar antenna arrays (UPAs) are considered for APs. We have divided the entire coverage area into grids to show the SNR in contour plots and reduce the computation time. These contour plots provide important design aspects for AP positions for distributed approach with a given broadside angle for a particular coverage area. It can be noted that the performance of distributed antenna system depends on the number of antenna arrays, array shape, their relative positions and broadside angles, and the structure of the coverage area. Although in this chapter we have chosen only the square area, this model can easily be applied to different types of coverage areas such as stadiums, and street canyons of different shapes and sizes. The numerical results for this chapter show that using four APs at the corners of a square-shaped outdoor area, pointing with 45° broadside angles towards the centre, provides the best coverage for the UE. This estimation of the parameters can save additional installation costs and reduce the processing power.

In Chapter 4, we have investigated the performance of a D-MaMIMO system with UPAs at the APs and multiple UEs equipped with single-antennas using BF and zero-forcing (ZF) pre-coding in an LoS scenario for downlink mmWave transmission. The inter-user interference (IUI) has been removed by applying not only BF but also combining the ZF pre-coding with BF. We have analysed the numerical conditioning for the ZF precoder design by obtaining the determinant of the effective channel matrix for the two user case, and have provided the conditions for the non-vanishing determinant. In fact, it depends on the path losses of two users, their correlation, and the phases of the AP-UE paths. From the first two conditions, the required user separation can be estimated. The third one occurs at random in a typical case, and we show that the probability of the required phases occurring decreases as the number of APs increases, as the correlation between the channels reduces. Moreover, for a large number of UE scenarios, the numerical results have provided vital information of total throughput of UEs to be served successfully applying this proposed approach for a given set of AP arrangements. A study on the effect of phase errors in mmWave oscillators has been carried out for the downlink case. The performance degrades progressively with an increasing phase errors. For system design, it will be advantageous to estimate performance degradation due to phase error for various AP topologies.

A multi-user (MU) D-MaMIMO system with multi-antenna arrays at both the AP and UE ends is explored in Chapter 5. To obtain the numerical results, we employed the same

LoS system model that we used in Chapter 4. In this chapter, we propose a novel approach for delivering a single data stream to a UE with multiple antenna elements rather than several data streams to each element of that UE using eigenvalue decomposition (EVD). Then we applied ZF pre-coding to eliminate the interference between multiple users. It is observed that applying only ZF pre-coding between the users as well as between the multiple streams towards the elements of the UE greatly reduces the SNR of each stream: hence the overall throughput is reduced. However, due to the multi-antenna UE diversity when transmitting only a single data stream towards a UE, the suggested technique considerably enhances performance compared to the single antenna UE. Furthermore, this system performance is compared to the single antenna UE scenario and it shows that deploying multi-antenna UEs with the proposed approach outperforms the system performance of single antenna UE. Hence, it is beneficial to have additional antenna elements at the UE end but with increasing users, the improvement becomes limited. Since the modern devices are designed to incorporate several antennas per device in mmWave frequencies, therefore, we have studied the average overall throughput for different numbers of UEs to identify the number of users to be served with maximum capacity.

In Chapter 6, an investigation has been carried out on the impact of the directional array response on the K-factor of a Ricean channel in mmWave transmission. We proposed the novel concepts of Environmental and Effective K-factor based on the directionality of the transmitting AP. We have used a single ring scattering multipath model to determine the K-factor. Assuming the presence of a line of sight hence Ricean fading, this model allows us to examine the effect of fading. It is observed that the effective K-factor depends on the radius of the ring of the scatterers and the distance between the AP and the UE. The effective K-factor increases with increasing radius of the ring of scatterers and antenna array size. However, it decreases with the increasing distance between the AP and the UE. Therefore, it highlights the significance of narrow beam-width mmWaves from large antenna arrays, as well as LoS paths. The numerical and analytical results are compared and the numerical results support the analytical results. These results should assist significantly in estimating the effect of the K-factor in mmWave communication where multipath is present.

7.2 Future Work

As a follow-up to the work in this thesis, various prospective research avenues could be pursued. The following are some of the possible future research directions:

1. The system models in this work take into account an open square coverage area and show the best AP distribution with a specific broadside angle and array configuration. However, this model is easily adaptable to practical scenarios such as stadiums of various shapes, gymnasiums, street canyons, smart city designs, and so on. It can help with important aspects of effective AP distributions for different scenarios in D-MaMIMO system without increasing unnecessary hardware costs and processing power.

2. We have implemented only the ZF scheme to eliminate the IUI for the D-MaMIMO system. However, other signal processing techniques (e.g. minimum mean squared error) should be considered for future work.

3. In Chapter 5, the multi-antenna user scenario is investigated by deploying linear antenna arrays at the UEs. However, with some additional geometrical estimation, a planar/square array could be used at the user end for the D-MaMIMO system in mmWave communication.

4. In this work, the difference in the heights of the APs and UEs is considered small and both are placed at ground level: hence the horizontal separation plays a dominant part in the system performance. However, using uniform planar arrays (UPAs) it is feasible to adapt this model for a system where the APs and UEs are located at different heights. In urban areas, there are typically a large number of high-rise buildings, and 5G base stations (i.e. gNB) are expected to serve these structures via 3D BF. Multiple beams are guided vertically and horizontally, covering multiple storeys of a high-rise building. Therefore, by adjusting the parameters, the investigation in this thesis can be expanded to design the network plan for a modern city with skyscrapers and dense users. To achieve the best system performance, various AP and UE array configurations can be explored.

5. According to the literature discussed in Chapter 2, the need for a large number of RF chains for digital pre-coding raises the cost and power consumption of deploying a large-scale antenna array. Hence, hybrid BF, which combines the advantages of both analogue and digital BF architectures, has emerged as a promising solution for lowering costs and power consumption. By introducing phase shifters and reducing the number of expensive components in digital and RF chains, hybrid BF enables the construction of relatively low-cost and low-complexity MaMIMO systems. Therefore,

hybrid BF could be an extension of this thesis work for the D-MaMIMO system in mmWave communication.

6. Extending this work to include stochastic geometry for user and AP positioning could be beneficial for channel estimation. Poisson point processes can be used to model cellular users and base stations (BSs).

7. It is critical to have a complete understanding of the channel state in order to successfully cancel user interference. However, in practice, it is not straightforward. The CSI acquisition requires substantial radio resources in FDD MaMIMO which increases with increasing dimension of the channel and in TDD-mode operation as the total number of UEs rises, it becomes challenging to guarantee the orthogonality of pilot sequences in the multi-cell situation which leads to pilot contamination. Several approaches are considered to avoid the pilot contamination. [187] has proposed optimal design pre-coding matrices to reduce the square errors induced by the pilot reuse that alleviates the pilot contamination. Recent developments in compressed sensing, sparse signal processing have drawn a lot of interest in CSI acquisition by reconstructing CSI from a limited number of channel information. This sparsity-inspired approaches reduce the high training overhead and solve the pilot contamination issue [188]. Furthermore, in comparison to conventional methods, deep learning (DL)-based approaches have recently been developed and demonstrated to significantly reduce the CSI acquisition and feedback overhead in MaMIMO systems. In [189] for hybrid antenna structure, an iterative analogue beam acquisition scheme is studied to minimise the overhead and complexity in obtaining the CSI. This work can, however, can be extended by exploring a more thorough examination of extracting CSI with the approaches discussed and the impact of estimation error on system performance.

8. It is important to consider the designing of a MU-MaMIMO system for a given coverage area with optimal energy efficiency from the environmental and economical considerations. The energy efficiency of a system is defined as the ratio between the achieved sum rate in the system and the total required power to achieve this sum rate [190]. The key factors that contribute are the number of antennas, active users in that coverage area and the transmit power. However, MaMIMO is considered as a solution to the energy efficiency issues of current cellular networks, by using appropriate active interference-suppressing pre-coding such as ZF or RZF [191]. By using proper scheduling approach where the number of transmit antennas and users increases with a limiting ratio between them the power efficiency can be improved. Also with increasing

BS antennas the transmitted power can be reduced proportionally to ensure spectral efficiency. Moreover, the quantity of quantization bits affects the energy efficiency of a MaMIMO system [192]. In [193][194] an uniform quantization scheme is proposed to find the optimal quantization bits that has low power consumption, making it an excellent choice for the practical implementation of cell-free MaMIMO. This work can be extended to evaluate the system performance in terms of energy efficiency.

9. In this work we mainly consider line-of-sight (LoS) channel model for multi-user scenarios. While multipath is likely to be sparse at mmWave propagation, a multipath channel model for the MU D-MaMIMO system can be included. In Chapter 6 we discuss a simple one ring scattering model which can be extended to a multi-cluster scattering model. Given that the scattered powers contribute significantly to the received signal, a more useful model might incorporate the probability that the LoS may be blocked. The proposed ZF pre-coding scheme's performance in NLoS situations could also be observed. Further research into the degrees of scattering loss can be conducted, taking into account the most recent propagation research findings.

References

[1] W. Jiang, B. Han, M. A. Habibi, and H. D. Schotten, "The road towards 6G: a comprehensive survey," *IEEE Open Journal of the Communications Society*, vol. 2, pp. 334–366, 2021.

[2] O. O. Erunkulu, A. M. Zungeru, C. K. Lebekwe, M. Mosalaosi, and J. M. Chuma, "5G mobile communication applications: a survey and comparison of use cases," *IEEE Access*, vol. 9, pp. 97 251–97 295, 2021.

[3] "IMT vision—framework and overall objectives of the future development of IMT for 2020 and beyond," ITU-R, Tech. Rep. ITU-R M.2083-0, Sep. 2015. [Online]. Available: https://www.itu.int/dms_pubrec/itu-r/rec/m/R-REC-M.2083-0-201509-I!!PDF-E.pdf

[4] J. Navarro-Ortiz, P. Romero-Diaz, S. Sendra, P. Ameigeiras, J. J. Ramos-Munoz, and J. M. Lopez-Soler, "A survey on 5G usage scenarios and traffic models," *IEEE Communications Surveys Tutorials*, vol. 22, no. 2, pp. 905–929, 2020.

[5] N. Khiadani, "Vision, requirements and challenges of sixth generation (6G) networks," in *2020 6th Iranian Conference on Signal Processing and Intelligent Systems (ICSPIS)*, 2020, pp. 1–4.

[6] H. Wang, P. Zhang, J. Li, and X. You, "Radio propagation and wireless coverage of LSAA-based 5G millimeter-wave mobile communication systems," *China Communications*, vol. 16, no. 5, pp. 1–18, 2019.

[7] H. Q. Ngo, A. Ashikhmin, H. Yang, E. G. Larsson, and T. L. Marzetta, "Cell-free massive MIMO versus small cells," *IEEE Transactions on Wireless Communications*, vol. 16, no. 3, pp. 1834–1850, 2017.

[8] H. Viswanathan and M. Weldon, "The past, present, and future of mobile communications," *Bell Labs Technical Journal*, vol. 19, pp. 8–21, 2014.

[9] M. A. M. Albreem, "5G wireless communication systems: vision and challenges," in *2015 International Conference on Computer, Communications, and Control Technology (I4CT)*, 2015, pp. 493–497.

[10] [Online]. Available: https://www.qualcomm.com/5g/what-is-5g

[11] J. G. Andrews, S. Buzzi, W. Choi, S. V. Hanly, A. Lozano, A. C. K. Soong, and J. C. Zhang, "What will 5G be?" *IEEE Journal on Selected Areas in Communications*, vol. 32, no. 6, pp. 1065–1082, Jun. 2014.

[12] S. Henry, A. Alsohaily, and E. S. Sousa, "5G is real: evaluating the compliance of the 3GPP 5G new radio system with the ITU IMT-2020 requirements," *IEEE Access*, vol. 8, pp. 42 828–42 840, 2020.

[13] E. Inc., "Ericsson mobility report," Mar. 2018. [Online]. Available: https://www.ericsson.com/491e34/assets/local/reports-papers/mobility-report/documents/2018/ericsson-mobility-report-november-2018.pdf

[14] J. F. Valenzuela-Valdés, n. Palomares, J. C. González-Macías, A. Valenzuela-Valdés, P. Padilla, and F. Luna-Valero, "On the ultra-dense small cell deployment for 5G networks," in *2018 IEEE 5G World Forum (5GWF)*, 2018, pp. 369–372.

[15] L. C. Gonçalves, P. Sebastião, N. Souto, and A. Correia, "One step greener: reducing 5G and beyond networks' carbon footprint by 2-tiering energy efficiency with CO2 offsetting," *Electronics*, vol. 9, no. 3, 2020. [Online]. Available: https://www.mdpi.com/2079-9292/9/3/464

[16] M. Alonzo, S. Buzzi, A. Zappone, and C. D'Elia, "Energy-efficient power control in cell-free and user-centric massive MIMO at millimeter wave," *IEEE Transactions on Green Communications and Networking*, vol. 3, no. 3, pp. 651–663, 2019.

[17] X. Liu, H. Mei, and L. Peng, "Adaptive beamforming planning for multicast mmwave communication," in *2020 International Conference on Networking and Network Applications (NaNA)*, 2020, pp. 147–151.

[18] A. N. Uwaechia and N. M. Mahyuddin, "A comprehensive survey on millimeter wave communications for fifth-generation wireless networks: feasibility and challenges," *IEEE Access*, vol. 8, pp. 62 367–62 414, 2020.

[19] "3GPP release 15." [Online]. Available: https://www.3gpp.org/release-15

[20] S. Mohanty, A. Agarwal, K. Agarwal, S. Mali, and G. Misra, "Role of millimeter wave for future 5G mobile networks: its potential, prospects and challenges," in *2021 1st Odisha International Conference on Electrical Power Engineering, Communication and Computing Technology(ODICON)*, 2021, pp. 1–4.

[21] H. Friis, "A note on a simple transmission formula," *Proceedings of the IRE*, vol. 34, no. 5, pp. 254–256, 1946.

[22] I. A. Hemadeh, K. Satyanarayana, M. El-Hajjar, and L. Hanzo, "Millimeter-wave communications: physical channel models, design considerations, antenna constructions, and link-budget," *IEEE Communications Surveys Tutorials*, vol. 20, no. 2, pp. 870–913, 2018.

[23] M. Arvas and M. Alsunaidi, "Analysis of oxygen absorption at 60 GHz frequency band," in *2019 IEEE International Symposium on Antennas and Propagation and USNC-URSI Radio Science Meeting*, 2019, pp. 2127–2128.

[24] Z. Qingling and J. Li, "Rain attenuation in millimeter wave ranges," in *2006 7th International Symposium on Antennas, Propagation EM Theory*, 2006, pp. 1–4.

[25] Y. Niu, Y. Li, D. Jin, L. Su, and A. V. Vasilakos, "A survey of millimeter wave communications (mmwave) for 5g: opportunities and challenges," *Wireless networks*, vol. 21, no. 8, pp. 2657–2676, 2015.

[26] Z. Pi and F. Khan, "An introduction to millimeter-wave mobile broadband systems," *IEEE Communications Magazine*, vol. 49, no. 6, pp. 101–107, 2011.

[27] H. Xu, T. Rappaport, R. Boyle, and J. Schaffner, "Measurements and models for 38-GHz point-to-multipoint radiowave propagation," *IEEE Journal on Selected Areas in Communications*, vol. 18, no. 3, pp. 310–321, 2000.

[28] H. Xu, V. Kukshya, and T. Rappaport, "Spatial and temporal characteristics of 60-GHz indoor channels," *IEEE Journal on Selected Areas in Communications*, vol. 20, no. 3, pp. 620–630, 2002.

[29] J. Lorca, M. Hunukumbure, and Y. Wang, "On overcoming the impact of doppler spectrum in millimeter-wave V2I communications," in *2017 IEEE Globecom Workshops (GC Wkshps)*, 2017, pp. 1–6.

[30] T. S. Rappaport, J. N. Murdock, and F. Gutierrez, "State of the art in 60-GHz integrated circuits and systems for wireless communications," *Proceedings of the IEEE*, vol. 99, no. 8, pp. 1390–1436, 2011.

[31] J. Karjalainen, M. Nekovee, H. Benn, W. Kim, J. Park, and H. Sungsoo, "Challenges and opportunities of mm-wave communication in 5G networks," in *2014 9th International Conference on Cognitive Radio Oriented Wireless Networks and Communications (CROWNCOM)*, 2014, pp. 372–376.

[32] M. Rumney, "The critical importance of accurate channel modelling for the success of mmWave 5G," in *2017 11th European Conference on Antennas and Propagation (EUCAP)*, 2017, pp. 3688–3691.

[33] M. Khatun, H. Mehrpouyan, D. Matolak, and I. Guvenc, "Millimeter wave systems for airports and short-range aviation communications: a survey of the current channel models at mmWave frequencies," in *2017 IEEE/AIAA 36th Digital Avionics Systems Conference (DASC)*, 2017, pp. 1–8.

[34] T. Bai, V. Desai, and R. W. Heath, "Millimeter wave cellular channel models for system evaluation," in *2014 International Conference on Computing, Networking and Communications (ICNC)*, 2014, pp. 178–182.

[35] M. R. Akdeniz, Y. Liu, M. K. Samimi, S. Sun, S. Rangan, T. S. Rappaport, and E. Erkip, "Millimeter wave channel modeling and cellular capacity evaluation," *IEEE Journal on Selected Areas in Communications*, vol. 32, no. 6, pp. 1164–1179, 2014.

[36] S. Hur, S. Baek, B. Kim, Y. Chang, A. F. Molisch, T. S. Rappaport, K. Haneda, and J. Park, "Proposal on millimeter-wave channel modeling for 5G cellular system," *IEEE Journal of Selected Topics in Signal Processing*, vol. 10, no. 3, pp. 454–469, 2016.

[37] C. Gustafson, K. Haneda, S. Wyne, and F. Tufvesson, "On mm-wave multipath clustering and channel modeling," *IEEE Transactions on Antennas and Propagation*, vol. 62, no. 3, pp. 1445–1455, 2014.

[38] M. K. Samimi and T. S. Rappaport, "3-D millimeter-wave statistical channel model for 5G wireless system design," *IEEE Transactions on Microwave Theory and Techniques*, vol. 64, no. 7, pp. 2207–2225, 2016.

[39] E. Björnson, E. G. Larsson, and T. L. Marzetta, "Massive MIMO: ten myths and one critical question," *IEEE Communications Magazine*, vol. 54, no. 2, pp. 114–123, 2016.

[40] L. V. d. P. Erik G. Larsson, "Massive MIMO for 5G," *IEEE 5G Tech Focus*, vol. 1, no. 1, Mar. 2017. [Online]. Available: https://futurenetworks.ieee.org/tech-focus/march-2017/massive-mimo-for-5g

[41] T. L. Marzetta, "Noncooperative cellular wireless with unlimited numbers of base station antennas," *IEEE Transactions on Wireless Communications*, vol. 9, no. 11, pp. 3590–3600, 2010.

[42] [Online]. Available: https://ma-mimo.ellintech.se/

[43] J. Hoydis, S. ten Brink, and M. Debbah, "Massive MIMO in the UL/DL of cellular networks: how many antennas do we need?" *IEEE Journal on Selected Areas in Communications*, vol. 31, no. 2, pp. 160–171, 2013.

[44] E. G. Larsson, O. Edfors, F. Tufvesson, and T. L. Marzetta, "Massive MIMO for next generation wireless systems," *IEEE Communications Magazine*, vol. 52, no. 2, pp. 186–195, 2014.

[45] J. Mundy and S. Kavanagh, "What is massive MIMO technology?" Tech. Rep., 2021. [Online]. Available: https://5g.co.uk/guides/what-is-massive-mimo-technology/

[46] D. Borges, P. Montezuma, R. Dinis, and M. Beko, "Massive MIMO techniques for 5G and beyond—opportunities and challenges," *Electronics*, vol. 10, no. 14, 2021. [Online]. Available: https://www.mdpi.com/2079-9292/10/14/1667

[47] J. Zhang, S. Chen, Y. Lin, J. Zheng, B. Ai, and L. Hanzo, "Cell-free massive MIMO: a new next-generation paradigm," *IEEE Access*, vol. 7, pp. 99 878–99 888, 2019.

[48] P. Zhu, J. Li, D. Wang, and X. You, "Large system serformance and sistributed scheme of sownlink beamforming in F-RANs with distributed antennas," *IEEE Access*, vol. 7, pp. 33 441–33 453, 2019.

[49] Q. Xue, Q. Li, C. Dong, S. Suo, and K. Niu, "Beam selection for cell-free millimeter-wave massive MIMO systems," in *2021 26th IEEE Asia-Pacific Conference on Communications (APCC)*, 2021, pp. 310–315.

[50] H. Q. Ngo, L.-N. Tran, T. Q. Duong, M. Matthaiou, and E. G. Larsson, "On the total energy efficiency of cell-free massive MIMO," *IEEE Transactions on Green Communications and Networking*, vol. 2, no. 1, pp. 25–39, 2018.

[51] L. D. Nguyen, T. Q. Duong, H. Q. Ngo, and K. Tourki, "Energy efficiency in cell-free massive MIMO with zero-forcing precoding design," *IEEE Communications Letters*, vol. 21, no. 8, pp. 1871–1874, 2017.

[52] C. He, G. Y. Li, F.-C. Zheng, and X. You, "Energy efficiency of distributed MIMO systems," in *2014 IEEE Global Conference on Signal and Information Processing (GlobalSIP)*, 2014, pp. 218–222.

[53] G. Interdonato, P. Frenger, and E. G. Larsson, "Scalability aspects of cell-free massive MIMO," *ICC 2019 - 2019 IEEE International Conference on Communications (ICC)*, May 2019. [Online]. Available: http://dx.doi.org/10.1109/ICC.2019.8761828

[54] C. D'Andrea, G. Interdonato, and S. Buzzi, "User-centric handover in mmWave cell-free massive MIMO with user mobility," *2021 29th European Signal Processing Conference (EUSIPCO)*, Aug 2021. [Online]. Available: http://dx.doi.org/10.23919/EUSIPCO54536.2021.9616361

[55] H. Q. Ngo, A. Ashikhmin, H. Yang, E. G. Larsson, and T. L. Marzetta, "Cell-free massive MIMO: nniformly great service for everyone," in *2015 IEEE 16th International Workshop on Signal Processing Advances in Wireless Communications (SPAWC)*, 2015, pp. 201–205.

[56] S. Zhou, M. Zhao, X. Xu, J. Wang, and Y. Yao, "Distributed wireless communication system: a new architecture for future public wireless access," *IEEE Communications Magazine*, vol. 41, no. 3, pp. 108–113, 2003.

[57] C.-M. Chen, A. P. Guevara, and S. Pollin, "Scaling up distributed massive MIMO: why and how," in *2017 51st Asilomar Conference on Signals, Systems, and Computers*, 2017, pp. 271–276.

[58] C.-M. Chen, V. Volskiy, A. Chiumento, L. Van der Perre, G. A. E. Vandenbosch, and S. Pollin, "Exploration of user separation capabilities by distributed large antenna arrays," in *2016 IEEE Globecom Workshops (GC Wkshps)*, 2016, pp. 1–6.

[59] A. Saleh, A. Rustako, and R. Roman, "Distributed antennas for indoor radio communications," *IEEE Transactions on Communications*, vol. 35, no. 12, pp. 1245–1251, 1987.

[60] K. T. Truong and R. W. Heath, "The viability of distributed antennas for massive MIMO systems," in *2013 Asilomar Conference on Signals, Systems and Computers*, 2013, pp. 1318–1323.

[61] M. Arnold, P. Baracca, T. Wild, F. Schaich, and S. t. Brink, "Measured distributed vs co-located massive MIMO in industry 4.0 environments," in *2021 Joint European Conference on Networks and Communications 6G Summit (EuCNC/6G Summit)*, 2021, pp. 306–310.

[62] M. Clark, T. Willis, L. Greenstein, A. Rustako, V. Erceg, and R. Roman, "Distributed versus centralized antenna arrays in broadband wireless networks," in *IEEE VTS 53rd Vehicular Technology Conference, Spring 2001. Proceedings (Cat. No.01CH37202)*, vol. 1, 2001, pp. 33–37 vol.1.

[63] D. Qiao, Y. Wu, and Y. Chen, "Massive MIMO architecture for 5G networks: co-located, or distributed?" in *2014 11th International Symposium on Wireless Communications Systems (ISWCS)*, 2014, pp. 192–197.

[64] J. Zhang and J. G. Andrews, "Distributed antenna systems with randomness," *IEEE Transactions on Wireless Communications*, vol. 7, no. 9, pp. 3636–3646, 2008.

[65] R. W. Heath Jr, T. Wu, Y. H. Kwon, and A. C. K. Soong, "Multiuser MIMO in distributed antenna systems with out-of-cell interference," *IEEE Transactions on Signal Processing*, vol. 59, no. 10, pp. 4885–4899, 2011.

[66] W. Belaoura, K. Ghanem, and H. Bousbia-Salah, "Hybrid precoding for DL massive MU-MIMO systems with distributed antenna deployments," in *2017 IEEE International Symposium on Antennas and Propagation USNC/URSI National Radio Science Meeting*, 2017, pp. 1173–1174.

[67] J. Li, D.-W. Yue, and Y. Sun, "Performance analysis of millimeter wave massive MIMO systems in centralized and distributed schemes," *IEEE Access*, vol. 6, pp. 75 482–75 494, 2018.

[68] G. Interdonato, E. Björnson, H. Quoc Ngo, P. Frenger, and E. G. Larsson, "Ubiquitous cell-free massive MIMO communications," *EURASIP Journal on Wireless Communications and Networking*, vol. 2019, no. 1, pp. 1–13, 2019.

[69] T. C. Mai, H. Quoc Ngo, and T. Q. Duong, "Cell-free massive MIMO systems with multi-antenna users," in *2018 IEEE Global Conference on Signal and Information Processing (GlobalSIP)*, 2018, pp. 828–832.

[70] C.-M. Chen, S. Blandino, A. Gaber, C. Desset, A. Bourdoux, L. Van der Perre, and S. Pollin, "Distributed massive MIMO: a diversity combining method for TDD reciprocity calibration," in *GLOBECOM 2017 - 2017 IEEE Global Communications Conference*, 2017, pp. 1–7.

[71] U. Madhow, D. R. Brown, S. Dasgupta, and R. Mudumbai, "Distributed massive MIMO: algorithms, architectures and concept systems," in *2014 Information Theory and Applications Workshop (ITA)*, 2014, pp. 1–7.

[72] M. Bashar, A. Akbari, K. Cumanan, H. Q. Ngo, A. G. Burr, P. Xiao, and M. Debbah, "Deep learning-aided finite-capacity fronthaul cell-free massive MIMO with zero forcing," in *ICC 2020 - 2020 IEEE International Conference on Communications (ICC)*, 2020, pp. 1–6.

[73] M. Bashar, K. Cumanan, A. G. Burr, M. Debbah, and H. Q. Ngo, "On the uplink max–min SINR of cell-free massive MIMO systems," *IEEE Transactions on Wireless Communications*, vol. 18, no. 4, pp. 2021–2036, 2019.

[74] S. Elhoushy, M. Ibrahim, and W. Hamouda, "Cell-free massive MIMO: a survey," *IEEE Communications Surveys Tutorials*, vol. 24, no. 1, pp. 492–523, 2022.

[75] D. Verenzuela, E. Björnson, and M. Matthaiou, "Optimal per-antenna adc bit allocation in correlated and cell-free massive MIMO," *IEEE Transactions on Communications*, vol. 69, no. 7, pp. 4767–4780, 2021.

[76] S.-N. Jin, D.-W. Yue, and H. H. Nguyen, "Spectral and energy efficiency in cell-free massive MIMO systems over correlated rician fading," *IEEE Systems Journal*, vol. 15, no. 2, pp. 2822–2833, 2021.

[77] z. Özdogan, E. Björnson, and J. Zhang, "Performance of cell-free massive MIMO with rician fading and phase shifts," *IEEE Transactions on Wireless Communications*, vol. 18, no. 11, pp. 5299–5315, 2019.

[78] Z. Wang, J. Zhang, E. Björnson, and B. Ai, "Uplink performance of cell-free massive MIMO over spatially correlated rician fading channels," *IEEE Communications Letters*, vol. 25, no. 4, pp. 1348–1352, 2021.

[79] H. Q. Ngo, H. Tataria, M. Matthaiou, S. Jin, and E. G. Larsson, "On the performance of cell-free massive MIMO in ricean fading," in *2018 52nd Asilomar Conference on Signals, Systems, and Computers*, 2018, pp. 980–984.

[80] S. Geng, J. Kivinen, X. Zhao, and P. Vainikainen, "Millimeter-wave propagation channel characterization for short-range wireless communications," *IEEE Transactions on Vehicular Technology*, vol. 58, no. 1, pp. 3–13, 2009.

[81] M. K. Samimi and T. S. Rappaport, "Ultra-wideband statistical channel model for non line of sight millimeter-wave urban channels," in *2014 IEEE Global Communications Conference*, 2014, pp. 3483–3489.

[82] G. Femenias and F. Riera-Palou, "Cell-free millimeter-wave massive MIMO systems with limited fronthaul capacity," *IEEE Access*, vol. 7, pp. 44 596–44 612, 2019.

[83] ——, "Reduced-complexity downlink cell-free mmWave massive MIMO systems with fronthaul constraints," in *2019 27th European Signal Processing Conference (EUSIPCO)*, 2019, pp. 1–5.

[84] J. García-Morales, G. Femenias, and F. Riera-Palou, "Energy-efficient access-point sleep-mode techniques for cell-free mmWave massive MIMO networks with non-uniform spatial traffic density," *IEEE Access*, vol. 8, pp. 137 587–137 605, 2020.

[85] M. Alonzo and S. Buzzi, "Cell-free and user-centric massive MIMO at millimeter wave frequencies," in *2017 IEEE 28th Annual International Symposium on Personal, Indoor, and Mobile Radio Communications (PIMRC)*, 2017, pp. 1–5.

[86] M. Alonzo, S. Buzzi, and A. Zappone, "Energy-efficient downlink power control in mmwave cell-free and user-centric massive MIMO," in *2018 IEEE 5G World Forum (5GWF)*, 2018, pp. 493–496.

[87] Y. Jin, J. Zhang, S. Jin, and B. Ai, "Channel estimation for cell-free mmWave massive MIMO through deep learning," *IEEE Transactions on Vehicular Technology*, vol. 68, no. 10, pp. 10 325–10 329, 2019.

[88] A. Burr, S. Islam, J. Zhao, and M. Bashar, "Cell-free massive MIMO with multi-antenna access points and user terminals," in *2020 54th Asilomar Conference on Signals, Systems, and Computers*, Nov. 2020, pp. 821–825.

[89] Q. Spencer, A. Swindlehurst, and M. Haardt, "Zero-forcing methods for downlink spatial multiplexing in multiuser MIMO channels," *IEEE Transactions on Signal Processing*, vol. 52, no. 2, pp. 461–471, 2004.

[90] K.-K. Wong, R. Murch, and K. Letaief, "Performance enhancement of multiuser MIMO wireless communication systems," *IEEE Transactions on Communications*, vol. 50, no. 12, pp. 1960–1970, 2002.

[91] A. S. A. Tarighat, M. Sadek, "A multi user beamforming scheme for downlink MIMO channels based on maximizing signal-to-leakage ratios," in *Proceedings. (ICASSP '05). IEEE International Conference on Acoustics, Speech, and Signal Processing, 2005.*, vol. 3, 2005, pp. iii/1129–iii/1132 Vol. 3.

[92] L. Du, L. Li, H. Q. Ngo, T. C. Mai, and M. Matthaiou, "Cell-free massive MIMO: joint maximum-ratio and zero-forcing precoder with power control," *IEEE Transactions on Communications*, vol. 69, no. 6, pp. 3741–3756, 2021.

[93] [Online]. Available: https://www.antenna-theory.com/

[94] C. A. Balanis, *Antenna theory: analysis and design*. John wiley & sons, 2015.

[95] [Online]. Available: https://scholar.valpo.edu/cgi/viewcontent.cgi?filename=32&article=1000&context=engineering_oer&type=additional

[96] J. A. Nanzer, S. R. Mghabghab, S. M. Ellison, and A. Schlegel, "Distributed phased arrays: challenges and recent advances," *IEEE Transactions on Microwave Theory and Techniques*, vol. 69, no. 11, pp. 4893–4907, 2021.

[97] Z. Wu, B. Wu, Z. Su, and X. Zhang, "Development challenges for 5G base station antennas," in *2018 International Workshop on Antenna Technology (iWAT)*, 2018, pp. 1–3.

[98] J. Koppenborg, H. Halbauer, S. Saur, and C. Hoek, "3D beamforming trials with an active antenna array," in *2012 International ITG Workshop on Smart Antennas (WSA)*, 2012, pp. 110–114.

[99] G. J. Foschini, "Layered space-time architecture for wireless communication in a fading environment when using multi-element antennas," *Bell Labs Technical Journal*, vol. 1, no. 2, pp. 41–59, 1996.

[100] A. Sayeed, "Deconstructing multiantenna fading channels," *IEEE Transactions on Signal Processing*, vol. 50, no. 10, pp. 2563–2579, 2002.

[101] M. Sanchez-Fernandez, S. Zazo, and R. Valenzuela, "Performance comparison between beamforming and spatial multiplexing for the downlink in wireless cellular systems," *IEEE Transactions on Wireless Communications*, vol. 6, no. 7, pp. 2427–2431, 2007.

[102] [Online]. Available: https://spectrum.ieee.org/5g-bytes-beamforming-explained

[103] B. D. Van Veen and K. M. Buckley, "Beamforming: a versatile approach to spatial filtering," *IEEE assp magazine*, vol. 5, no. 2, pp. 4–24, 1988.

[104] [Online]. Available: http://www.massive-mimo.net/

[105] E. Björnson, M. Bengtsson, and B. Ottersten, "Optimal multiuser transmit beamforming: a difficult problem with a simple solution structure [lecture notes]," *IEEE Signal Processing Magazine*, vol. 31, no. 4, pp. 142–148, 2014.

[106] C. Zhang and D. Yin, "A new multi-user transmit beamforming scheme for downlink MIMO channels," in *2016 IEEE/ACES International Conference on Wireless Information Technology and Systems (ICWITS) and Applied Computational Electromagnetics (ACES)*, 2016, pp. 1–2.

[107] C. Masterson, "Massive MIMO and beamforming: the signal processing behind the 5G buzzwords," *Analog Dialogue*, vol. 51, Jun. 2017.

[108] S. M. Razavizadeh, M. Ahn, and I. Lee, "Three-dimensional beamforming: a new enabling technology for 5G wireless networks," *IEEE Signal Processing Magazine*, vol. 31, no. 6, pp. 94–101, 2014.

[109] N. Seifi, J. Zhang, R. W. Heath, T. Svensson, and M. Coldrey, "Coordinated 3D beamforming for interference management in cellular networks," *IEEE Transactions on Wireless Communications*, vol. 13, no. 10, pp. 5396–5410, 2014.

[110] J. Niu, G. Y. Li, Y. Li, D. Fang, and X. Li, "Joint 3D beamforming and resource allocation for small cell wireless backhaul in HetNets," *IEEE Communications Letters*, vol. 21, no. 10, pp. 2286–2289, 2017.

[111] S. A. Busari, K. M. S. Huq, S. Mumtaz, L. Dai, and J. Rodriguez, "Millimeter-wave massive MIMO communication for future wireless systems: a survey," *IEEE Communications Surveys Tutorials*, vol. 20, no. 2, pp. 836–869, 2018.

[112] S. Kutty and D. Sen, "Beamforming for millimeter wave communications: an inclusive survey," *IEEE Communications Surveys Tutorials*, vol. 18, no. 2, pp. 949–973, 2016.

[113] C. Tao and B. Zhou, "Indoor localization with smart antenna system: multipath mitigation with MIMO beamforming scheme," in *2017 IEEE 14th International Conference on Mobile Ad Hoc and Sensor Systems (MASS)*, 2017, pp. 303–307.

[114] A. Paulraj and T. Kailath, "On beamforming in presence of multipath," in *ICASSP '85. IEEE International Conference on Acoustics, Speech, and Signal Processing*, vol. 10, 1985, pp. 564–567.

[115] L. Yu, W. Liu, and R. Langley, "Robust adaptive beamforming for multi-path environment based on domain weighted PCA," in *2007 15th International Conference on Digital Signal Processing*, 2007, pp. 91–94.

[116] Z. Xiao, X.-G. Xia, D. Jin, and N. Ge, "Iterative eigenvalue decomposition and multipath-grouping Tx/Rx joint beamformings for millimeter-wave communications," *IEEE Transactions on Wireless Communications*, vol. 14, no. 3, pp. 1595–1607, 2015.

[117] S. Rangan, T. S. Rappaport, and E. Erkip, "Millimeter-wave cellular wireless networks: potentials and challenges," *Proceedings of the IEEE*, vol. 102, no. 3, pp. 366–385, 2014.

[118] T. S. Rappaport, F. Gutierrez, E. Ben-Dor, J. N. Murdock, Y. Qiao, and J. I. Tamir, "Broadband millimeter-wave propagation measurements and models using adaptive-beam antennas for outdoor urban cellular communications," *IEEE Transactions on Antennas and Propagation*, vol. 61, no. 4, pp. 1850–1859, 2013.

[119] S.-L. Ju, N.-I. Kim, S.-Q. Lee, J. Kim, and K.-S. Kim, "Hybrid beamforming scheme for millimeter-wave massive MIMO and dense small cell networks," in *2019 25th Asia-Pacific Conference on Communications (APCC)*, 2019, pp. 301–304.

[120] Y. Sun and C. Qi, "Weighted sum-rate maximization for analog beamforming and combining in millimeter wave massive MIMO communications," *IEEE Communications Letters*, vol. 21, no. 8, pp. 1883–1886, 2017.

[121] [Online]. Available: https://telecompedia.net/5g-overview/

[122] M. A. B. Abbasi, V. F. Fusco, and O. Yurduseven, "High directivity beamformer for millimeter-wave 5G base stations," in *2020 IEEE 3rd 5G World Forum (5GWF)*, 2020, pp. 309–311.

[123] Y.-H. Cho and J.-J. Kim, "Line-of-sight MIMO channel in millimeter-wave beamforming system: modeling and prototype results," in *2015 IEEE 81st Vehicular Technology Conference (VTC Spring)*, 2015, pp. 1–5.

[124] D.-W. Yue and Q. Yan, "LOS component-based beamforming for downlink wireless backhauling with massive MIMO," in *2016 Sixth International Conference on Instrumentation Measurement, Computer, Communication and Control (IMCCC)*, 2016, pp. 869–873.

[125] T. Kebede, Y. Wondie, and J. Steinbrunn, "Performance evaluation of millimeterwave-massive MIMO with beamforming techniques," in *2021 International Symposium on Networks, Computers and Communications (ISNCC)*, 2021, pp. 1–8.

[126] Y. Zou, Q. Li, G. Yang, and X. Cheng, "Analog beamforming for millimeter-wave MIMO systems via stochastic optimization," in *2016 8th International Conference on Wireless Communications Signal Processing (WCSP)*, 2016, pp. 1–5.

[127] S. Hur, T. Kim, D. J. Love, J. V. Krogmeier, T. A. Thomas, and A. Ghosh, "Millimeter wave beamforming for wireless backhaul and access in small cell networks," *IEEE Transactions on Communications*, vol. 61, no. 10, pp. 4391–4403, 2013.

[128] X. Gao, L. Dai, C. Yuen, and Z. Wang, "Turbo-like beamforming based on tabu search algorithm for millimeter-wave massive MIMO systems," *IEEE Transactions on Vehicular Technology*, vol. 65, no. 7, pp. 5731–5737, 2016.

[129] G. Barb, M. Otesteanu, F. Alexa, and A. Ghiulai, "Digital beamforming techniques for future communications systems," in *2020 12th International Symposium on Communication Systems, Networks and Digital Signal Processing (CSNDSP)*, 2020, pp. 1–4.

[130] S. Yoshioka, S. Suyama, T. Okuyama, J. Mashino, and Y. Okumura, "5G massive MIMO with digital beamforming and two-stage channel estimation for low SHF band," in *2017 Wireless Days*, 2017, pp. 107–112.

[131] A. A. Farid, M. Abdelghany, U. Madhow, and M. J. W. Rodwell, "Dynamic range requirements of digital vs. RF and tiled beamforming in mm-Wave massive MIMO," in *2021 IEEE Radio and Wireless Symposium (RWS)*, 2021, pp. 46–48.

[132] W. Hong, J. Zhou, J. Chen, Z. Jiang, C. Yu, and C. Guo, "Asymmetric full-digital beamforming mmWave massive MIMO systems for B5G/6G wireless communications," in *2020 IEEE Asia-Pacific Microwave Conference (APMC)*, 2020, pp. 31–32.

[133] I. Ahmed, H. Khammari, A. Shahid, A. Musa, K. S. Kim, E. De Poorter, and I. Moerman, "A survey on hybrid beamforming techniques in 5G: architecture and system model perspectives," *IEEE Communications Surveys Tutorials*, vol. 20, no. 4, pp. 3060–3097, 2018.

[134] C. Kim, T. Kim, and J.-Y. Seol, "Multi-beam transmission diversity with hybrid beamforming for MIMO-OFDM systems," in *2013 IEEE Globecom Workshops (GC Wkshps)*, 2013, pp. 61–65.

[135] S. Han, C.-l. I, Z. Xu, and C. Rowell, "Large-scale antenna systems with hybrid analog and digital beamforming for millimeter wave 5G," *IEEE Communications Magazine*, vol. 53, no. 1, pp. 186–194, 2015.

[136] F. Sohrabi and W. Yu, "Hybrid digital and analog beamforming design for large-scale antenna arrays," *IEEE Journal of Selected Topics in Signal Processing*, vol. 10, no. 3, pp. 501–513, 2016.

[137] A. Li, D. Spano, J. Krivochiza, S. Domouchtsidis, C. G. Tsinos, C. Masouros, S. Chatzinotas, Y. Li, B. Vucetic, and B. Ottersten, "A tutorial on interference exploitation via symbol-level precoding: overview, state-of-the-art and future directions," *IEEE Communications Surveys Tutorials*, vol. 22, no. 2, pp. 796–839, 2020.

[138] F. Rusek, D. Persson, B. K. Lau, E. G. Larsson, T. L. Marzetta, O. Edfors, and F. Tufvesson, "Scaling up MIMO: opportunities and challenges with very large arrays," *IEEE Signal Processing Magazine*, vol. 30, no. 1, pp. 40–60, 2013.

[139] H. Prabhu, J. Rodrigues, O. Edfors, and F. Rusek, "Approximative matrix inverse computations for very-large MIMO and applications to linear pre-coding systems," in *2013 IEEE Wireless Communications and Networking Conference (WCNC)*, 2013, pp. 2710–2715.

[140] C. Zhang, Y. Jing, Y. Huang, and L. Yang, "Performance analysis for massive MIMO downlink with low complexity approximate zero-forcing precoding," *IEEE Transactions on Communications*, vol. 66, no. 9, pp. 3848–3864, 2018.

[141] S. Chatzinotas, B. Ottersten, and R. De Gaudenzi, *Cooperative and cognitive satellite systems*, 1st ed. USA: Academic Press, Inc., 2015.

[142] A. Wiesel, Y. C. Eldar, and S. Shamai, "Zero-forcing precoding and generalized inverses," *IEEE Transactions on Signal Processing*, vol. 56, no. 9, pp. 4409–4418, 2008.

[143] M. Bashar, M. Eslami, and M. J. Dehghani, "Zero-forcing precoding with partially outdated CSI over time-varying MIMO broadcast channels," in *2013 IEEE 77th Vehicular Technology Conference (VTC Spring)*, 2013, pp. 1–5.

[144] T. Yoo and A. Goldsmith, "On the optimality of multiantenna broadcast scheduling using zero-forcing beamforming," *IEEE Journal on Selected Areas in Communications*, vol. 24, no. 3, pp. 528–541, 2006.

[145] ——, "Optimality of zero-forcing beamforming with multiuser diversity," in *IEEE International Conference on Communications, 2005. ICC 2005. 2005*, vol. 1, 2005, pp. 542–546 Vol. 1.

[146] D. Bartolome and A. Perez-Neira, "Spatial scheduling in multiuser wireless systems: from power allocation to admission control," *IEEE Transactions on Wireless Communications*, vol. 5, no. 8, pp. 2082–2091, 2006.

[147] S. C. Tripathi, A. Trivedi, and S. Rajoria, "Power optimization of cell free massive MIMO with zero-forcing beamforming technique," in *2018 Conference on Information and Communication Technology (CICT)*, 2018, pp. 1–4.

[148] W. Dai, Y. Liu, and B. Rider, "How many users should be turned on in a multi-antenna broadcast channel?" *CoRR*, vol. abs/0705.2274, 2007. [Online]. Available: http://arxiv.org/abs/0705.2274

[149] H. R. K. M. Zhang, J., "Mode switching for the multi-antenna broadcast channel based on delay and channel quantization," *EURASIP J. Adv. Signal Process*, 2009.

[150] W. Jiang and H. D. Schotten, "Impact of channel aging on zero-forcing precoding in cell-free massive MIMO systems," *CoRR*, vol. abs/2107.01404, 2021. [Online]. Available: https://arxiv.org/abs/2107.01404

[151] W. Abu Shehab and Z. Al-qudah, "Singular value decomposition: principles and applications in multiple input multiple output communication system," *International Journal of Computer Networks and Communications*, vol. 9, pp. 13–21, 01 2017.

[152] E. Telatar, "Capacity of multi-antenna gaussian channels," *European Transactions on Telecommunications*, vol. 10, no. 6, pp. 585–595, 1999. [Online]. Available: https://onlinelibrary.wiley.com/doi/abs/10.1002/ett.4460100604

[153] W. Liu, L. L. Yang, and L. Hanzo, "SVD-assisted multiuser transmitter and multiuser detector design for MIMO systems," *IEEE Transactions on Vehicular Technology*, vol. 58, no. 2, pp. 1016–1021, 2009.

[154] W. Liu, C. Li, J. Li, and L. Hanzo, "Singular value decomposition-based multiuser multiple-input multiple-output vector perturbationaided downlink transmitter and lattice-reductionassisted uplink receiver pair," *IET Commun.*, vol. 6, no. 15, pp. 2448–2454, 2012. [Online]. Available: https://doi.org/10.1049/iet-com.2011.0184

[155] L. Lee, J. Wang, and X. Wu, "ZF beamforming performance analysis for multiuser spatial multiplexing with imperfect channel feedback," in *2007 International Conference on Wireless Communications, Networking and Mobile Computing*, 2007, pp. 869–872.

[156] G. Lebrun, T. Ying, and M. Faulkner, "MIMO transmission over a time-varying channel using SVD," in *Global Telecommunications Conference, 2002. GLOBECOM '02. IEEE*, vol. 1, 2002, pp. 414–418 vol.1.

[157] V.-F. Crâşmariu, M.-O. Arvinte, A.-A. Enescu, and S. Ciochină, "Performance analysis of the singular value decomposition with block-diagonalization precoding in multi-user massive MIMO systems," in *2016 12th IEEE International Symposium on Electronics and Telecommunications (ISETC)*, 2016, pp. 71–74.

[158] S. Salous, V. Degli Esposti, F. Fuschini, R. S. Thomae, R. Mueller, D. Dupleich, K. Haneda, J.-M. Molina Garcia-Pardo, J. Pascual Garcia, D. P. Gaillot, S. Hur, and M. Nekovee, "Millimeter-wave propagation: characterization and modeling toward fifth-generation systems. (wireless corner)," *IEEE Antennas and Propagation Magazine*, vol. 58, no. 6, pp. 115–127, 2016.

[159] M. M. Taygur and T. F. Eibert, "Investigation of distributed and collocated base stations in a large urban massive MIMO scenario," in *2017 11th European Conference on Antennas and Propagation (EUCAP)*, 2017, pp. 1577–1581.

[160] Z. Liu and L. Dai, "A comparative study of downlink MIMO cellular networks with co-located and distributed base-station antennas," *IEEE Transactions on Wireless Communications*, vol. 13, no. 11, pp. 6259–6274, 2014.

[161] ——, "Asymptotic capacity analysis of downlink MIMO systems with co-located and distributed antennas," in *2013 IEEE 24th Annual International Symposium on Personal, Indoor, and Mobile Radio Communications (PIMRC)*, 2013, pp. 1286–1290.

[162] G. N. Kamga, M. Xia, and S. Aïssa, "Spectral-efficiency analysis of massive MIMO systems in centralized and distributed schemes," *IEEE Transactions on Communications*, vol. 64, no. 5, pp. 1930–1941, 2016.

[163] G. R. MacCartney and T. S. Rappaport, "Millimeter-wave base station diversity for 5g coordinated multipoint CoMP applications," *IEEE Transactions on Wireless Communications*, vol. 18, no. 7, pp. 3395–3410, 2019.

[164] *5G; Study on channel model for frequencies from 0.5 to 100 GHz*, 3GPP TR 38.901 V.14.1. ed., Aug. 2017.

[165] [Online]. Available: https://www.ofcom.org.uk/__data/assets/pdf_file/0014/104702/5G-spectrum-access-at-26-GHz.pdf

[166] W.-C. Kao, S.-Q. Zhan, and T.-S. Lee, "AI-aided 3-D beamforming for millimeter wave communications," in *2018 International Symposium on Intelligent Signal Processing and Communication Systems (ISPACS)*, 2018, pp. 278–283.

[167] Y. Lu, M. Koivisto, J. Talvitie, M. Valkama, and E. S. Lohan, "Positioning-aided 3D beamforming for enhanced communications in mmwave mobile networks," *IEEE Access*, vol. 8, pp. 55 513–55 525, 2020.

[168] S. Tripathi, S. Redhu, and R. M. Hegde, "Clustering-assisted 3D beamforming for throughput maximization in mmwave networks," in *2021 IEEE International Conference on Communications Workshops (ICC Workshops)*, 2021, pp. 1–6.

[169] M. E. Hassan, A. E. Falou, and C. Langlais, "Performance assessment of linear precoding for multi-user massive MIMO systems on a realistic 5g mmwave channel," in *2018 IEEE Middle East and North Africa Communications Conference (MENACOMM)*, 2018, pp. 1–5.

[170] H. Yang and T. L. Marzetta, "Performance of conjugate and zero-forcing beamforming in large-scale antenna systems," *IEEE Journal on Selected Areas in Communications*, vol. 31, no. 2, pp. 172–179, 2013.

[171] E. Nayebi, A. Ashikhmin, T. L. Marzetta, H. Yang, and B. D. Rao, "Precoding and power optimization in cell-free massive MIMO systems," *IEEE Transactions on Wireless Communications*, vol. 16, no. 7, pp. 4445–4459, 2017.

[172] H. V. Balan, R. Rogalin, A. Michaloliakos, K. Psounis, and G. Caire, "Achieving high data rates in a distributed MIMO system," in *Proceedings of the 18th Annual International Conference on Mobile Computing and Networking*, ser. Mobicom '12. New York, NY, USA: Association for Computing Machinery, 2012, p. 41–52. [Online]. Available: https://doi.org/10.1145/2348543.2348552

[173] [Online]. Available: https://www.3gpp.org/DynaReport/38-series.htm

[174] X. Li, E. Björnson, S. Zhou, and J. Wang, "Massive MIMO with multi-antenna users: when are additional user antennas beneficial?" in *2016 23rd International Conference on Telecommunications (ICT)*, 2016, pp. 1–6.

[175] P. Layec, P. Piantanida, R. Visoz, and A. O. Berthet, "Capacity bounds for MIMO multiple access channel with imperfect channel state information," in *2008 IEEE Information Theory Workshop*, 2008, pp. 21–25.

[176] T. Yoo and A. Goldsmith, "Capacity and power allocation for fading MIMO channels with channel estimation error," *IEEE Transactions on Information Theory*, vol. 52, no. 5, pp. 2203–2214, 2006.

[177] T. C. Mai, H. Q. Ngo, and T. Q. Duong, "Downlink spectral efficiency of cell-free massive MIMO systems with multi-antenna users," *IEEE Transactions on Communications*, vol. 68, no. 8, pp. 4803–4815, 2020.

[178] K. Dawui and D. Slock, "Multiuser-MIMO downlink TX-RX design based on SVD channel diagonalization and multiuser diversity," 01 2005, pp. 1493–1497.

[179] X. An, C.-S. Sum, R. V. Prasad, J. Wang, Z. Lan, J. Wang, R. Hekmat, H. Harada, and I. Niemegeers, "Beam switching support to resolve link-blockage problem in 60 GHz WPANs," in *2009 IEEE 20th International Symposium on Personal, Indoor and Mobile Radio Communications*, 2009, pp. 390–394.

[180] "Study of mmWave signal propagation in non-line-of-sight environment," Telecom Infra Project, Inc., Tech. Rep., 2019. [Online]. Available: https://cdn.brandfolder.io/D8DI15S7/as/qcra3r-2jik60-cze57x/mmWave-Networks_Study-of-mmWave-Signal-Propagation-in-Non-line-of-site-Environment_-_White_Paper_-_Telecom_Infra_Project.pdf

[181] J. G. Andrews, T. Bai, M. N. Kulkarni, A. Alkhateeb, A. K. Gupta, and R. W. Heath, "Modeling and analyzing millimeter wave cellular systems," *IEEE Transactions on Communications*, vol. 65, no. 1, pp. 403–430, 2017.

[182] S. Mukherjee, S. S. Das, A. Chatterjee, and S. Chatterjee, "Analytical calculation of rician K-factor for indoor wireless channel models," *IEEE Access*, vol. 5, pp. 19 194–19 212, 2017.

[183] A. Doukas and G. Kalivas, "Rician K factor estimation for wireless communication systems," in *2006 International Conference on Wireless and Mobile Communications (ICWMC'06)*, 2006, pp. 69–69.

[184] D. Dupleich, N. Iqbal, C. Schneider, S. Haefner, R. Müller, S. Skoblikov, J. Luo, and R. Thomä, "Investigations on fading scaling with bandwidth and directivity at 60 GHz," in *2017 11th European Conference on Antennas and Propagation (EUCAP)*, 2017, pp. 3375–3379.

[185] A. Borhani and M. Pätzold, "A non-stationary one-ring scattering model," in *2013 IEEE Wireless Communications and Networking Conference (WCNC)*, 2013, pp. 2620–2625.

[186] "*NIST Digital Library of Mathematical Functions*," http://dlmf.nist.gov/, Release 1.1.5 of 2022-03-15, f. W. J. Olver, A. B. Olde Daalhuis, D. W. Lozier, B. I. Schneider, R. F. Boisvert, C. W. Clark, B. R. Miller, B. V. Saunders, H. S. Cohl, and M. A. McClain, eds. [Online]. Available: http://dlmf.nist.gov/

[187] J. Jose, A. Ashikhmin, T. L. Marzetta, and S. Vishwanath, "Pilot contamination and precoding in multi-cell TDD systems," *IEEE Transactions on Wireless Communications*, vol. 10, no. 8, pp. 2640–2651, 2011.

[188] J.-C. Shen, J. Zhang, K.-C. Chen, and K. B. Letaief, "High-dimensional CSI acquisition in massive MIMO: sparsity-inspired approaches," *IEEE Systems Journal*, vol. 11, no. 1, pp. 32–40, 2017.

[189] S. Chen, Q. Gao, R. Chen, H. Li, S. Sun, and Z. Liu, "A CSI acquisition approach for mmWave massive MIMO," *China Communications*, vol. 16, no. 9, pp. 1–14, 2019.

[190] H. M. Al-Obiedollah, K. Cumanan, J. Thiyagalingam, J. Tang, A. G. Burr, Z. Ding, and O. A. Dobre, "Spectral-energy efficiency trade-off-based beamforming design for MISO non-orthogonal multiple access systems," *IEEE Transactions on Wireless Communications*, vol. 19, no. 10, pp. 6593–6606, 2020.

[191] E. Björnson, L. Sanguinetti, J. Hoydis, and M. Debbah, "Optimal design of energy-efficient multi-user mimo systems: is massive mimo the answer?" *IEEE Transactions on Wireless Communications*, vol. 14, no. 6, pp. 3059–3075, 2015.

[192] H. Q. Ngo, E. G. Larsson, and T. L. Marzetta, "Energy and spectral efficiency of very large multiuser MIMO systems," *IEEE Transactions on Communications*, vol. 61, no. 4, pp. 1436–1449, 2013.

[193] M. Bashar, K. Cumanan, A. G. Burr, H. Q. Ngo, E. G. Larsson, and P. Xiao, "Energy efficiency of the cell-free massive MIMO uplink with optimal uniform quantization," *IEEE Transactions on Green Communications and Networking*, vol. 3, no. 4, pp. 971–987, 2019.

[194] M. Bashar, H. Q. Ngo, K. Cumanan, A. G. Burr, P. Xiao, E. Björnson, and E. G. Larsson, "Uplink spectral and energy efficiency of cell-free massive MIMO with optimal uniform quantization," *IEEE Transactions on Communications*, vol. 69, no. 1, pp. 223–245, 2021.